UNIVERSITÀ DI PARMA

UNIVERSITA' DEGLI STUDI DI PARMA

DOTTORATO DI RICERCA IN
INGEGNERIA CIVILE E ARCHITETTURA

CICLO XXXIII

ADVANCED METHODOLOGY FOR FRETTING FATIGUE ASSESSMENT OF METALLIC STRUCTURAL COMPONENTS

Coordinatore:
Prof. Sandro Longo

Supervisor:
Prof.ssa Sabrina Vantadori

Co-supervisor:
Prof. Andrea Carpinteri

Candidato:
Andrea Zanichelli

Anni Accademici 2017/2018 - 2019/2020

ABSTRACT

The present Ph.D. Thesis deals with the analysis of metallic structural components subject to fretting fatigue in partial slip regime. An analytical methodology for fretting fatigue assessment of structural components is proposed. Such a methodology allows to evaluate both the initial crack path and the lifetime of metallic structures under fretting fatigue elastic partial slip loading conditions in high-cycle fatigue.

The proposed methodology consists in the joint application of the multiaxial fatigue criterion by Carpinteri et al. together with the non-local approach (named Critical Direction Method) by Araújo et al. The philosophy related to the theory of the Critical Distance by Taylor is also taken into account in the procedure.

The stress field induced into two bodies in contact subject to fretting fatigue is analysed in Chapter 2, since it represents an input data for the methodology. Firstly, the damage process associated with fretting is described, by even exploiting the concept of fretting map. Subsequently, the main methodologies available in the literature to analyse fretting fatigue problems are briefly reviewed. Finally, the analytical formulation implemented in the proposed methodology is detailed.

Chapter 3 is devoted to the description of the advanced analytical methodology proposed in the present Ph.D. Thesis for fretting fatigue assessment of structural components. In particular, both the Critical Direction Method by Araújo et al., the theory of the Critical Distance by Taylor, and the Carpinteri et al. criterion for fretting fatigue are described. Then, the steps of the advanced methodology proposed in the present Ph.D. Thesis are detailed.

Chapter 4 deals with the validation of the proposed analytical methodology. In more detail, ten different experimental campaigns available in the literature and

related to fretting fatigue tests in partial slip conditions are examined. Eight different materials, that is, four aluminium alloys, one titanium alloy and three steels, are analysed. The results obtained in terms of both crack path orientation and fatigue life are described and compared to the experimental ones available in the literature, for each experimental campaign examined.

Finally, conclusions are summarised in Chapter 5.

INDEX

1
OBJECT AND OBJECTIVES OF THE PH.D. THESIS

1.1 Object of study

The present Ph.D. Thesis deals with the analysis of metallic structural components subject to fretting fatigue in partial slip regime.

Fretting is a contact phenomenon that occurs when a structural component is clamped against another mechanical part in presence of small oscillatory relative displacements. In such a condition, relative micro-displacements arise at the contact surface. Two different regimes can be distinguished on the basis of the magnitude of such relative displacements:

i) *Gross slip regime*, with micro-displacements generally of the order of $20 \div 300\ \mu m$. In such a condition, characterised by global relative motion between the components, the main damage phenomenon is the material wear (Berthier, 1989);

ii) *Partial slip regime*, when the relative micro-displacements are of the order of few microns, together with a magnitude of the load clamping the components sufficiently high to prevent complete sliding between them. In such a condition, the contact surface consists of an inner stick region, with no relative displacements, and an outer micro-slip region, and the main damage phenomenon is the nucleation of cracks at the contact surface due to high stress gradient (Hurricks,1970).

Superficial debris formation due to material wear is a complex long-term issue. However, such a damage phenomenon is less dangerous than the crack nucleation and subsequent propagation when components are subjected to remote fatigue loading (Waterhouse, 1992). Therefore, partial slip regime has been recognised as the most damaging condition.

As a matter of fact, a remote fatigue loading, acting at least on one of the components under contact, is able to promote the evolution of surface cracks, that

can lead to failure of the fatigued component itself. This situation is referred to as *fretting fatigue*, which is well-known to be different from plain fatigue, mainly due to the high stress level that characterises the region near the contact surface (Szolwinski, 1997). Moreover, fretting fatigue is a complex phenomenon that depends on more than 50 parameters (Collins, 1965), which can be narrowed down into eight groups: relative slip amplitude, number of loading cycles, frequency of cyclic loading, magnitude and distribution of the contact pressure, local stress state, material and surface conditions, temperature, and environments surrounding the component surfaces (Sunde, 2018).

Fretting fatigue has been recognised as the primary failure mode in many in-service engineering components in different fields of application. Railway transport, where cracks nucleating due to rolling fatigue issues may lead to failure and consequent derailment, both air and sea transport, where damages related to detachment of layers or components in riveted joints could happen, and automotive area, where failure can occur in wheel spindle, turbine blades hook systems with the hub, fasten of crankshaft with bearing, are worth noting. Moreover, fretting fatigue affects orthopaedic implants, metal ropes and cables, and many other applications in which bolted joints are subjected to small oscillatory relative displacements or vibrations.

Most failures due to fretting fatigue occur in high-cycle fatigue regime conditions, where a large portion up to 90% of total fatigue life is spent in crack nucleation, whereas only a small amount is related to crack propagation (Namjoshi, 2002). Therefore, a crack-nucleation approach is desirable to be applied in order to assess the fatigue behaviour of fretting-affected components.

In such a context, an accurate analysis of fatigue behaviour of structural components subject to fretting fatigue appears to be of fundamental importance.

1.2 Objectives of the Ph.D. Thesis

An analytical methodology for fretting fatigue assessment of structural components is proposed in the present Ph.D. Thesis. In more detail, such a methodology may be employed in order to evaluate both the initial crack path and the lifetime of metallic structures under fretting fatigue elastic partial slip loading conditions in

high-cycle fatigue. Consequently, being based on linear-elastic formulations, it could be easily applied to practical situations in the industrial field.

The proposed methodology falls in the category of stress-based critical-plane approach. In particular, the criterion by Carpinteri et al. (Carpinteri, 2011) for metallic structures under multiaxial constant amplitude fatigue loading in high-cycle fatigue regime, originally proposed for plain fatigue conditions, is here extended to the case of fretting fatigue. The Carpinteri et al. criterion is implemented in conjunction with the Critical Direction Method proposed by Araújo et al. (Araújo, 2017), and the philosophy related to the theory of the Critical Distance by Taylor (Taylor, 2007) is also taken into account in the procedure.

The stress field induced into two bodies in contact subject to fretting fatigue is analysed in **Chapter 2**, since it represents an input data for the methodology. Firstly, the damage process associated with fretting is described, by even exploiting the concept of fretting map. Subsequently, the main methodologies available in the literature to analyse fretting fatigue problems are briefly reviewed. Finally, the analytical formulation implemented in the proposed methodology is detailed.

Chapter 3 is devoted to the description of the advanced analytical methodology proposed in the present Ph.D. Thesis for fretting fatigue assessment of structural components. In particular, both the Critical Direction Method by Araújo et al., the theory of the Critical Distance by Taylor, and the Carpinteri et al. criterion for fretting fatigue are described. Then, the steps of the advanced methodology proposed in the present Ph.D. Thesis are detailed.

Chapter 4 deals with the validation of the proposed analytical methodology. In more detail, ten different experimental campaigns available in the literature and related to fretting fatigue tests in partial slip conditions are examined. Eight different materials, that is, four aluminium alloys, one titanium alloy and three steels, are analysed. The results obtained in terms of both crack path orientation and fatigue life are described and compared to the experimental ones available in the literature, for each experimental campaign examined.

Finally, conclusions are summarised in **Chapter 5**.

1.3 References

Araújo J.A., Almeida G.M.J., Ferreira J.L.A., da Silva C.R.M., Castro F.C. Early cracking orientation under high stress gradients: The fretting case. *International Journal of Fatigue*, 2017; 100: 611-618.

Berthier Y., Vincent L., Godet M. Fretting fatigue and fretting wear. *Tribology International*, 1989; 22: 235-242.

Carpinteri A., Spagnoli A., Vantadori S. Multiaxial fatigue assessment using a simplified critical plane-based criterion. *International Journal of Fatigue*, 2011; 33: 969-976.

Collins J.A. Fretting-fatigue damage-factor determination. *Journal of Engineering for Industry*, 1965; 87, 3: 298-302.

Hurricks P.L. Mechanism of fretting. *Wear*, 1970; 15: 389-409.

Namjoshi S.A., Mall S., Jain V.K., Jin O. Fretting fatigue crack initiation mechanism in Ti-6Al-4V. *Fatigue and Fracture of Engineering Materials and Structures*, 2002; 25, 10: 955-964.

Sunde S.L., Berto F., Haugen B. Predicting fretting fatigue in engineering design. *International Journal of Fatigue*, 2018; 117: 314-326.

Szolwinski M.P., Farris T.N. Mechanics of fretting fatigue crack formation. *International Journal of Fatigue*, 1997; 19: 39-49.

Taylor D. *The Theory of Critical Distances: A New Perspective in Fracture Mechanics*. UK: Elsevier; 2007.

Waterhouse R.B. The problems of fretting fatigue testing. *In: Attia M.H., Waterhouse R.B., editors. Standardization of fretting fatigue test methods and equipment*. ASTM STP 1159, Philadelphia, 1992, 13-19.

2
STRESS FIELD DUE TO FRETTING FATIGUE

2.1 Introduction

The present Chapter deals with the analysis of the stress field induced into two bodies in contact, subject to fretting fatigue.

Firstly, the damage process associated with fretting is described. Moreover, the loading conditions that characterise such a phenomenon, that are fretting wear and fretting fatigue, are analysed and the mechanical behaviour under such conditions is described by exploiting the concept of fretting map.

Subsequently, the main methodologies available in the literature to analyse fretting fatigue problems are briefly reviewed. Such methodologies are based on both analytical and numerical solutions.

The methodology proposed in the present Ph.D. Thesis belongs to the field of the stress-based critical plane approach. In particular, the multiaxial fatigue criterion proposed by Carpinteri et al. (Carpinteri, 2011) is used in conjunction with the Critical Direction method proposed by Araújo et al. (Araújo, 2017) and the theory of the Critical Distance by Taylor (Taylor, 2007).

Finally, the analytical formulation implemented in such a methodology is detailed in the case of cylindrical contact, because the advanced methodology proposed in the present Ph.D. Thesis is verified by taking into account experimental fretting fatigue tests in partial slip conditions. Although the application of the above methodology to simple cases, such as cylinder-to-flat fretting fatigue tests, may appear restrictive because of its simplicity, it is fundamental for understanding the phenomenon of fretting fatigue. Moreover, in order to study more complex geometries, numerical approaches based on finite element models would be more suitable. However, the calibration of such models is quite difficult, and analytical solutions (such as the one implemented in the

methodology proposed in the present Ph.D. Thesis) are often employed for calibration, in order to achieve more reliable results.

2.2 Fretting phenomenon: basic concepts

Many in-service engineering components are subjected to a large number of vibrations. When such components are clamped against a different mechanical part by means of a normal load, relative cyclic nano-/micro-displacements arise at contact surface. This contact phenomenon is named fretting (Nowell, 2005; Waterhouse, 1992).

The damage process associated with fretting is caused by the synergistic contribution of wear, corrosion, and crack nucleation and growth (Waterhouse, 1972). According to Hurricks (Hurricks, 1970), a typical damage mechanism can be observed in engineering materials subject to fretting.

The scarring of the superficial oxide layer is the initial mechanism that can be observed (Sunde, 2018). Then, the formation of cold-welds at the surface asperities appears, thus modifying the friction between the contact surfaces. In particular, the value of the friction coefficient has experimentally been observed to increase during the first few hundreds of loading cycles (Hills, 1998).

When the above micro-welds break and wear off, micro-debris appear between the contact surfaces (Szolwinski, 1997). Although such debris may initially promote the abrasion phenomenon, they act as a protective layer (named third body) reducing the wear of the material (Berthier, 1989).

As the number of loading cycles increases, plastic deformations take place near the contact surface, thus resulting in possible nucleation of several grain-sized microcracks (Endo, 1976). When such microcracks affect the superficial oxide layer, additional microdebris arise. This mechanism, together with corrosive environmental conditions, accelerates the wear process.

In such a condition, if a cyclic loading is applied to one of the members of the contact, the propagation of one or more of the aforementioned microcracks into the bulk material is promoted. It should be highlighted that the near-surface crack nucleation stage is dominated by the high stress gradient due to contact and

strongly depends on the material microstructure, whereas remote fatigue loading mainly affects the crack propagation stage (Nowell, 1990).

As far as the loading conditions are concerned, fretting wear and fretting fatigue can be distinguished (Waterhouse, 1992). Fretting wear loading condition is attained when at least one of the members of the contact is subjected to an external cyclic motion, whereas fretting fatigue loading condition is attained when at least one of the members of the contact is subjected to an external cyclic load.

In both such conditions either partial slip or gross slip regime may occur. According to the theoretical model by Mindlin (Mindlin, 1949), partial slip regime is attained when the tangential force remains lower than the product of the normal load and the static coefficient of friction, and there are parts of contact where no slip occurs. The fretting loop in a tangential force-displacement plane is elliptical (Hannel, 2001). On the other hand, gross slip regime is attained when the tangential force is equal to the above product, and slip occurs across the whole contact. The fretting loop is trapezoidal (Hannel, 2001).

In order to properly describe the mechanical behaviour under both fretting wear and fretting fatigue, the concept of fretting map can be exploited. Such a tool is a visual description of the fretting phenomenon, built in order to characterise the fretting problem and distinguish the regimes involved. In particular, by means of fretting maps, it is possible to distinguish the regime of fretting contact in terms of:

i) Relative displacements, thus identifying stick (that is, no sliding), mixed stick and slip, or gross slip;
ii) Surface degradation, thus identifying fatigue, wear, or oxidation attack;
iii) Fretting loop shape, thus identifying linear, elliptical or trapezoidal shape.

A review of the main fretting maps available in the literature is given by Zhou et al. (Zhou, 2006). The concept of fretting map under fretting wear loading condition was initially proposed by Vingsbo and Soderberg (Vingsbo, 1988). They identified the slip amplitude as the most significant parameter. Therefore, they built different fretting maps, where the normal force, the frequency of vibration, the fretting wear rate, or the fretting lifetime were generally identified as a function of the slip amplitude.

Vingsbo and Soderberg experimentally identified three regimes (***Figure 2.1***):

i) Stick regime, characterised by no sliding at the interface and very limited wear and oxidation in correspondence of individual asperities. The fretting loop collapses in a segment;
ii) Mixed stick-slip regime, characterized by a central stick area and a surrounding annular slip area. Extensive crack formation (fatigue) arises in the slip area with release of particles from cracks (wear), and wear and oxidation appear at the shear fractured individual asperities in the stick area. The fretting loop has an elliptical shape;
iii) Gross slip regime, characterized by slip that takes place across the whole contact area, extensive wear with sliding marks in fretting direction and material delamination and detach of particles, and oxidation with detach of oxide flakes. Wear and oxidation are strongly coupled in such a regime. The fretting loop has a trapezoidal shape.

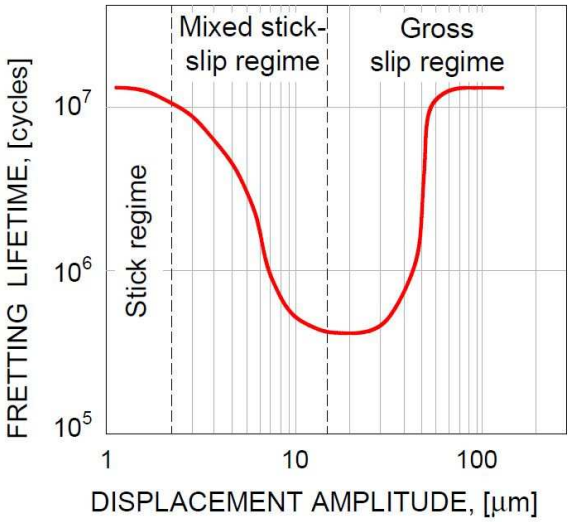

Figure 2.1 *Example of fretting map under fretting wear loading condition proposed by Vingsbo and Soderberg (Vingsbo, 1988).*

Subsequently, Zhou et al. (Zhou, 1990; Zhou, 1992; Zhou, 1995) proposed the *running condition fretting map* (RCFM), where the fretting regimes are distinguished in partial slip regime, mixed fretting regime and gross slip regime,

depending on both displacement amplitude and number of loading cycles. More precisely, the regimes experimentally identified are (***Figure 2.2a***):

i) Partial slip regime, attained for small displacement amplitude values where, during the entire test, the contact behaves as in partial slip regime described by Mindlin or, in an equivalent way, in the mixed stick-slip regime described by Vingsbo and Soderberg. The fretting loop has an elliptical shape during the whole test;

ii) Mixed fretting regime, attained for intermediate displacement amplitude values, associated with an unstable fretting loop, that may have a trapezoidal shape or an elliptical shape depending on the number of loading cycles. The Mindlin model is not valid in such a regime;

iii) Gross slip regime, attained for large displacement amplitude values where, during the whole test, the contact behaves as in the gross slip regime described by both Mindlin and Vingsbo and Soderberg. The fretting loop has a trapezoidal shape during the whole test.

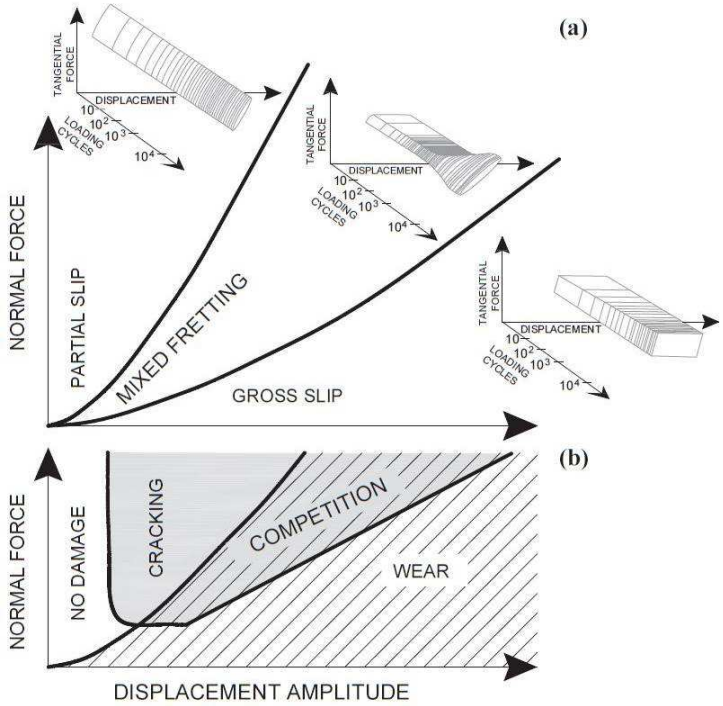

Figure 2.2 *(a) Running condition fretting map and (b) material response fretting map.*

Note that Zhou et al. ignored the stick regime highlighted by Vingsbo and Soderberg suggesting, in agreement with Mindlin, that there are always some regions of the contact experiencing slip and, therefore, no stick regime can actually exist.

Moreover, the regime definitions by Zhou et al. are more realistic than those previously presented, because both Mindlin and Vingsbo and Soderberg neglected the early stage of fretting process (that is, what happens below 10^4 loading cycles) and therefore were not able to capture the mixed fretting regime.

Another fretting map, named *material response fretting map* (MRFM), was proposed by Heredia and Fouvry (Heredia, 2010). In such a fretting map, no damage domain, cracking domain, competition domain, and wear domain are distinguished (***Figure 2.2b***).

Concerning the correspondence between RCFM and MRFM shown in ***Figure 2.2***, partial slip regime is divided into a security domain, without damage, and a domain where cracking appears. On the other hand, gross slip regime is associated with wear and oxidation, whereas mixed fretting regime generates competition between cracking and wear.

Both fretting wear and fretting fatigue conditions have been widely investigated in last decades. In particular, fretting fatigue has been recognised as a primary failure mode across a wide range of structural components. Therefore, the main analytical and numerical solutions available in the literature for the case of fretting fatigue are reviewed in the following Section.

2.3 Analytical and numerical methods for fretting fatigue

Fretting fatigue has been recognised as a primary failure mode across a wide range of structural components, such as dovetail joints, bolt and riveted joints, spline coupling, running cables, and overhead conductors (Araújo, 2016; Juoksukangas, 2016; Moraes, 2018; Ruiz, 1984). Such a phenomenon is well-known to differ from plain fatigue, especially because of the high stress-gradient near the surface of the component due to contact.

The analytical studies of contact date back to the end of XIX century, when Hertz (Hertz, 1882) studied frictionless contact between linear elastic spherical

half-spaces. The Hertzian solution was then extended by many researchers, in order to find closed form solutions for different cases. Johnson et al. (Johnson, 1971) included the adhesive forces between the contact bodies, whereas Cattaneo (Cattaneo, 1938) and Mindlin (Mindlin, 1949) independently considered partial slips due to the presence of tangential loads. The Cattaneo-Mindlin case was then integrated by Nowell and Hills (Nowell, 1987) by taking into account the effect of a bulk cyclic stress on the stress components. Moreover, the Cattaneo-Mindlin problem was extended by Jager (Jager, 1998) to more general geometries and, subsequently, by Davies et al. (Davies, 2012) to varying normal loads.

Asymptotic analysis has also been employed to study the stress concentration in fretting fatigue, due to the analogy with cracks in fracture mechanics. Such a theory has been applied especially in complete contact problems with sharp contact edges, where the Hertzian theory fails. Williams (Williams, 1952) and Bogy (Bogy, 1968) proposed to evaluate the stress components as functions of the wedge angle, in elastically similar bodies and elastically dissimilar bodies, respectively. The asymptotic theory has been applied also to incomplete contact in partial slip by Dini and Hills (Dini, 2004), who compared the results obtained with those deduced by using the Cattaneo-Mindlin solution, and by Fleury et al. (Fleury, 2017) who extended the analysis to more complex loading histories.

Analytical models are widely used for comparisons with experimental results and parametric studies. Moreover, such methods can be used to evaluate the stress field in real components, once the parameters involved have been adjusted.

On the other hand, numerical methods such as finite element methods, are becoming increasingly used, allowing to examine more complex geometries, loading histories, and external conditions. In general, when half-plane theory is violated, numerical methods are needed.

Finite element methods are available in the literature in order to take into account the effect of either wear or plasticity in the fretting fatigue modelling (Gandiolle, 2013; Madge, 2007). Moreover, microstructural effects, such as the damage evolution and the crack initiation, may be studied by including continuum damage mechanics in the finite element code (Zhang, 2012).

The extended finite element methods have recently attracted the interest of many researchers due to the possibility to enrich the solution of standard finite

element methods. In more detail, discontinuous functions can be implemented, thus providing the possibility to capture local and discontinuous effects. Moës et al. (Moës, 1999) proposed a model able to simulate the crack growth without the need for remeshing, and Giner et al. (Giner, 2008) were able to find good estimations in terms of stress intensity factors with a relatively coarse mesh by using singular expressions for complete contact as enrichment functions in the formulation of finite elements.

Nowadays, different approaches implementing either analytical or numerical models have been applied to assess the fatigue life of fretting affected components. Some of those approaches consider both crack nucleation and crack propagation phase. Araújo and Nowell (Araújo, 2009) proposed a total life methodology for the evaluation of mixed low-high cycle fatigue tests. According to such a methodology, the number of cycles needed to nucleate a crack of a given length is added to the number of cycles for propagation. It is worth noting that the choice of the initiation crack length is arbitrary and may lead to very different results. Navarro et al. (Navarro, 2003) proposed to define the initiation crack length by computing, in different material points along the crack path, the driving force for both initiation and propagation by using the Basquin equation and the Linear Elastic Fracture Mechanics (LEFM), respectively. The minimum depth at which the LEFM driving force was bigger than the one related to the initiation mechanism was assumed to be the initiation crack length. Consequently, the total life was obtained as the sum between the initiation number of cycles and the number of cycles for crack propagation until failure.

Some approaches related only to the crack propagation phase are available in the literature. Such approaches, based on the linear elastic fracture mechanics, aim to determine whether a crack will arrest after initiation by means of threshold curves for the stress intensity factors. By using a numerical methodology based on a stress-intensity factor criterion, Said et al. (Said, 2020) showed that cracks propagated up to a certain extent even in fully compressive state, and proposed a Mode II threshold. Moreover, Giannakopoulos et al. (Giannakopoulos, 1998) compared the contact stress with the stress singularities due to cracks. The crack growth in fretting fatigue was compared to a branching crack starting from a principal crack represented by the contact interface. The fretting fatigue life was

evaluated by means of the classical Paris law, by exploiting the asymptotic field description and inferring the order of singularity to be square-root bounded.

Nevertheless, damage models concerning the crack nucleation phase are mainly employed in fretting fatigue assessment, since crack nucleation life has been observed to be around 90% of the total fretting fatigue life (Walvekar, 2014). Such models may be classified according to Bhatti and Wahab (Bhatti, 2018) on the basis of the approach used to define failure. More precisely, four different approaches may be distinguished: fretting specific parameters (FSP) approach, continuum damage mechanics (CDM) approach, stress invariant (SI) approach, and critical plane (CP) approach.

In order to take into account the high frictional forces at the contact interface, fretting specific parameters incorporating the effect of slip amplitude have been proposed. The most widespread parameter was that proposed by Ruiz et al. (Ruiz, 1984), which combined relative slip amplitude with shear stress to obtain the frictional energy due to contact forces and later added tensile stress to such a frictional energy for better predicting the actual crack location. Such parameters provide a quantitative prediction of fretting fatigue behaviour, and are widely used in many industrial applications.

Continuum damage mechanics approach aims to describe the nucleation process inside a representative volume element at mesoscale, by employing mechanical variables. More precisely, a damage scalar variable incorporating the effect of mean stress, stress amplitude, loading history, material, and loading conditions is adopted. Different CDM models are available in the literature, such as those proposed by Bhattacharya and Ellingwood (Bhattacharya, 1998), Chaboche and Lesne (Chaboche, 1988) and Lemaitre (Lemaitre, 1985), in which the crack nucleation is assumed to occur when a critical value of damage is achieved. Since damage is computed as a scalar variable, no information can be obtained about crack orientation.

As far as the stress invariant approach is concerned, the parameter suggested by Crossland (Crossland, 1956) is worth noting. Such a parameter takes into account both the maximum amplitude of second invariant of the deviatoric stress tensor and the maximum hydrostatic pressure. This approach is characterised by a low time requesting computation, but it is not able to determine the crack orientation.

According to the critical plane approach, fatigue assessment is performed on a specific plane named critical plane, which is prone to be the crack nucleation plane. This approach can further be classified as stress-based, strain-based, or strain-energy density based approach. Findley (Findley, 1959) and later McDiarmid (McDiarmid, 1991) proposed two different stress-based parameters for high-cycle fatigue regime, both of them depending on the maximum normal stress. Brown and Miller (Brown, 1973) suggested a strain-based evaluation of fatigue life, by proposing a linear combination of shear strain amplitude and maximum normal strain range. Fatemi and Socie (Fatemi, 1988) modified the Brown and Miller parameter by substituting the normal strain with the normal stress, in order to include the effect of non-proportional loading and mean stress. Moreover, among the strain energy density-based parameters, the one by Smith et al. (Smith, 1970), known as the Smith Watson and Topper (SWT) parameter (defined as maximum tensile stress multiplied by strain amplitude), and the one by Liu (Liu, 1993) (based on virtual strain energy) are the most widespread.

It is important to highlight that estimations can be improved by applying non-local approaches, that is, by taking into account either the stress state related to a material point at a certain distance from the contact zone or a mean stress state computed along a line or in a volume. Note that the strategy based on a mean state of stress was originally proposed for notched structural components: an analogy between notches and fretting fatigue seems to be appropriate since the notch effect in terms of stress concentration is similar to that due to the severe stress gradients in the contact zone for fretting fatigue (Araújo, 2016).

In the context of critical plane approach, Araújo et al. (Araújo, 2020) employed a finite element method that incorporated wear and a critical plane-based criterion coupled with a critical distance varying with fatigue life, in order to numerically analyse fretting fatigue tests on wires taken from overhead conductors. The approach showed reasonably accurate estimation of fretting fatigue life in medium-high cycle regime.

The methodology proposed in the present Ph.D. Thesis belongs to the field of stress-based critical plane approach. In particular, the multiaxial fatigue criterion proposed by Carpinteri et al. (Carpinteri, 2011) is implemented in conjunction with the Critical Direction method proposed by Araújo et al. (Araújo, 2017) and the

theory of the Critical Distance by Taylor (Taylor, 2007). The stress field used as input for the criterion is analytically evaluated by using the closed-form solution by Johnson (Johnson, 1985), based on the formalisms by Hertz (Hertz, 1896), Cattaneo (Cattaneo, 1938) and Mindlin (Mindlin, 1949), and McEwen (McEwen, 1949), together with the closed-form solution by Nowell and Hills (Nowell, 1987).

In more detail, such an analytical formulation in the case of cylindrical contact is discussed in the following Section, since the advanced methodology proposed in the present PhD Thesis is verified by taking into account experimental fretting fatigue tests in partial slip conditions.

2.4 Analytical solution for fretting fatigue in partial slip regime: cylindrical contact

Let us consider a typical fretting fatigue configuration (***Figure 2.3***), where two fretting pads, which may be characterised by either spherical or cylindrical shape, are pushed against a dog-bone specimen in partial slip regime. The reference frame, $Oxyz$, is shown in ***Figure 2.3***. A normal constant force, P, and a cyclic tangential force, $Q(t)$, are applied to the pads, whereas the specimen experiences a cyclic axial stress, $\sigma_B(t)$, named bulk stress in the following, which is in-phase with $Q(t)$.

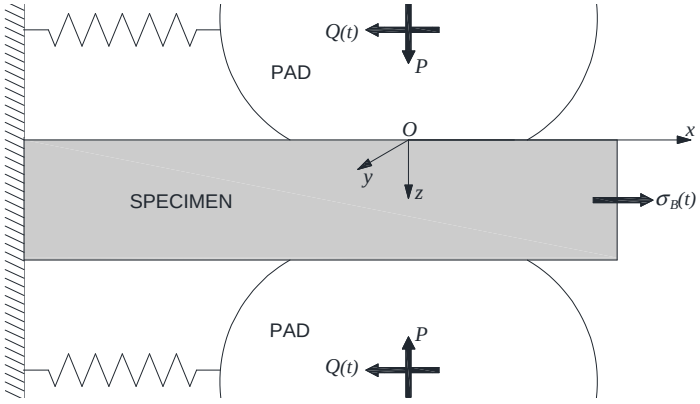

Figure 2.3 *Typical cylinder-to-flat fretting fatigue test, in presence of both constant normal load, P, cyclic tangential load, $Q(t)$, and cyclic bulk stress, $\sigma_B(t)$.*

The stress field in the vicinity of the contact zone, in the case of fretting fatigue elastic partial slip loading condition, is detailed hereafter. Note that only the stress field in the case of cylindrical pads is presented in the following: nevertheless, the stress field in the case of spherical pads may be deduced in a similar way (Johnson, 1985).

2.4.1 Constant normal load in contact problems

Let us consider a contact problem with two non-conforming bodies, thus characterized by different profiles. The contact zone between such solids consists of a single point (or a line, depending on the bodies geometry), which coincides with the origin of the reference frame *Oxyz* in ***Figure 2.4***. However, as far as an external load or displacement is applied, the two bodies deform and the contact area becomes a finite area, whose sizes are a function of the magnitudes of applied loads or displacements.

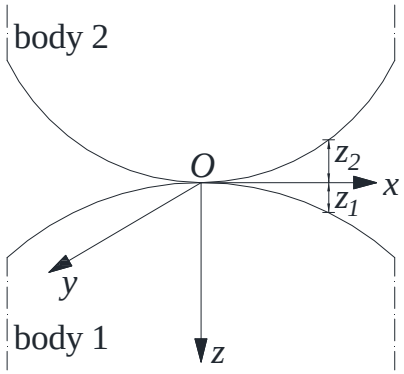

Figure 2.4 *Contact between non-conforming bodies, characterized by different general profiles.*

Therefore, a theory of contact is required to predict the shape and size of the contact surface, the magnitude and distribution of the surface tractions, and displacements and deformations induced within the two bodies.

In the region close to the contact zone, the surface profile of each body may be approximated by means of a parabolic shape, represented by the following quadratic expressions:

$$z_1 = A_1 x^2 + B_1 y^2 + C_1 xy \qquad (2.1a)$$

$$z_2 = A_2 x^2 + B_2 y^2 + C_2 xy \qquad (2.1b)$$

where higher order terms are neglected. A_1, B_1, A_2, B_2 are positive constants depending on the shape of solids brought into contact. It is possible to identify a proper orientation of the x and y axes (that is, x_1 and y_1) so that the term in xy vanishes and *Equations (2.1)* become:

$$z_1 = \frac{1}{2R_1'} x_1^2 + \frac{1}{2R_1''} y_1^2 \qquad (2.2a)$$

$$z_2 = -\left(\frac{1}{2R_2'} x_2^2 + \frac{1}{2R_2''} y_2^2 \right) \qquad (2.2b)$$

where R_1', R_1'' and R_2', R_2'' represent the surface radii of curvature for body 1 and 2, respectively, in correspondence of the origin, O, of the reference frame.

Moreover, the distance, h, between the two surfaces may be written as follows:

$$h = z_1 + z_2 = \frac{1}{2R'} x^2 + \frac{1}{2R''} y^2 = Ax^2 + By^2 \qquad (2.3)$$

where R' and R'' represent the main relative radii of curvature, whereas A and B are positive constants. If the longitudinal axes of the two bodies are inclined to each other by an angle α, it is possible to demonstrate that A and B are defined by the following expressions:

$$A+B=\frac{1}{2}\left(\frac{1}{R'}+\frac{1}{R''}\right)=\frac{1}{2}\left(\frac{1}{R_1'}+\frac{1}{R_1''}+\frac{1}{R_2'}+\frac{1}{R_2''}\right) \qquad (2.4a)$$

$$|B-A|=\frac{1}{2}\left[\left(\frac{1}{R_1'}-\frac{1}{R_1''}\right)^2+\left(\frac{1}{R_2'}-\frac{1}{R_2''}\right)^2+2\left(\frac{1}{R_1'}-\frac{1}{R_1''}\right)\left(\frac{1}{R_2'}-\frac{1}{R_2''}\right)\cos 2\alpha\right] \qquad (2.4b)$$

By means of *Equations 2.4*, it can be deduced that:

i) If the two bodies are solids of revolutions, then $A+B=\frac{1}{2}\left(\frac{1}{R_1}+\frac{1}{R_2}\right)$. The points characterised by the same value of h lay on a circle centred at the origin O;

ii) If the two bodies are cylindrical and in contact along their longitudinal axes, then $A=\frac{1}{2}\left(\frac{1}{R_1}+\frac{1}{R_2}\right)$ and $B=0$. The points characterised by the same value of h lay on a straight line parallel to the longitudinal axis;

iii) If the two bodies have general profiles, then A and B are defined by general expressions. The points characterised by the same value of h lay on an ellipse centred at the origin O.

We shall now consider the deformation (dotted line in ***Figure 2.5***) caused by the application of a normal load, P, on both bodies of general shape (chosen convex for convenience).

Due to such a normal load, two points T_1 and T_2 reasonably distant from the contact surface move towards the origin of the reference system, O, whereas the points $S_1(x,y,z_1)$ and $S_2(x,y,z_2)$ on the contact surface move along the z axis by an amount equal to $\bar{u}_{z1}$ and $\bar{u}_{z2}$, measured from T_1 and T_2, respectively. In such a situation, the following two cases may arise:

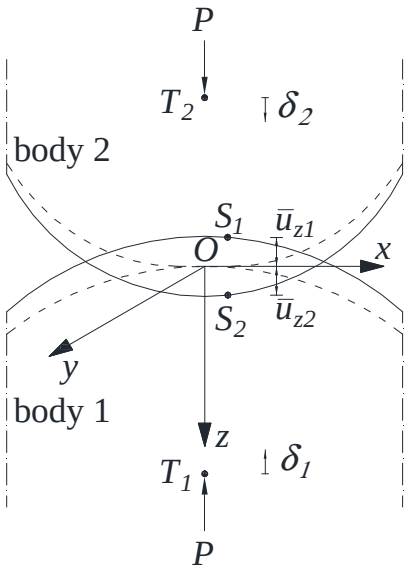

Figure 2.5 *Contact between non-conforming bodies, characterized by different general profiles: deformation due to constant normal load, P (dashed lines).*

i) S_1 and S_2 are coincident, that means that the two points are located within the contact region. In such a case, the following equality holds:

$$\bar{u}_{z1} + \bar{u}_{z2} + h = \delta_1 + \delta_2 \qquad (2.5)$$

And, by means of *Equation (2.3)*, it becomes:

$$\bar{u}_{z1} + \bar{u}_{z2} = \delta_1 + \delta_2 - Ax^2 - By^2 \qquad (2.6)$$

ii) S_1 and S_2 are not coincident, that means that the two points lie outside the contact region. In such a case, the following equality holds:

$$\bar{u}_{z1} + \bar{u}_{z2} > \delta_1 + \delta_2 - Ax^2 - By^2 \qquad (2.7)$$

In order to analyse the deformation due to contact pressure, it is necessary to determine the distribution of the pressure field at the contact interface, such that the resulting displacements, normal to the surfaces, satisfy both *Equation (2.6)* within the contact area and *Equation (2.7)* outside such an area.

Heinrich Hertz (Hertz, 1896) was the first one to achieve significant results concerning the problem of the contact between two elastic bodies of general shape, clamped against each other by means of a constant normal load. He considered some hypotheses in order to simplify the problem. In more detail, by considering the half-width a of the contact region, the radius R of curvature of the two bodies, the depth l of such bodies, the deformation ε_y in correspondence of the yielding of the material, the friction coefficient μ, Hertz assumed that:

1) $a << R$, that is, the width of the contact surface is negligible with respect to the radius of curvature for each body. Such a hypothesis allows us to approximate the contact surfaces to an elastic half-space;
2) $a << l$, that is, each body can be considered as an elastic half-space loaded over an elliptical region at the surface. Such a hypothesis allows us to obtain a stress/deformation field that is not influenced by the presence of the solid boundary;
3) $\varepsilon < \varepsilon_y$, that is, the magnitude of the deformations near the contact region allows us to apply the theory of elasticity;
4) $\mu = 0$, that is, the surfaces of the bodies are frictionless, that is, only normal stress is transferred.

Therefore, as far as two cylindrical bodies in contact along their longitudinal axes are considered, the contact surface consists in a strip of width $2a$, lying parallel to the axes of the cylinders (***Figure 2.6***). Such a contact surface may be considered as the limit of the elliptical surface that characterizes the contact between general bodies, as one of the axes tends to infinite. It is important to highlight that a plane strain condition may be assumed and, consequently, only x and z coordinates are considered (***Figure 2.6***).

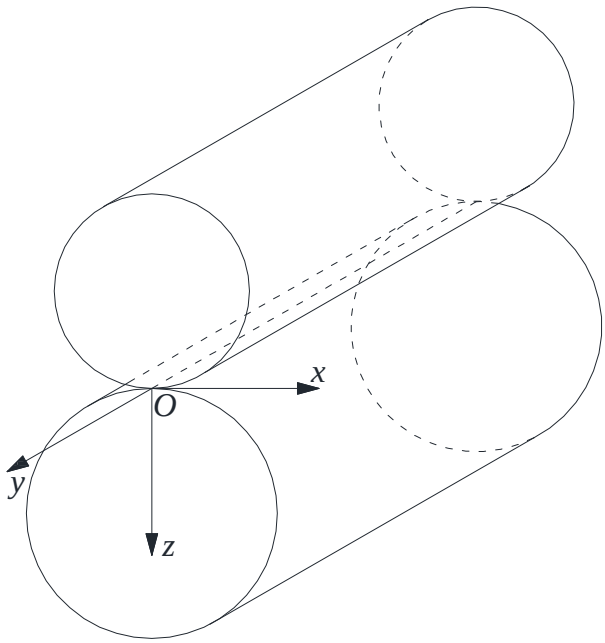

Figure 2.6 *Contact between cylindrical bodies.*

Equation (2.3) allows us to express the separation h between two cylindrical bodies as follows:

$$h = \frac{1}{2}\left(\frac{1}{R_1} + \frac{1}{R_2}\right)x^2 = \frac{1}{2R}x^2 \qquad (2.8)$$

being $\frac{1}{R} = \left(\frac{1}{R_1} + \frac{1}{R_2}\right)$. Hence, for points lying on the contact surfaces, the condition represented by *Equation (2.6)* must be respected:

$$\bar{u}_{z1} + \bar{u}_{z2} = \delta_1 + \delta_2 - \frac{1}{2R}x^2 \qquad (2.9)$$

whereas, for points outside the contact surface, the condition represented by *Equation (2.7)* holds:

$$\bar{u}_{z1} + \bar{u}_{z2} > \delta_1 + \delta_2 - \frac{1}{2R}x^2 \qquad (2.10)$$

By means of the Hertzian theory, it is possible to uniquely determine the normal pressure distribution, $p(x)$, that satisfies *Equations (2.9)* and *(2.10)*. More precisely, by differentiating both contributions of *Equation (2.9)*, it is possible to obtain:

$$\frac{\partial \bar{u}_{z1}}{\partial x} + \frac{\partial \bar{u}_{z2}}{\partial x} = -\frac{1}{R}x \qquad (2.11)$$

Moreover, by exploiting the results reported by Johnson (Johnson, 1985) related to the displacement field of a half-space due to the presence of a normal load, it is possible to write:

$$\frac{\partial \bar{u}_{z1}}{\partial x} + \frac{\partial \bar{u}_{z2}}{\partial x} = -\frac{2}{\pi E^*}\int_{-a}^{a} \frac{p(s)}{x-s}\,ds \qquad (2.12)$$

where E^* represents the elastic modulus for plane strain condition. In the case of two bodies in contact, it becomes $\frac{1}{E^*} = \frac{1-\nu_1^2}{E_1} + \frac{1-\nu_2^2}{E_2}$.

Therefore, by considering *Equations (2.11)* and *(2.12)*, we can derive:

$$\int_{-a}^{a} \frac{p(s)}{x-s}\,ds = \frac{\pi E^*}{2R}x \qquad (2.13)$$

from which the normal pressure distribution, $p(x)$, can be obtained:

$$p(x) = -\frac{\pi E^*}{2R}\frac{x^2 - \frac{a^2}{2}}{\pi\sqrt{\left(a^2 - x^2\right)}} + \frac{P}{\pi\sqrt{a^2 - x^2}} \qquad (2.14)$$

In order to determine a distribution $p(x)$ of compression on the whole contact region and a finite stress gradient at the edges of such an area, it is possible to demonstrate (Hertz, 1896; Johnson, 1985) that the constant normal load P must be equal to the following expression:

$$P = \frac{\pi a^2 E^*}{4R} \qquad (2.15)$$

Therefore, by combining *Equations (2.14)* and *(2.15)*, it is possible to determine the contact semi-width, a , between two cylindrical half spaces:

$$a = \sqrt{\frac{4PR}{\pi E^*}} \qquad (2.16)$$

Moreover, the normal pressure distribution arising at the contact interface between the two cylindrical bodies is obtained from *Equation (2.14)*:

$$p(x) = \frac{2P}{\pi a^2}\sqrt{a^2 - x^2} \qquad (2.17)$$

Such a distribution, named *Hertzian contact pressure distribution*, is characterized by a parabolic shape (***Figure 2.7***) with a maximum value in the middle of the contact region ($x = 0$) equal to:

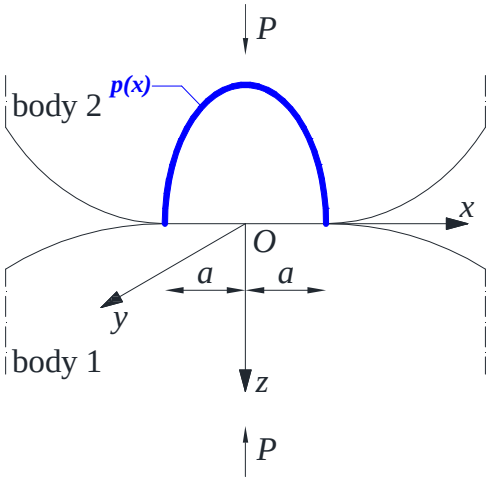

Figure 2.7 *Contact pressure distribution, $p(x)$, at the interface of cylindrical bodies, subject to constant normal load, P.*

$$p_0 = \frac{2P}{\pi a} = \sqrt{\frac{P E^*}{\pi R}} \tag{2.18}$$

The determination of stresses due to cylindrical contact was firstly provided in a simplified form by McEwen (McEwen, 1949). In more detail, the components of the stress tensor, produced by a general constant load P in the vicinity of the contact zone, are given by:

$$\sigma_x^P = -\frac{p_0}{a}\left[m\left(1+\frac{z^2+n^2}{m^2+n^2}\right) - 2z \right] \tag{2.19a}$$

$$\sigma_z^P = -\frac{p_0}{a} m\left(1-\frac{z^2+n^2}{m^2+n^2}\right) \tag{2.19b}$$

$$\tau_{xz}^{P}=\begin{cases}-\dfrac{p_0}{a}n\left(\dfrac{m^2-z^2}{m^2+n^2}\right) & \text{for } x\geq 0\\ \dfrac{p_0}{a}n\left(\dfrac{m^2-z^2}{m^2+n^2}\right) & \text{for } x<0\end{cases} \qquad (2.19c)$$

where the functions m and n are given by:

$$m^2=\frac{1}{2}\left[\sqrt{\left(a^2-x^2+z^2\right)^2+4x^2z^2}+\left(a^2-x^2+z^2\right)\right] \qquad (2.20a)$$

$$n^2=\frac{1}{2}\left[\sqrt{\left(a^2-x^2+z^2\right)^2+4x^2z^2}-\left(a^2-x^2+z^2\right)\right] \qquad (2.20b)$$

Nevertheless, the influence of a cyclic tangential load on both stress and displacement fields is not taken into account by the Hertzian theory, and will be analysed in the following Section.

2.4.2 Static tangential load in contact problems

The influence of a static tangential force, Q, on both stress and displacement fields within two bodies in contact is analysed in the present Section.

Let us consider two bodies of general profile, subject to both a normal load, P, and a tangential load, Q, as is shown in ***Figure 2.8***.

Firstly, the effect of the tangential force on size and shape of the contact surfaces, as well as on the distribution of normal pressure on such an area, needs to be analysed. In order to ensure the equilibrium, the distribution $q_1(x,y)$ of tangential load on surface 1 needs to be equal, but with opposite direction, to the distribution $q_2(x,y)$ of tangential load on surface 2:

$$q_1(x,y)=-q_2(x,y) \qquad (2.21)$$

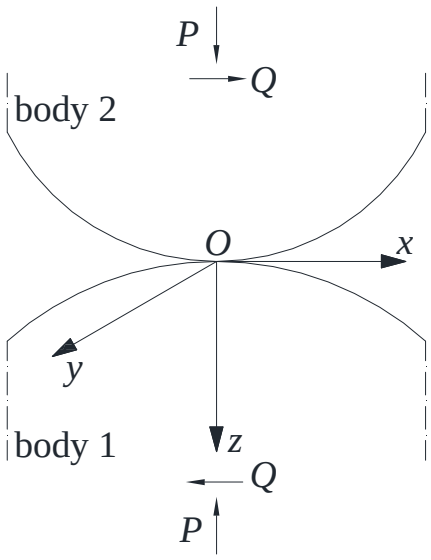

Figure 2.8 *Contact between non-conforming bodies, characterized by different general profiles, subject to both constant normal load, P , and constant tangential load, Q .*

It is important to highlight that Boussinesq studies (Boussinesq, 1885) allow to affirm that the normal displacement on contact surface is proportional, for each body, to the value $G/1-2\nu$, where G represents the tangential elastic modulus. Thus, by considering *Equation (2.21)*, it can be written:

$$\frac{G_1}{1-2\nu_1}\bar{u}_{z1}(x,y)=-\frac{G_2}{1-2\nu_2}\bar{u}_{z2}(x,y) \qquad (2.22)$$

where $\bar{u}_{z1}(x,y)$ and $\bar{u}_{z2}(x,y)$ represent the displacements of points lying on the contact surface of body 1 and body 2, respectively. The Poisson coefficients ν_1 and ν_2 and the tangential elastic moduli G_1 and G_2 are related to body 1 and body 2, respectively.

Equation (2.22) shows that, if the two bodies in contact are characterised by the same elastic properties, the tangential forces transmitted between them give rise to normal displacements in body 1 that are equal to those in body 2, with opposite

direction. Therefore, the size and shape of the contact area is not affected by the deformation of the surfaces. Consequently, such an area does not depend on the tangential load Q, and is function of the normal load P only.

On the other hand, if the two bodies are characterised by different mechanical properties, the normal pressure distribution, $p(x)$, and the size and shape of the contact surface are influenced by the presence of the tangential load. Such an influence was analysed by Bufler (Bufler, 1959), who analytically proved that the presence of a tangential load causes both the shifting of centre and the increasing of size of the contact surface. Nevertheless, such an influence is negligible for small values of friction coefficient, typical of mechanical applications.

Therefore, in the following, the stresses and deformation due to the normal pressure are assumed to be independent of the stresses and deformation due to the tangential traction. In more detail, the superposition principle is used in order to define both stress and deformation fields.

As far as both a constant normal load, P, and a constant tangential load, Q, are present, two cases may arise:

i) Total slip between the bodies, that is, the tangential force can be determined as a function of the normal load, by means of the friction coefficient μ ($Q = \mu P$);

ii) Partial slip between the bodies, that is, even if no relative motions arise, additional stresses due to friction are induced to the contact surface ($Q < \mu P$).

In the present Ph.D. Thesis, contact problems in partial slip conditions are analysed, due to the fact that total slip is rare in most of the structural components affected by contact problems (Hills, 1994). Moreover, as was highlighted by Madge et al. (Madge, 2007) and Araújo (Araújo, 2015), the most significant reduction of fatigue life occurs in partial slip regime.

Therefore, let us consider two bodies subject to a constant normal load, P, and a constant tangential load, Q, characterised by a partial slip regime, that is, $Q < \mu P$ (***Figure 2.9***).

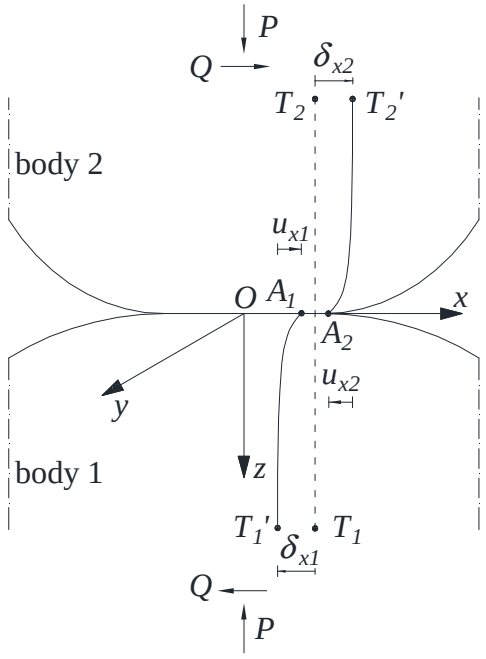

Figure 2.9 *Contact between non-conforming bodies, characterized by different general profiles: deformation due to both constant normal load, P, and constant tangential load, Q.*

As far as partial slip regime is concerned, at least one point laying on the contact surface is not affected by relative motion. More precisely, the contact region consists of two areas: the *slip* zone and the *stick* one. The first one is characterised by a relative slip between the contact surfaces, whereas the latter presents a prefect adherence between the contact surfaces, without relative motions.

Let us consider two points T_1 and T_2 reasonably distant from the contact surface, with the corresponding displacements δ_{x1} and δ_{x2}, and two points A_1 and A_2 on the contact surface, with the corresponding displacements, $\bar{u}_{x1}$ and $\bar{u}_{x2}$. The absolute displacement s_x in the x direction between A_1 and A_2 may be expressed as follows:

$$s_x = s_{x1} - s_{x2} = \left(\bar{u}_{x1} - \delta_{x1}\right) - \left(\bar{u}_{x2} - \delta_{x2}\right) = \left(\bar{u}_{x1} - \bar{u}_{x2}\right) - \left(\delta_{x1} - \delta_{x2}\right) \qquad (2.23)$$

whereas the absolute displacement s_y in the y direction may be expressed by:

$$s_y = s_{y1} - s_{y2} = \left(\bar{u}_{y1} - \delta_{y1}\right) - \left(\bar{u}_{y2} - \delta_{y2}\right) = \left(\bar{u}_{y1} - \bar{u}_{y2}\right) - \left(\delta_{y1} - \delta_{y2}\right) \qquad (2.24)$$

In the case of points A_1 and A_2 located within the stick region, the absolute displacements s_x and s_y are equal to zero and no relative motion arises. Consequently, *Equations (2.23)* and *(2.24)* become:

$$\bar{u}_{x1} - \bar{u}_{x2} = \delta_{x1} - \delta_{x2} \qquad (2.25a)$$

$$\bar{u}_{y1} - \bar{u}_{y2} = \delta_{y1} - \delta_{y2} \qquad (2.25b)$$

It is possible to remark that all the points within the stick region undergo the same displacement, regardless of the position of A_1 and A_2. Moreover, if the two bodies are characterised by the same value of elastic modulus, they are subjected to the same distribution of tangential load and thus, by considering *Equation (2.21)*, it is possible to obtain:

$$\bar{u}_{x1} = -\bar{u}_{x2} \qquad (2.26a)$$

$$\bar{u}_{y1} = -\bar{u}_{y2} \qquad (2.26b)$$

Moreover, in order to assure that within the stick region no slip arises between the bodies, the contact shear distribution, $q(x, y)$, must undergo the following condition:

$$\left|q(x,y)\right| < \mu \left|p(x,y)\right| \qquad (2.27)$$

On the other hand, within the slip regions, where slip between bodies arises, the conditions of *Equation (2.25)* can not be applied, and the condition of *Equation (2.27)* becomes:

$$\left|q(x,y)\right| = \mu \left|p(x,y)\right| \qquad (2.28)$$

Moreover, as a consequence of the physical nature of the phenomena, the contact shear distribution needs to have a direction opposite to that of the relative slip between the bodies, $s(x,y)$. More precisely, the following condition holds:

$$\frac{q(x,y)}{\left|q(x,y)\right|} = -\frac{s(x,y)}{\left|s(x,y)\right|} \qquad (2.29)$$

Note that *Equations (2.25)* and *(2.27)* provide the boundary conditions for the stick region, whereas *Equations (2.28)* and *(2.29)* provide the boundary conditions for the slip region. Since the distributions of tractions and displacements that satisfy such conditions are not known in advance, it is useful to start by assuming that the stick region covers the whole contact area.

As far as two cylindrical bodies in contact along their longitudinal axes are concerned, the half-width a of the contact area and the contact pressure distribution $p(x)$ are determined through the Hertzian theory.

Firstly, let us assume that the value of the friction coefficient is sufficiently high to prevent relative slip throughout the whole contact surface, that is, *Equations (2.38)* hold for $-a \le x \le a$. In such a condition, each point on the contact surface experiences the same displacement and thus, according to the theory of elastic half-space, the loading distribution is characterised by the shape shown in ***Figure 2.10***, and its expression is equal to:

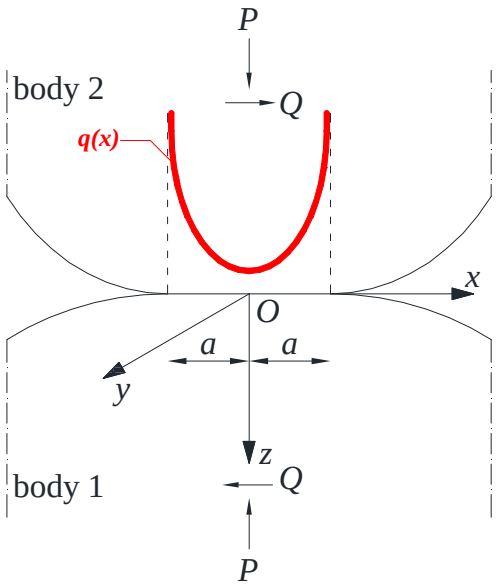

Figure 2.10 *Contact shear distribution, $q(x)$, due to constant tangential displacements at the interface of cylindrical bodies, subject to both constant normal load, P, and constant tangential load, Q.*

$$q(x) = \frac{Q}{\pi\sqrt{a^2 - x^2}} \qquad (2.30)$$

The contact shear distribution is highlighted to tend to infinite at the contact edges ($x = \pm a$). However, such a condition is incompatible with the initial hypothesis of total adherence, since it would require a friction coefficient also tending to infinite. As a consequence, relative slips should arise at the edges of the contact zone, where $q(x)$ reaches high values, whereas adherence is expected in the inner region.

Now let us consider a partial slip condition, with the tangential load Q equal to μP. The solution for such a case was firstly proposed by Cattaneo (Cattaneo, 1938) and, independently, by Mindlin (Mindlin, 1949). The contact shear distribution, $q'(x)$, may be expressed by means of the Hertzian theory:

$$q'(x) = \mu p(x) = \frac{\mu p_0}{a}\sqrt{a^2 - x^2} \qquad (2.31)$$

Moreover, the tangential displacements due to $q'(x)$ may be determined in a similar way to that used for the normal displacements due to an Hertzian contact pressure distribution. More precisely, in the case of absence of slip in $x = 0$, it is possible to obtain:

$$\bar{u}'_{x1} = \delta'_{x1} - \frac{\left(1-\nu_1^2\right)\mu p_0 x^2}{aE_1} \qquad (2.32a)$$

$$\bar{u}'_{x2} = -\delta'_{x2} + \frac{\left(1-\nu_2^2\right)\mu p_0 x^2}{aE_2} \qquad (2.32b)$$

As far as points within the zone $-c \le x \le c$ (***Figure 2.11***) are concerned, an additional contribution, $q''(x)$, to the contact shear distribution needs to be taken into account:

$$q''(x) = -\frac{\mu p_0}{a}\sqrt{c^2 - x^2} \qquad (2.33)$$

The tangential displacements due to $q''(x)$ are equal to:

$$\bar{u}''_{x1} = -\delta''_{x1} + \frac{c}{a}\frac{\left(1-\nu_1^2\right)\mu p_0 x^2}{cE_1} \qquad (2.34a)$$

$$\bar{u}''_{x2} = \delta''_{x2} - \frac{c}{a}\frac{\left(1-\nu_2^2\right)\mu p_0 x^2}{cE_2} \qquad (2.34b)$$

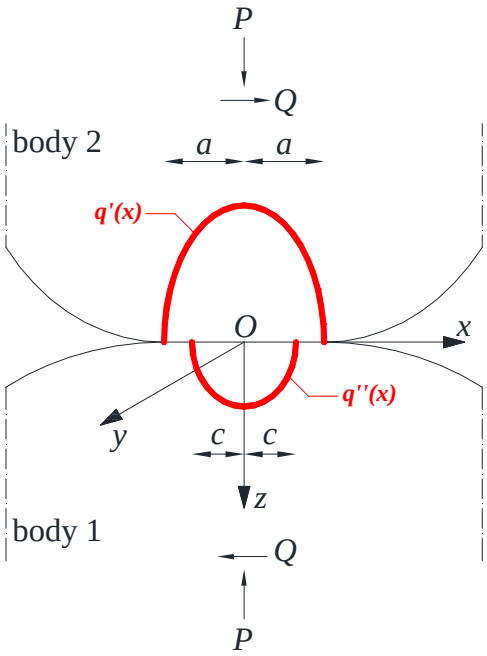

Figure 2.11 *Contact shear distributions, $q'(x)$ and $q''(x)$, at the interface of cylindrical bodies, subject to both constant normal load, P, and tangential load, Q.*

Then, the resultant tangential displacements, $\bar{u}_{x1}$ and $\bar{u}_{x2}$, are determined by superposing the effects produced by $q'(x)$ with those produced by $q''(x)$:

$$\bar{u}_{x1} = \bar{u}'_{x1} + \bar{u}''_{x1} = \delta'_{x1} - \delta''_{x1} = \delta_{x1} \qquad (2.35a)$$

$$\bar{u}_{x2} = \bar{u}'_{x2} + \bar{u}''_{x2} = -\delta'_{x2} + \delta''_{x2} = -\delta_{x2} \qquad (2.35b)$$

By analysing *Equations (2.35)*, it can be noted that the displacements within the region $-c \le x \le c$ are constant. More precisely, by substituting *Equations (2.35)* in *Equation (2.25a)*, the condition of perfect adherence between the two surfaces is satisfied. Moreover, the contact shear distribution in such a region is equal to:

$$q(x) = q'(x) + q''(x) = \frac{\mu p_0}{a}\left(\sqrt{a^2 - x^2} - \sqrt{c^2 - x^2}\right) \qquad (2.36)$$

Note that, since $c < a$, $q(x)$ is lower than the maximum value, $\mu p(x)$, related to the slip condition. Therefore, the second condition that ensures the perfect adherence between the bodies, represented by the *Equation (2.27)*, is also satisfied.

On the other hand, as far as points within the zone $c \le |x| \le a$ are concerned, the condition represented by *Equation (2.28)* for slip regions is automatically satisfied when $q'(x)$ is determined, as is reported in *Equation (2.31)*.

Then, in order to satisfy also the condition concerning the direction of displacements, represented by *Equation (2.29)*, the displacement field produced by an elliptical contact shear distribution is required. Such displacements, $\bar{u}_{x1}$, have been evaluated by Poritsky (Poritsky, 1950) and are qualitatively plotted in ***Figure 2.12***.

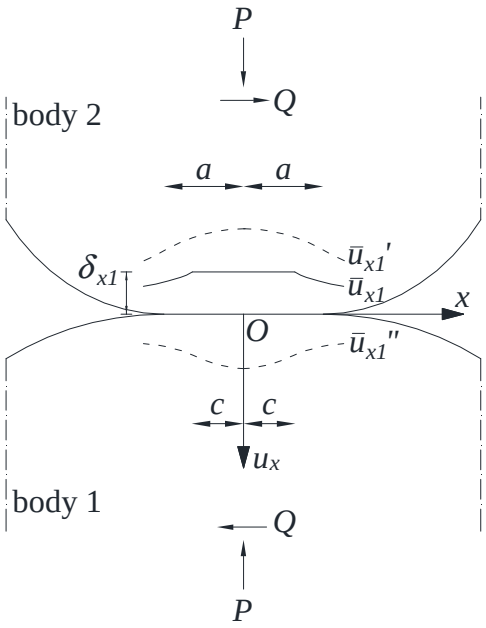

Figure 2.12 *Qualitative shape of* $\bar{u}_{x1}$, $\bar{u}'_{x1}$ *and* $\bar{u}''_{x1}$ *displacement fields.*

The absolute slip between two points lying on the contact surface is given by *Equation (2.23)*:

$$s_x = \left(\bar{u}_{x1} - \bar{u}_{x2}\right) - \delta_x \qquad (2.37)$$

Note that the value of $\bar{u}_{x1}$ is lower than that of δ_{x1} in each point of the slip region (***Figure 2.12***). In the same way, it is possible to demonstrate that the value of $\bar{u}_{x2}$ is lower than that of δ_{x2} within the slip region. Therefore, by considering *Equation (2.37)*, it is possible to deduce that the absolute slip s_x is negative and thus its direction is opposite with respect to the contact shear distribution.

Moreover, Johnson (Johnson, 1985) demonstrated that the contact shear distribution qualitatively shown in ***Figure 2.13*** and given by:

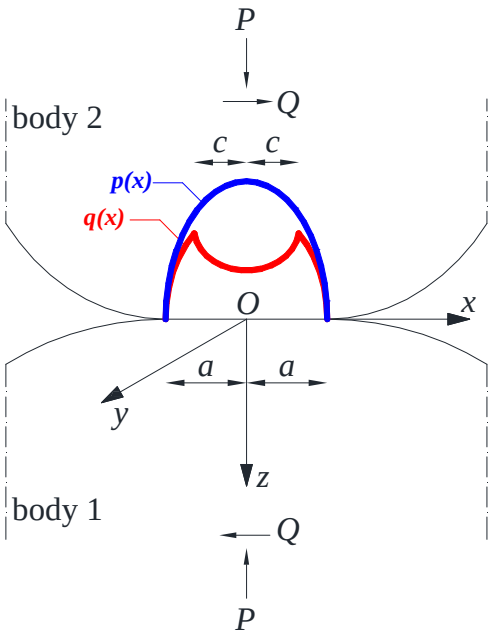

Figure 2.13 *Contact pressure distribution, $p(x)$, and contact shear distribution, $q(x)$, at the interface of cylindrical bodies, subject to both constant normal load, P, and*

constant tangential load, Q.

$$q(x)=\begin{cases}\dfrac{\mu p_0}{a}\sqrt{a^2-x^2} & \text{for } c\le|x|\le a\\ \dfrac{\mu p_0}{a}\left(\sqrt{a^2-x^2}-\sqrt{c^2-x^2}\right) & \text{for } |x|<c\end{cases} \qquad (2.38)$$

together with the contact pressure distribution, satisfies the boundary conditions both within ($-c\le x\le c$) and outside ($c\le|x|\le a$) the stick region.

Furthermore, the size of the stick region may be determined by imposing the equilibrium of tangential forces as follows:

$$Q=\int_{-a}^{a}q(x)\,dx=\int_{-a}^{a}q'(x)\,dx+\int_{-c}^{c}q''(x)\,dx=\mu P-\left(\frac{c}{a}\right)^2\mu P \qquad (2.39)$$

so that:

$$c=a\sqrt{1-\frac{Q}{\mu P}} \qquad (2.40)$$

It is important to highlight that, as P is kept constant whereas Q is progressively increased, a slip region appears at the edges of the contact surface and progressively spreads inwards the contact area. As Q approaches the limit value of slip ($Q=\mu P$), the stick region shrinks to a line ($c=0$), and a further increase of tangential load causes a total slip between the bodies.

The determination of stresses due to cylindrical contact in the presence of a static tangential load, Q, may be deduced by employing the results determined by McEwen (McEwen, 1949) for the case of normal load, as is reported in *Section 2.3.1*. In more detail, because the contact shear distribution is directly proportional to the contact pressure distribution by means of the friction coefficient, the

components of the stress tensor produced by a general tangential load Q in the vicinity of the contact zone are given by (Johnson, 1985; Vantadori, 2017):

$$\sigma_x^Q = \begin{cases} \dfrac{\mu p_0}{a}\left\{\left[n\left(2-\dfrac{z^2-m^2}{m^2+n^2}\right)-2x\right]-\left[n_c\left(2-\dfrac{z^2-m_c^2}{m_c^2+n_c^2}\right)-2x\right]\right\} \\ \text{for } x \geq 0 \\ \dfrac{\mu p_0}{a}\left\{-\left[n\left(2-\dfrac{z^2-m^2}{m^2+n^2}\right)+2x\right]+\left[n_c\left(2-\dfrac{z^2-m_c^2}{m_c^2+n_c^2}\right)+2x\right]\right\} \\ \text{for } x < 0 \end{cases} \tag{2.41a}$$

$$\sigma_z^Q = \begin{cases} \dfrac{\mu p_0}{a}\left[-n\left(\dfrac{m^2-z^2}{m^2+n^2}\right)+n_c\left(\dfrac{m_c^2-z^2}{m_c^2+n_c^2}\right)\right] & \text{for } x \geq 0 \\ \dfrac{\mu p_0}{a}\left[n\left(\dfrac{m^2-z^2}{m^2+n^2}\right)-n_c\left(\dfrac{m_c^2-z^2}{m_c^2+n_c^2}\right)\right] & \text{for } x < 0 \end{cases} \tag{2.41b}$$

$$\tau_{xz}^Q = \frac{\mu p_0}{a}\left\{-\left[m\left(1+\frac{z^2+n^2}{m^2+n^2}\right)-2z\right]+\left[m_c\left(1+\frac{z^2+n_c^2}{m_c^2+n_c^2}\right)-2z\right]\right\} \tag{2.41c}$$

where the functions m_c and n_c are given by:

$$m_c^2 = \frac{1}{2}\left[\sqrt{\left(c^2-x^2+z^2\right)^2+4x^2z^2}+\left(c^2-x^2+z^2\right)\right] \tag{2.42a}$$

$$n_c^2 = \frac{1}{2}\left[\sqrt{\left(c^2-x^2+z^2\right)^2+4x^2z^2}-\left(c^2-x^2+z^2\right)\right] \tag{2.42b}$$

Finally, the stress tensor may be determined by means of the superposition principle:

$$\sigma_x = \sigma_x^P + \sigma_x^Q \qquad (2.43a)$$

$$\sigma_z = \sigma_z^P + \sigma_z^Q \qquad (2.43b)$$

$$\tau_{xz} = \tau_{xz}^P + \tau_{xz}^Q \qquad (2.43c)$$

where σ_x^P, σ_z^P and τ_{xz}^P represent the components of the stress tensor due to a constant normal load, P, determined in Section 2.4.1 (*Equations (2.19)*).

2.4.3 Cyclic tangential load in contact problems

In the previous Sections, the contact problem characterised by loads in static regime has been analysed. On the other hand, fretting fatigue is generally characterized by cyclic tangential loads, $Q(t)$, that vary between two limiting values, Q_{max} and Q_{min}, over time.

It is important to highlight that the contact shear distribution for cylindrical contact, obtained in Section 2.4.2 and reported in *Equation (2.38)*, is limited to the time instants corresponding to such limiting values. The analysis of contact shear distribution in a general time instant, $Q_{min} < Q(t) < Q_{max}$, is thus of interest. Therefore, the influence of a cyclic tangential force, $Q(t) = Q_a sen(\omega t)$ characterised by an amplitude Q_a, on both stress and displacement fields within two bodies in contact is analysed in the present Section.

Let us consider the time history shown in ***Figure 2.14***.

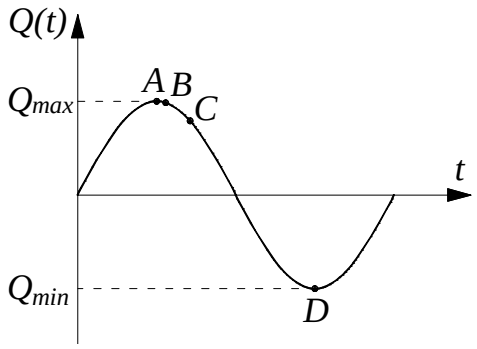

Figure 2.14 *Time history of cyclic tangential load,* $Q(t)$.

Points A and D correspond to Q_{max} and Q_{min}, respectively. By starting from point A, an infinitesimal decrease of tangential load (point B in ***Figure 2.14***) implies that the displacements variation over time is characterised by an opposite direction with respect to that in correspondence of time instants of increasing tangential load, and that means:

$$\frac{\left(\frac{\partial\left[u_1(t)-u_2(t)\right]}{\partial t}\right)_{t=B}}{\left|\left(\frac{\partial\left[u_1(t)-u_2(t)\right]}{\partial t}\right)_{t=B}\right|}=-\frac{\left(\frac{\partial\left[u_1(t)-u_2(t)\right]}{\partial t}\right)_{t=A}}{\left|\left(\frac{\partial\left[u_1(t)-u_2(t)\right]}{\partial t}\right)_{t=A}\right|} \qquad (2.44)$$

As a consequence, the condition represented by *Equation (2.28)* is no longer satisfied, and a perfect adherence arises on the whole contact surface.

Furthermore, an additional decrease of the tangential load (from point B to point C in ***Figure 2.14***) gives rise to a *reverse slip* at the edges of the contact surface ($c \le |x| \le a$). In such an area, the contact shear distributions reported in *Equation (2.38)* need to be changed in sign in order to satisfy *Equation (2.29)* (Hills, 1994).

Let us consider two cylindrical bodies in contact along their longitudinal axes, subject to a constant normal load P, and a cyclic tangential load $Q(t)$ (***Figure 2.15***).

It is possible to demonstrate (Johnson, 1985) that an additional contribution, $q'''(x,t)$, to the contact shear distribution reported in *Equation (2.38)* has to be taken into account in order to satisfy the boundary conditions:

$$q'''(x) = \frac{2\mu p_0}{a}\sqrt{c'(t)^2 - x^2} \qquad (2.45)$$

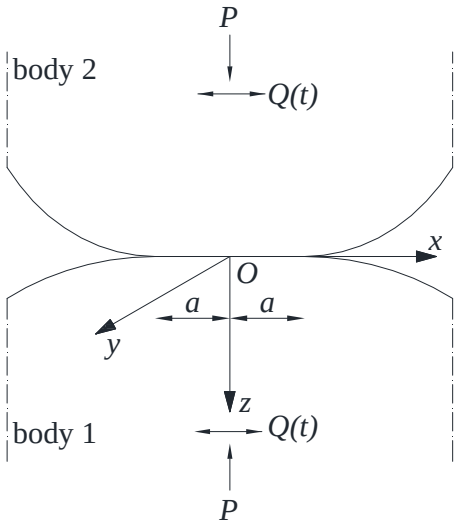

Figure 2.15 *Contact between cylindrical bodies, subject to both constant normal, P, and cyclic tangential load, $Q(t)$.*

where $c'(t)$ represents the instantaneous half-width of the stick region. Therefore, for a general time instant, the contact shear distribution is qualitatively shown in ***Figure 2.16***, and *Equation (2.38)* becomes:

$$q(x)=\begin{cases} -\dfrac{\mu p_0}{a}\sqrt{a^2-x^2} \\ \text{for } c'(t)\le|x|\le a \\ -\dfrac{\mu p_0}{a}\left[\sqrt{a^2-x^2}-2\sqrt{c'(t)^2-x^2}\right] \\ \text{for } c\le|x|<c'(t) \\ -\dfrac{\mu p_0}{a}\left[\sqrt{a^2-x^2}-2\sqrt{c'(t)^2-x^2}+\sqrt{c^2-x^2}\right] \\ \text{for } |x|<c \end{cases} \qquad (2.46)$$

Moreover, $c'(t)$ may be determined by imposing the equilibrium of tangential forces, in a similar way to that reported in *Equation (2.39)*:

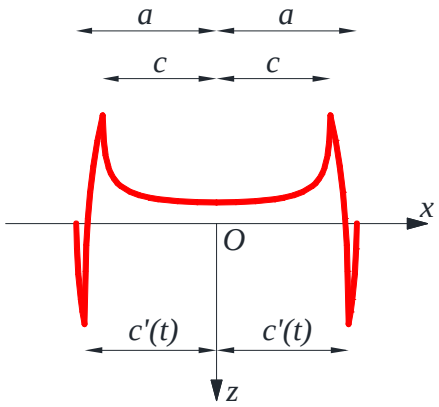

Figure 2.16 *Qualitative contact shear distribution* $q(x,t)$ *due to cyclic tangential load,* $Q(t)$.

$$c'(t)=a\sqrt{1-\frac{Q_{max}-Q(t)}{2\mu P}} \qquad (2.47)$$

Note that the value of the half-width c of the stick region remains constant during the whole cycle, and may be determined as follows:

$$c = a\sqrt{1 - \frac{Q_a}{\mu P}} \qquad (2.48)$$

2.4.4 Cyclic bulk load in contact problems

Fretting fatigue occurs in presence of a cyclic load (or a cyclic stress), named bulk load (or bulk stress), caused by an external source and applied to at least one of the two bodies in contact. The influence of such a load on the contact stress field within two bodies in contact is analysed in the present Section.

Let us consider two cylindrical bodies in contact along their longitudinal axes, subject to a constant normal load P and a cyclic tangential load $Q(t) = Q_a sen(\omega t)$, varying according to the time history shown in ***Figure 2.14***. Moreover, a cyclic bulk stress, $\sigma_B(t) = \sigma_{B,m} + \sigma_{B,a} sen(\omega t)$, characterised by an amplitude $\sigma_{B,a}$ and a mean value $\sigma_{B,m}$, in phase with $Q(t)$, is applied to one of the two bodies in contact (***Figure 2.17***).

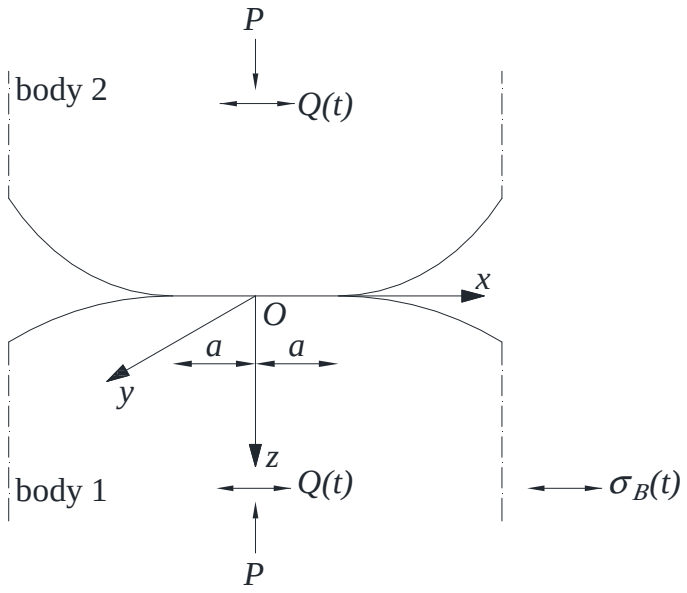

Figure 2.17 *Contact between cylindrical bodies, subject to both constant normal load, P , cyclic tangential load, $Q(t)$, and cyclic bulk stress, $\sigma_B(t)$.*

By assuming a linear elastic behaviour, the stress field due to the cyclic bulk stress may be taken into account by means of the superposition principle. Nevertheless, in the body where such a stress is applied, a deformation arises. Such a deformation is not experienced by the other body and, consequently, the deformation states of the two bodies at the contact surface are not conforming.

According to Hills and Nowell (Hills, 1994), the presence of $\sigma_B(t)$ promotes an eccentricity e of the stick zone towards the contact trailing edge. At the time instant for which $Q(t)$ attains its maximum value, the value of e can be computed by means of the following expression:

$$e = a\frac{\sigma_{B,a}}{4\mu p_0} \qquad (2.49)$$

Note that such an expression only holds in partial-slip regime, that is, with small values of $\sigma_{B,a}$ and, in particular, the following condition needs to be satisfied:

$$\sigma_{B,a} \le 4\mu p_0 \left(1-\sqrt{1-\frac{Q_a}{\mu P}}\right) \tag{2.50}$$

Moreover, at the time instants when $Q(t)$ attains both its maximum and minimum values, the contact shear distribution is qualitatively shown in ***Figure 2.18***, and *Equations (2.38)* and *(2.46)* become:

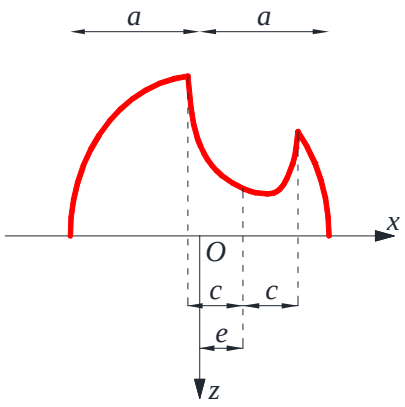

Figure 2.18 *Qualitative contact shear distribution* $q(x,t)$ *due to both cyclic tangential load,* $Q(t)$*, and cyclic bulk stress,* $\sigma_B(t)$*, when they attain their maximum values.*

$$q(x)=\begin{cases}\dfrac{\mu p_0}{a}\sqrt{a^2-x^2} \\ \text{for } -a\le x<-c+e \\ \dfrac{\mu p_0}{a}\left[\sqrt{a^2-x^2}-\sqrt{c^2-(x-e)^2}\right] \\ \text{for } -c+e\le x\le c+e \\ \dfrac{\mu p_0}{a}\sqrt{a^2-x^2} \\ \text{for } c+e<x\le a\end{cases} \qquad (2.51)$$

The contact shear distribution $q(x,t)$ in a general time instant is qualitatively shown in ***Figure 2.19***, and *Equation (2.51)* may be generalised as follows:

$$q(x)=\begin{cases}-\dfrac{\mu p_0}{a}\sqrt{a^2-x^2} \\ \text{for } -a\le x<-c'(t)+e'(t) \\ -\dfrac{\mu p_0}{a}\left\{\sqrt{a^2-x^2}-2\sqrt{c'(t)^2-\left[x-e'(t)\right]^2}\right\} \\ \text{for } -c'(t)+e'(t)\le x<-c+e \\ -\dfrac{\mu p_0}{a}\left\{\sqrt{a^2-x^2}-2\sqrt{c'(t)^2-\left[x-e'(t)\right]^2}+\sqrt{c^2-(x-e)^2}\right\} \\ \text{for } -c+e\le x\le c+e \\ -\dfrac{\mu p_0}{a}\left\{\sqrt{a^2-x^2}-2\sqrt{c'(t)^2-\left[x-e'(t)\right]^2}\right\} \\ \text{for } c+e<x\le c'(t)+e'(t) \\ -\dfrac{\mu p_0}{a}\sqrt{a^2-x^2} \\ \text{for } c'(t)+e'(t)<x\le a\end{cases} \qquad (2.52)$$

being $e'(t)$ the instantaneous eccentricity of the stick region:

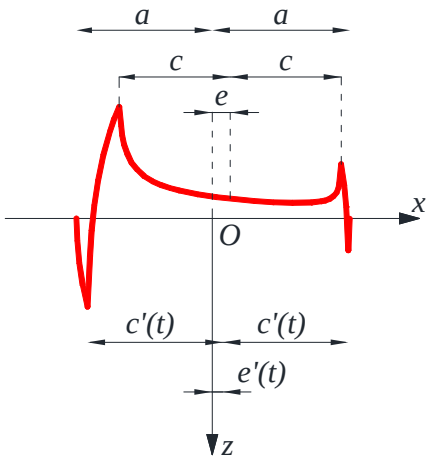

Figure 2.19 *Qualitative contact shear distribution* $q(x,t)$ *due to both cyclic tangential load,* $Q(t)$*, and cyclic bulk stress,* $\sigma_B(t)$*, at a general time instant.*

$$e'(t)=\frac{a}{8\mu p_0}\left[\sigma_{B,max}-\sigma_B(t)\right] \tag{2.53}$$

The stresses due to cylindrical contact in the presence of a cyclic tangential load $Q(t)$ and a cyclic bulk stress $\sigma_B(t)$, in phase with $Q(t)$ and applied to one of the two bodies in contact, may be deduced by employing the results determined by McEwen (McEwen, 1949) for the case of normal load, as is reported in *Section 2.4.1*. In more detail, the components of the stress tensor, produced by a cyclic tangential load, in the vicinity of the contact zone at the time instant when $Q(t)$ attains its maximum value, are given by (Johnson, 1985; Vantadori, 2020):

$$\sigma_x^Q = \begin{cases} \dfrac{\mu p_0}{a}\left\{\left[n\left(2-\dfrac{z^2-m^2}{m^2+n^2}\right)-2x\right]-\left[n_e\left(2-\dfrac{z^2-m_e^2}{m_e^2+n_e^2}\right)-2|x-e|\right]\right\} \\ \text{for } x \geq 0 \\ \dfrac{\mu p_0}{a}\left\{-\left[n\left(2-\dfrac{z^2-m^2}{m^2+n^2}\right)+2x\right]+\left[n_e\left(2-\dfrac{z^2-m_e^2}{m_e^2+n_e^2}\right)-2|x-e|\right]\right\} \\ \text{for } x < 0 \end{cases} \qquad (2.54a)$$

$$\sigma_z^Q = \begin{cases} \dfrac{\mu p_0}{a}\left[-n\left(\dfrac{m^2-z^2}{m^2+n^2}\right)+n_e\left(\dfrac{m_e^2-z^2}{m_e^2+n_e^2}\right)\right] & \text{for } x \geq 0 \\ \dfrac{\mu p_0}{a}\left[n\left(\dfrac{m^2-z^2}{m^2+n^2}\right)-n_e\left(\dfrac{m_e^2-z^2}{m_e^2+n_e^2}\right)\right] & \text{for } x < 0 \end{cases} \qquad (2.54b)$$

$$\tau_{xz}^Q = \frac{\mu p_0}{a}\left\{-\left[m\left(1+\frac{z^2+n^2}{m^2+n^2}\right)-2z\right]+\left[m_e\left(1+\frac{z^2+n_e^2}{m_e^2+n_e^2}\right)-2z\right]\right\} \qquad (2.54c)$$

where the functions m_e and n_e are given by:

$$m_e^2 = \frac{1}{2}\left\{\sqrt{\left[c^2-(x-e)^2+z^2\right]^2+4(x-e)^2z^2}+\left[c^2-(x-e)^2+z^2\right]\right\} \qquad (2.55a)$$

$$n_e^2 = \frac{1}{2}\left\{\sqrt{\left[c^2-(x-e)^2+z^2\right]^2+4(x-e)^2z^2}-\left[c^2-(x-e)^2+z^2\right]\right\} \qquad (2.55b)$$

In ***Figure 2.20***, the stress component profiles due to fretting loading in correspondence of the xz plane are shown, at the trailing edge of the contact zone (that is $x=a$), due to the normal load (***Figure 2.20(a)***) and the tangential load (***Figure 2.20(b)***).

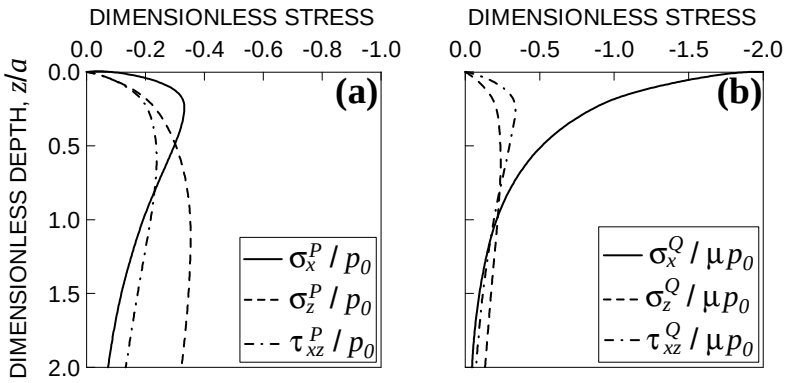

Figure 2.20 *Stress component profiles at the trailing edge of the contact zone ($x = a$), due to: (a) constant normal load, P , and (b) cyclic tangential load, $Q(t)$.*

Moreover, the direct contribution of the cyclic bulk stress to the stress field consists of a normal stress component. In particular, the expression of such a stress component, at the time instant for which both $Q(t)$ and $\sigma_B(t)$ attain their maximum values, is given by:

$$\sigma_x^B = \sigma_{B,m} + \sigma_{B,a} \tag{2.56}$$

Finally, by superimposing the stress contributions due to the constant normal load (*Equations (2.19)*), the cyclic tangential load (*Equations (2.54)*) and the cyclic bulk load (*Equation (2.56)*), the specimen stress tensor due to fretting fatigue loading can be evaluated. In particular, at the time instant in correspondence to the maximum value of both bulk stress and tangential force, the stress components turn out to be:

$$\sigma_x = \sigma_x^P + \sigma_x^Q + \sigma_x^B \tag{2.57a}$$

$$\sigma_z = \sigma_z^P + \sigma_z^Q \tag{2.57b}$$

$$\tau_{xz} = \tau_{xz}^{P} + \tau_{xz}^{Q} \qquad (2.57c)$$

It should be highlighted that $\sigma_y = \nu\left(\sigma_x + \sigma_z\right)$ due to plane strain condition.

2.5 References

Araújo J.A., Nowell D. Mixed high low fretting fatigue of Ti6Al4V: Test and modelling. *Tribology International*, 2009; 42: 1276–1285.

Araújo J.A., Bellecave J., Castro F.C., Mériaux J., Pommier S. Equivalent configurations for notch and fretting fatigue. *Frattura ed Integrità Strutturale*, 2015; 33: 427-433.

Araújo J.A., Castro F.C., Pommier S., Bellecave J., Meriaux J. On the design and test of equivalent configurations for notch and fretting fatigue. *Fatigue and Fracture of Engineering Materials and Structures*, 2016; 39: 1241-1250.

Araújo J.A., Almeida G.M.J., Ferreira J.L.A., da Silva C.R.M., Castro F.C. Early cracking orientation under high stress gradients: The fretting case. *International Journal of Fatigue*, 2017; 100: 611-618.

Araújo J.A., Castro F.C., Matos I.M., Cardoso R.A. Life prediction in multiaxial high cycle fretting fatigue. *International Journal of Fatigue*, 2020; 134, 105504.

Berthier Y., Vincent L., Godet M. Fretting fatigue and fretting wear. *Tribology International*, 1989; 22: 235-242.

Bhattacharya B., Ellingwood B. Continuum damage mechanics analysis of fatigue crack initiation. *International Journal of Fatigue*, 1998; 20: 631-639.

Bhatti N.A., Wahab M.A. Fretting fatigue crack nucleation: A review. *Tribology International*, 2018; 121: 121-138.

Bogy D.B. Edge-bonded dissimilar orthogonal elastic wedges under normal and shear loading. *Journal of Applied Mechanics*, 1968; 35, 3: 460.

Boussinesq J. *Application des Potentials à l'etude de l'équilibre et du mouvement des solides éelastiques*. Gauthier-Villars: Paris; 1885.

Brown M.W., Miller K.J. A theory for fatigue under multiaxial stress-strain conditions. In: *A Theory for Fatigue Under Multiaxial Stress-Strain Conditions*. *Proceedings of the Institution of Mechanical Engineers*, 1973; 187: 745-756.

Bufler H. Zur Theorie der rollenden Reibung. *Ingenieur Archiv*, 1959; 27: 137-152.

Carpinteri A., Spagnoli A., Vantadori S. Multiaxial fatigue assessment using a simplified critical plane-based criterion. *International Journal of Fatigue*, 2011; 33: 969-976.

Cattaneo C. Sul contatto di due corpi elastici: distribuzione locale degli sforzi. *Rendiconti dell'Accademia Nazionale dei Lincei*, 1938; 27, 6: 342–8.

Chaboche J.L., Lesne P.M. A non-linear continuous fatigue damage model. *Fatigue and Fracture of Engineering Materials and Structures*, 1988; 11: 1-17.

Crossland B. Effect of large hydrostatic pressures on the torsional fatigue strength of an alloy steel. *Proceedings of International Conference on Fatigue of Metals*, 1956: 138-149.

Davies M., Barber J., Hills D. Energy dissipation in a frictional incomplete contact with varying normal load. *International Journal of Mechanical Sciences*, 2012; 55, 1: 13–21.

Dini D., Hills D.A. Bounded asymptotic solutions for incomplete contacts in partial slip. *International Journal of Solids and Structures*, 2004; 41, 24–25: 7049–62.

Endo K., Goto H. Initiation and propagation of fretting fatigue cracks. *Wear*, 1976; 38: 311-324.

Fatemi A., Socie D.F. A critical plane approach to multiaxial fatigue damage including out-of-phase loading. *Fatigue and Fracture of Engineering Materials and Structures*, 1988; 11: 149-165.

Findley W.N. A theory for the effect of mean stress on fatigue of metals under combined torsion and axial load or bending. *Journal of Engineering for Industry*, 1959; 301-306.

Fleury R., Hills D., Ramesh R., Barber J. Incomplete contacts in partial slip subject to varying normal and shear loading, and their representation by asymptotes. *Journal of the Mechanics and Physics of Solids*, 2017; 99: 178–91.

Fouvry S., Nowell D., Kubiak K., Hills D. Prediction of fretting crack propagation based on a short crack methodology. *Engineering Fracture Mechanics*, 2008; 75, 6: 1605–22.

Gandiolle C., Fouvry S. Experimental analysis and modeling of the crack arrest condition under severe plastic fretting fatigue conditions. *Procedia Engineering*, 2013; 66: 783–92.

Giannakopoulos A., Lindley T., Suresh S. Aspects of equivalence between contact mechanics and fracture mechanics: theoretical connections and a life-prediction methodology for fretting-fatigue. *Acta Materialia*, 1998; 46, 9: 2955–68.

Giner E., Sukumar N., Fuenmayor F.J., Vercher A. Singularity enrichment for complete sliding contact using the partition of unity finite element method.

International Journal for Numerical Methods in Engineering, 2008; 76, 9: 1402–18.

Hannel S., Fouvry S., Kapsa Ph., Vincent L. The fretting sliding transition as a criterion for electrical contact performance. *Wear*, 2001; 249: 761–70.

Heredia S., Fouvry S. Introduction of a new sliding regime criterion to quantify partial, mixed and gross slip fretting regimes: correlation with wear and cracking processes. *Wear*, 2010; 269: 515–24.

Hertz H. Ueber die beruhrung fester elastischer korper. *Journal für die reine und angewandte Mathematik*, 1882; 92: 156–71.

Hertz H. *Miscellaneous Paper by Heinrich Hertz*. New York: Macmillan & Co; 1896.

Hills D.A., Nowell D., O'Connor J.J. On the mechanics of fretting fatigue. *Wear*, 1988; 125: 129-146.

Hills D.A., Nowell D. *Mechanics of Fretting Fatigue*. Kluwer Academic Publishers: Londra; 1994.

Hurricks P.L. Mechanism of fretting. *Wear*, 1970; 15: 389-409.

Jager J. A new principle in contact mechanics. *Journal of Tribology*, 1998; 120, 4: 677–84.

Johnson K.L., Kendall K., Roberts A.D. Surface energy and the contact of elastic solids. *Proceedings of the Royal Society A: Mathematical, Physical and Engineering Sciences*, 1971; 324, 1558: 301–13.

Johnson K.L. *Contact Mechanics*. UK: Cambridge University Press; 1985.

Juoksukangas J., Lehtovaara A., Mäntylä A. Experimental and numerical investigation of fretting fatigue behavior in bolted joints. *Tribology International*, 2016; 103: 440-448.

Lemaitre J. A continuous damage mechanics model for ductile fracture. *Journal of Engineering Materials and Technology*, 1985; 107: 83-89.

Liu K.C. A method based on virtual strain-energy parameters for multiaxial fatigue life prediction. In: McDowell DL, Ellis R, eds. *Advances in Multiaxial Fatigue*. Philadelphia: American Society for Testing and Materials; 1993: 67-84.

Madge J.J., Leen S.B., Shipway P.H. The critical role of fretting wear in the analysis of fretting fatigue. *Wear*, 2007; 263, 1–6: 542–51.

McDiarmid D.L. A general criterion for high cycle multiaxial fatigue failure. *Fatigue and Fracture of Engineering Materials and Structures*, 1991; 14: 429-453.

McEwen E. Stress in elastic cylinders in contact along a generatrix. *Philosophical Magazine*, 1949; 40: 454.

Mindlin R.D. Compliance of elastic bodies in contact. *ASME Journal of Applied Mechanics*, 1949; 16: 259–68.

Moës N., Dolbow J., Belytschko T. A finite element method for crack growth without remeshing. *International Journal for Numerical Methods in Engineering*, 1999; 46, 1: 131–50.

Moraes J.F.C., Rao1 H.M., Jordon J.B., Barkey M.E. High cycle fatigue mechanisms of aluminum self-piercing riveted joints. *Fatigue and Fracture of Engineering Materials and Structures*, 2018; 41: 57-70.

Navarro C., Garcia M., Dominguez J. A procedure for estimating the total life in fretting fatigue. *Fatigue and Fracture of Engineering Materials and Structures*, 2003; 26, 5: 459–68.

Nowell D., Hills D. Mechanics of fretting fatigue tests. *International Journal of Mechanical Sciences*, 1987; 29, 5: 355–65.

Nowell D., Hills D. Crack Initiation criteria in fretting fatigue. *Wear*, 1990; 136, 2: 329-43.

Nowell D. Recent developments in the understanding of fretting fatigue. *Proceeding of the 15th European Conference on Fracture (ECF-15)*, 2005.

Poritsky H. Stresses and deflections of Cylindrical bodies in contact. *ASME Journal of Applied Mechanics*, 1950; 17: 191-201.

Ruiz C., Boddington P.H.B., Chen K.C. An investigation of fatigue and fretting in a dovetail joint. *Experimental Mechanics*, 1984; 24: 208-217.

Said J., Fouvry S., Cailletaud G., Yang C., Hafid F. Shear driven crack arrest investigation under compressive state: prediction of fretting fatigue failure of aluminium strands. *International Journal of Fatigue*, 2020; 136: 105589.

Smith K., Topper T., Watson P. A stress-strain function for the fatigue of metals. *Journal of Materials*, 1970; 5: 767-778.

Sunde S.L., Berto F., Haugen B. Predicting fretting fatigue in engineering design. *International Journal of Fatigue*, 2018; 117: 314-326.

Szolwinski M.P., Farris T.N. Mechanics of fretting fatigue crack formation. *International Journal of Fatigue*, 1997; 19: 39-49.

Taylor D. *The Theory of Critical Distances: A New Perspective in Fracture Mechanics*. UK: Elsevier; 2007.

Vantadori S., Fortese G., Ronchei C., Scorza D. A stress gradient approach for fretting fatigue assessment of metallic structural components. *International Journal of Fatigue*, 2017; 101: 1-8.

Vantadori S., Zanichelli A. Fretting-fatigue analysis of shot-peened aluminium and titanium test specimens. *Fatigue and Fracture of Engineering Materials and Structures*, 2020; In press.

Vingsbo O., Soderberg S. On fretting map. *Wear*, 1988; 126: 131–47.

Walvekar A.A., Leonard B.D., Sadeghi F., Jalalahmadi B., Bolander N. An experimental study and fatigue damage model for fretting fatigue. *Tribology International*, 2014; 79: 183-196.

Waterhouse R.B. *Fretting Corrosion*. UK: Pergamon; 1972.

Waterhouse R.B. Fretting fatigue. *International Materials Reviews*, 1992; 37: 77-97.

Williams M.L. Stress singularities resulting from various boundary conditions in angular corners of plates in extension. *Journal of Applied Mechanics*, 1952; 4, 19: 526–34.

Zhang T., McHugh P., Leen S. Finite element implementation of multiaxial continuum damage mechanics for plain and fretting fatigue. *International Journal of Fatigue*, 2012; 44: 260–72.

Zhou Z.R., Pellerin V., Vincent L. Wear mechanisms in fretting of aluminium alloys. *Proceedings of the second international conference on aluminium alloys*, Beijing, China, 1990; 642–7.

Zhou Z.R., Fayeulle S., Vincent L. Cracking behaviour of various aluminium alloys during fretting wear. *Wear*, 1992; 155: 317–30.

Zhou Z.R., Vincent L. Mixed fretting regime. *Wear*, 1995; 181–183: 531–6.

Zhou Z.R., Nakazawa K., Zhu M.H., Maruyama N., Kapsa Ph., Vincent L. Progress in fretting maps. *Tribology International*, 2006; 39: 1068–73.

3

FORMULATION OF AN ADVANCED METHODOLOGY FOR FRETTING FATIGUE ASSESSMENT

3.1 Introduction

The present Chapter deals with the description of the advanced analytical methodology proposed in the present Ph.D. Thesis for fretting fatigue assessment of structural components. In more detail, such a methodology may be employed in order to evaluate both the initial crack path and the lifetime of metallic structures under fretting fatigue elastic partial slip loading conditions. Consequently, being based on linear-elastic formulations, it could be easily applied to practical situations in the industrial field.

Note that the above methodology has been originally proposed by Carpinteri et al. (Carpinteri, 2019), and some applications are available in the literature (Vantadori, 2020a; Vantadori, 2020b; Vantadori, 2020c; Zanichelli, 2020).

The proposed methodology falls in the category of stress-based critical-plane approach. In particular, the criterion by Carpinteri et al. (Carpinteri, 2011) for metallic structures under multiaxial constant amplitude fatigue loading in high-cycle fatigue regime, originally proposed for plain fatigue conditions and subsequently developed for fatigue assessment of smooth, notched, and welded components characterised by high-cycle fatigue regime (Carpinteri, 2015; Ronchei, 2016), is here extended to the case of fretting fatigue. The Carpinteri et al. criterion is implemented in conjunction with the Critical Direction Method proposed by Araújo et al. (Araújo, 2017), and the philosophy related to the theory of the Critical Distance by Taylor (Taylor, 2007) is also taken into account in the procedure.

More precisely, the proposed advanced methodology consists of the following steps:

i) Firstly, the stress field used as input for the Carpinteri et al. criterion is analytically evaluated by using both the closed-form solution by Johnson (Johnson, 1985), based on the formalisms by Hertz (Hertz, 1896), Cattaneo (Cattaneo, 1938) and Mindlin (Mindlin, 1949), and McEwen (McEwen, 1949), and the closed-form solution by Nowell and Hills (Nowell, 1987). Such an analytical formulation in the case of cylindrical contact has been detailed in Chapter 2;
ii) Subsequently, the critical plane orientation is determined in accordance to the Critical Direction Method proposed by Araújo et al.;
iii) Then, the verification point is determined by means of concepts taken by the theory of the Critical Distance by Taylor;
iv) Finally, the fatigue life is evaluated by means of the Carpinteri et al. criterion for fretting fatigue.

In the following Sections, both the Critical Direction Method by Araújo et al., the theory of the Critical Distance by Taylor and the Carpinteri et al. criterion for fretting fatigue are described, and the advanced methodology proposed in the present Ph.D. Thesis is detailed.

3.2 Critical Direction Method

The Critical Direction Method has been proposed by Araújo et al. (Araújo, 2017) in order to be employed in conjunction with any critical plane-based criterion, for the estimation of the orientation of the crack initiation plane, that is to say, the orientation of the critical plane, in the case of high stress gradient zones.

As is well-known, according to the critical plane-based approach, the critical plane is determined by examining the fatigue load history at a single material point, named critical point. However, in the case of high stress gradient, typical of fretting fatigue configurations, the choice of the critical point is not straightforward due to the variety of stress states in the process zone. Moreover, it would seem more appropriate to analyse suitable quantities summarizing the stress field at the process zone instead of examining the fatigue load history related to a single point. In fact, in such a condition the critical planes related to adjacent material points

may be characterised by different orientations due to the variety of stress state in the process zone.

As a matter of fact, from a mechanical point of view, the crack initiation direction in a high stress gradient zone does not depend on the stress state in a single point only, but it is controlled by an average stress condition within a given material volume (Araújo, 2002).

In such a condition, the critical plane orientation is determined by maximising a suitable quantity computed over a process zone. Such a process zone is represented by a line in two-dimensional problems (or a plane in three-dimensional problems) characterised by a physical dimension. Note that such an association to a physical dimension is not typical of critical plane methods, in which the critical plane determination is limited to define its orientation.

In such a way, the critical plane criteria should be applied as critical direction models.

The implementation of the Critical Direction Method starts by considering a line (with orientation θ) emanating from the crack initiation point H on the material surface (***Figure 3.1***). Analougsly to the philosophy of the theory of the Critical Distance by Taylor (Taylor, 2007) in the form of the Line Method, such a line has a length equal to $2L$.

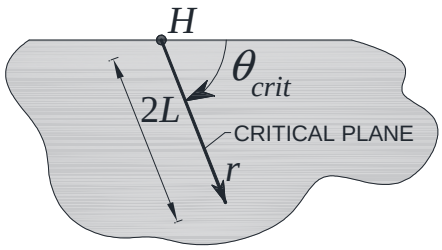

Figure 3.1 *Implementation of the Critical Direction Method proposed by Araújo et al. (Araújo, 2017).*

Subsequently, the fatigue load histories of both normal stress, σ, and shear stress, τ, along such a line are computed by employing either an analytical formulation or a numerical method. Then, both the normal and the shear stresses are averaged along the line, thus obtaining:

$$\bar{\sigma}(\theta,t)=\frac{1}{2L}\int_{0}^{2L}\sigma(r,\theta,t)\,dr \qquad (3.1a)$$

$$\bar{\tau}(\theta,t)=\frac{1}{2L}\int_{0}^{2L}\tau(r,\theta,t)\,dr \qquad (3.1b)$$

Within a loading cycle, the fatigue stress field along the above line is described by means of the maximum and the minimum values of both normal and shear stresses. Therefore, the averaged maximum value, $\bar{\sigma}_{\max}(\theta)$, and amplitude, $\bar{\sigma}_{a}(\theta)$, of the normal stress and the averaged amplitude, $\bar{\tau}_{a}(\theta)$, of the shear stress during a loading cycle are given by:

$$\bar{\sigma}_{\max}(\theta)=\max_{t}\left[\bar{\sigma}(\theta,t)\right] \qquad (3.2a)$$

$$\bar{\sigma}_{a}(\theta)=\frac{1}{2}\left\{\max_{t}\left[\bar{\sigma}(\theta,t)\right]-\min_{t}\left[\bar{\sigma}(\theta,t)\right]\right\} \qquad (3.2b)$$

$$\bar{\tau}_{a}(\theta)=\frac{1}{2}\left\{\max_{t}\left[\bar{\tau}(\theta,t)\right]-\min_{t}\left[\bar{\tau}(\theta,t)\right]\right\} \qquad (3.2c)$$

Finally, by means of the above quantities, the chosen fatigue parameter is computed for the specific orientation, according to the critical plane-based criterion adopted.

Such a procedure is repeated by varying the orientation θ from 0° to 180° (***Figure 3.1***) and, therefore, the critical plane is defined as that corresponding to the orientation θ_{crit} for which the above fatigue parameter is maximized.

3.3 Theory of the Critical Distance

In order to perform the fatigue assessment of a metallic component subject to fretting fatigue, a non-local approach should be employed in conjunction with a multiaxial fatigue criterion. In particular, the use of non-local approaches allows us to take into account the high stress gradient close to the contact surface, thus leading to more accurate estimations in terms of lifetime (Nowell, 1988; Amargier, 2010).

Among the non-local approaches available in the literature, the Theory of the Critical Distance proposed by Taylor (Taylor, 1999; Taylor, 2007) is the most widespread, mainly because of its simplicity. Such a Theory is based on concepts related to the Linear Elastic Fracture Mechanics and Continuum Mechanics, and has been originally proposed to deal with sharp geometries such as notches and cracks, in order to take into account the high stress gradient arising close to the geometric discontinuities. Subsequently, the Theory of the Critical Distance has been successfully applied to fretting fatigue problems (Araújo, 2007; Araújo, 2008; Fouvry, 2014).

According to the Theory of the Critical Distance, the fatigue damage in correspondence of stress raisers is related to an effective linear elastic stress quantity, σ_{eff}, which is assumed to be representative of the damaged zone. Such a damage zone is associated to a material length, named critical distance, L.

The effective stress quantity may be computed in different ways. In particular, for bi-dimensional analyses, three different approaches related to three different domains can be employed:

i) Point Method;
ii) Line Method;
iii) Area Method.

Let us consider an infinite notched plate as is shown in ***Figure 3.2***. The reference system r,θ, with the origin O in correspondence of the apex of the crack, is introduced. The plate is loaded by means of a remote tensile loading, σ. Consequently, the maximum principal stress σ_1 in the vicinity of the notch may be computed by means of the Linear Elastic Fracture Mechanics (***Figure 3.2***).

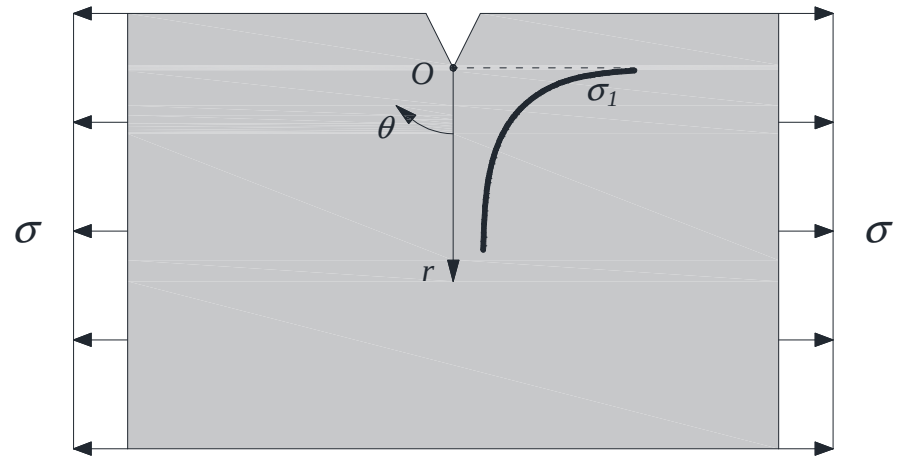

Figure 3.2 *Maximum principal stress profile in a bi-dimensional stress riser.*

As far as the Point Method is concerned, the effective stress quantity is assumed to be equal to the value of the maximum principal stress at a distance equal to $L/2$ from the apex of the notch, that is:

$$\sigma_{eff} = \sigma_1 \left(\theta = 0, r = L/2 \right) \tag{3.3}$$

A similar strategy can be used for fretting configurations, where the equality expressed by *Equation (3.3)* holds in a point located at a distance $L/2$ from the contact edge along a line perpendicular to the contact surface.

As far as the Line Method is concerned, the effective stress quantity is computed by averaging the maximum principal stress up to a distance equal to $2L$ from the apex of the notch, that is:

$$\sigma_{eff} = \frac{1}{2L} \int_0^{2L} \sigma_1 \left(\theta = 0, r \right) dr \tag{3.4}$$

A similar strategy can be used for fretting configurations, where the equality expressed by *Equation (3.4)* holds up to a distance equal to $2L$ from the contact edge along a line perpendicular to the contact surface.

As far as the Area Method is concerned, the effective stress quantity is computed by averaging the maximum principal stress over a semi-circular area, with the centre at the apex of the notch and a radius equal to L, that is:

$$\sigma_{eff} = \frac{4}{\pi L^2} \int_{-\pi/2}^{+\pi/2} \int_{0}^{L} \sigma_1(\theta, r)\, r\, dr\, d\theta \qquad (3.5)$$

A similar strategy can be used for fretting configurations, where the semi-circular area characterised by a radius equal to L is centred at the contact edge.

It is important to highlight that the application of the Theory of the Critical Distance is strongly affected by the definition of the critical distance, L. Such a distance has been defined as an intrinsic material parameter, and may be computed in different ways. The following formulation based on the Fracture Mechanics was proposed by El-Haddad (El-Haddad, 1980):

$$L = \frac{1}{\pi}\left(\frac{\Delta K_{I,th}}{\Delta \sigma_{af,-1}}\right)^2 \qquad (3.6)$$

where $\Delta K_{I,th}$ is the threshold stress intensity factor range for long cracks, and $\Delta \sigma_{af,-1}$ is the fatigue limit range for fully reversed normal loading.

By taking into account the Point Method, Castro et al. (Castro, 2009) showed that the critical distance depends on the multiaxial fatigue criterion considered, and suggested to derive such a distance from the results of two different fatigue tests: one test on a smooth specimen, and another one on a cracked specimen under threshold condition.

Recent works have also correlated the critical distance to the number of loading cycles to failure (Kouanga, 2018; Susmel, 2007).

Moreover, Taylor suggested that the critical distance should be associated with the material microstructure and that it could be taken equal to the average material grain size. Such an assumption is also supported by experimental evidences in which the critical distance is generally found to be of the same scale as the microstructural parameters (Araújo, 2002), and the microcrack path has been observed to be affected by grain boundaries and crystallographic orientations (Araújo, 2017).

3.4 Carpinteri et al. criterion

The Carpinteri et al. criterion (Carpinteri, 2001; Carpinteri, 2011) is a multiaxial fatigue criterion based on the concept of the critical plane. Such a criterion has been originally proposed for metallic structures subject to multiaxial constant amplitude fatigue loading in high-cycle fatigue regime, and it is formulated in terms of stress.

The critical plane-based criteria are based on the experimental observations of both crack nucleation and propagation due to fatigue loading (Marquis, 2003). In particular, three stages may be distinguished in the fatigue fracture process: crack initiation, crack propagation, and final failure (Wulpi, 2013).

The crack initiation stage is characterised by irreversible sub-microscopic changes, named dislocations, caused by cyclic shearing forces. As cyclic loading continues to be applied, such shearing forces produce a dislocation slipping inside the crystal, commonly along a plane oriented at 45° with respect to the loading. Such a plane is named *crack initiation plane*. Moreover, as such dislocations become more pervasive, thus involving different crystals, the coalescence of more microscopic cracks in a macroscopic crack may occur.

Subsequently, during the crack propagation stage, the crack orientation changes from 45° to 90° with respect to the maximum principal stress direction (i.e. direction of the applied loading), and such a crack propagation occurs in a plane named *final fracture plane*. Finally, the failure stage occurs because of the cross-section reduction due to the fatigue crack propagation.

According to such experimental evidences, the Carpinteri et al. criterion allows to take into account both the crack initiation plane (characterised by a Mode II

fracture behaviour) and the final fracture plane (characterised by a Mode I fracture behaviour) in the determination of the critical plane orientation. In particular, such a criterion assumes: (a) as crack initiation plane, a plane whose orientation is linked to that of the final fracture plane through a function that takes into account the fatigue material properties (that is, the fatigue limits under fully reversed normal and shear stress); (b) as final fracture plane, a plane whose orientation is linked to averaged principal stress directions.

According to the critical plane approach, the fatigue assessment of a structural component consists of two steps: Step I deals with the determination of the orientation of the critical plane; Step II deals with the fatigue failure assessment, carried out in such a plane. In more details, the fatigue life is evaluated by employing an equivalent stress amplitude obtained after the reduction of the multiaxial stress state to an equivalent uniaxial one.

3.4.1 Step I: determination of the critical plane orientation

Let us consider a generic point, P, of a metallic structural component and a fixed reference system XYZ with the origin in such a point. The stress tensor $\boldsymbol{\sigma}(t)$ in P at a generic time instant, t, of the fatigue load history ($0 \le t \le T$, where T is the period of the loading cycle) is:

$$\boldsymbol{\sigma}(t) = \begin{bmatrix} \sigma_x(t) & \tau_{xy}(t) & \tau_{xz}(t) \\ \tau_{xy}(t) & \sigma_y(t) & \tau_{yz}(t) \\ \tau_{xz}(t) & \tau_{yz}(t) & \sigma_z(t) \end{bmatrix} \qquad (3.7)$$

In correspondence of such an instant, the principal stresses $\sigma_1(t)$, $\sigma_2(t)$, and $\sigma_3(t)$ (with $\sigma_1(t) \ge \sigma_2(t) \ge \sigma_3(t)$) and the corresponding principal directions 1, 2, and 3 can be computed. Such principal directions are uniquely identified by means of the principal Euler angles $\phi(t)$, $\theta(t)$, and $\psi(t)$ (with $0 \le \phi(t) \le 2\pi$, $0 \le \theta(t) \le \pi$, and $0 \le \psi(t) \le 2\pi$), which represent three subsequent rotations around the Z, Y', and 1 axes, respectively (***Figure 3.3***). Note that the limits

$0 \le \theta(t) \le \pi/2$, and $-\pi/2 \le \psi(t) \le \pi/2$ need to be introduced in order to determine the principal Euler angles (Carpinteri, 1999).

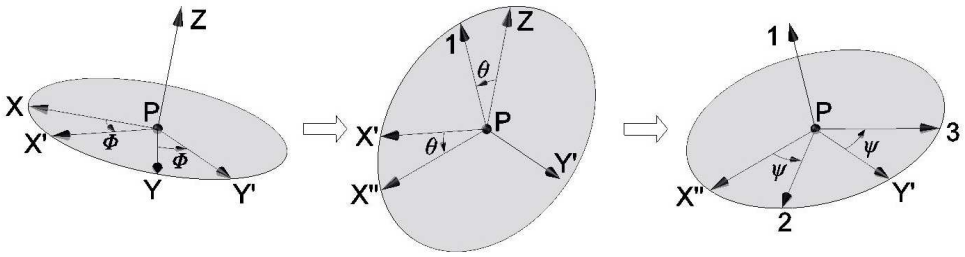

Figure 3.3 *Definition of the principal stress directions* 1, 2, *and* 3 *by means of the principal Euler angles* ϕ, θ, *and* ψ *with respect to the fixed reference system* XYZ.

The principal stresses are generally time-varying under fatigue loading. Therefore, Carpinteri et al. (Carpinteri, 2011) proposed to compute the averaged values of the principal stresses within a loading cycle, identified by $\hat{\sigma}_1$, $\hat{\sigma}_2$, and $\hat{\sigma}_3$. The corresponding averaged principal stress directions $\hat{1}$, $\hat{2}$, and $\hat{3}$ may be identified by means of the averaged principal Euler angles $\hat{\phi}$, $\hat{\theta}$, and $\hat{\psi}$.

In more details, the principal Euler angles are averaged by means of a weight function:

$$W(t) = h\left[\sigma_1(t) - \sigma_{1,\max}\right] \qquad (3.7)$$

where $h\left[\sigma_1(t) - \sigma_{1,\max}\right]$ is the Heaviside step function, which is $h[x] = 1$ if $x \ge 0$ and $h[x] = 0$ if $x < 0$.

In more detail, such a weight function works so that the averaged principal Euler angles and, consequently, the averaged principal stress directions correspond to those at the time instant when the maximum principal stress attains its peak value, $\sigma_{1,\max}$, within a loading cycle. More precisely, the averaged principal Euler angles are given by:

$$\hat{\phi} = \frac{1}{W}\int_0^T \phi(t)\, W(t)\, dt \qquad (3.8a)$$

$$\hat{\theta} = \frac{1}{W}\int_0^T \theta(t)\, W(t)\, dt \qquad (3.8b)$$

$$\hat{\psi} = \frac{1}{W}\int_0^T \psi(t)\, W(t)\, dt \qquad (3.8c)$$

where

$$W = \int_0^T W(t)\, dt \qquad (3.9)$$

According to the Carpinteri et al. criterion (Carpinteri, 2000; Carpinteri, 2002), the normal to the final fracture plane is assumed to coincide with the $\hat{1}$-direction, identified by the mean Euler angles $\hat{\phi}$ and $\hat{\theta}$. Moreover, the normal w to the crack initiation plane is assumed to be linked to the above $\hat{1}$-direction through the off-angle, δ, given by the following empirical expression:

$$\delta = \frac{3}{2}\left[1 - \left(\frac{\tau_{af,-1}}{\sigma_{af,-1}}\right)^2\right] 45° \qquad (3.10)$$

where $\sigma_{af,-1}$ and $\tau_{af,-1}$ are the fatigue limits under fully reversed normal stress and shear stress, respectively, at the reference number N_0 of loading cycles.

Such a rotation δ is generally performed in the $\hat{1}\hat{3}$ plane, from $\hat{1}$ to $\hat{3}$. Note that, as far as bi-dimensional problems are concerned, such a rotation has a physical meaning when it is performed in the plane containing the stress tensor

components, i.e. in the $\hat{1}\hat{3}$ plane when $\hat{\sigma}_2$ is equal to zero, or in the $\hat{1}\hat{2}$ plane when $\hat{\sigma}_3$ is equal to zero.

In accordance to experimental observations (Brown, 1973), the off-angle δ is equal to $0°$ when the ratio between the fatigue limits $\tau_{af,-1}/\sigma_{af,-1}$ is equal to 1 (typical value in the case of hard metals), whereas it is equal to $45°$ when the ratio between the fatigue limits $\tau_{af,-1}/\sigma_{af,-1}$ is equal to $1/\sqrt{3}$ (typical value in the case of borderline mild/hard metals). Therefore, the critical plane tends to coincide with the final fracture plane in hard metals, for which the Mode I is the predominant failure mode, and with the crack initiation plane for mild metals, for which the Mode II is the predominant failure mode. According to the Carpinteri et al. criterion, the critical plane coincides with the dominant failure plane.

3.4.2 Step II: fatigue failure assessment

The second step deals with the computation of the stress components acting on the critical plane at point P of the metallic structural component. In particular, let us consider a local reference system uvw (centred in P), in which $\mathbf{w}$ is the normal to the critical plane, whereas $\mathbf{u}$ is determined by the intersection between the critical plane with the plane containing both the versor $\mathbf{w}$ and the axes Z, and $\mathbf{v}$ is perpendicular to $\mathbf{u}$, both $\mathbf{u}$ and $\mathbf{v}$ laying on the critical plane (***Figure 3.4***).

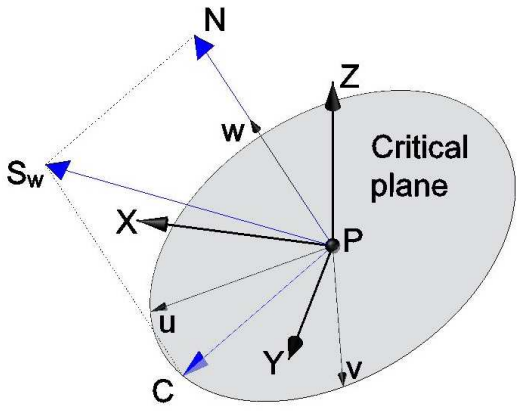

Figure 3.4 *Stress components acting on the critical plane, referred to the local reference system* uvw.

The stress vector at the generic time instant t can be deduced from the stress tensor as follows:

$$\mathbf{S}_{\mathrm{w}}(t)=\boldsymbol{\sigma}(t)\cdot\mathbf{w} \tag{3.11}$$

Then, a normal stress component perpendicular to the critical plane, $\mathbf{N}(t)$, and a shear stress component lying on the critical plane, $\mathbf{C}(t)$, may be computed at the generic time instant t:

$$\mathbf{N}(t)=\left[\mathbf{w}\cdot\mathbf{S}_{w}(t)\right]\mathbf{w} \tag{3.12a}$$

$$\mathbf{C}(t)=\mathbf{S}_{w}(t)-\mathbf{N}(t) \tag{3.12a}$$

In the case of constant amplitude multiaxial cyclic loading, both $\mathbf{N}(t)$ and $\mathbf{C}(t)$ are periodic functions. In more detail, the normal stress component is characterised by a fixed direction with respect to time and, therefore, its modulus is:

$$N(t)=\mathbf{w}\cdot\mathbf{S}_{w}(t)=\mathbf{w}\cdot\boldsymbol{\sigma}(t)\cdot\mathbf{w} \tag{3.13}$$

Moreover, both the mean value N_m and the amplitude N_a are easily evaluated:

$$N_{m}=\frac{1}{2}\left\{\max_{0\le t<T}\left[\mathbf{w}\cdot\boldsymbol{\sigma}(t)\cdot\mathbf{w}\right]+\min_{0\le t<T}\left[\mathbf{w}\cdot\boldsymbol{\sigma}(t)\cdot\mathbf{w}\right]\right\} \tag{3.14a}$$

$$N_{a}=\frac{1}{2}\left\{\max_{0\le t<T}\left[\mathbf{w}\cdot\boldsymbol{\sigma}(t)\cdot\mathbf{w}\right]-\min_{0\le t<T}\left[\mathbf{w}\cdot\boldsymbol{\sigma}(t)\cdot\mathbf{w}\right]\right\} \tag{3.14b}$$

On the other hand, the shear stress component lying on the critical plane has a time-varying direction. In particular, during the fatigue load history, the vector $\mathbf{C}(t)$ describes a closed path, Σ, on the critical plane. A closed-form equation of Σ is available for simple load history only. As far as a more complex load history is concerned, a polygonal path, Σ', consisting of n vertexes may be used as an approximation of the real path, so that $\lim_{n\to\infty}\Sigma' = \Sigma$ (Carpinteri, 2014).

Different methods available in the literature (Susmel, 2009) may be used in order to determine the shear stress component. Among them, the Longest Chord method (Lemaitre, 1990), the Longest Projection method (Grubisic, 1976), and the Minimum Bounding Circle method (Papadopoulos, 1998) are worth noting. Nevertheless, such methods are not able to uniquely compute the shear stress components in some cases. Moreover, they lead to high computational costs when complex load histories are investigated.

The shear stress component may be uniquely computed by means of the Maximum Rectangular Hull method, recently proposed by Araújo et al. (Mamiya, 2002; Mamiya, 2009; Araújo, 2011). Such a method, implemented in the Carpinteri et al. criterion (Carpinteri, 2013; Carpinteri, 2014), works by bordering the closed path Σ by means of different rectangles, each of which is characterised by an orientation, Θ, with respect to the reference system uvw, as is shown in ***Figure 3.5***.

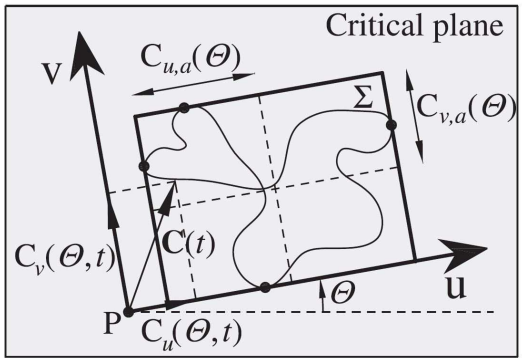

Figure 3.5 *Closed path Σ of the shear stress component bordered by means of a generic rectangle, according to the Maximum Rectangular Hull method (Carpinteri, 2013).*

The components C_u and C_v of the shear stress vector along **u** and **v** directions, respectively, can be computed through the Maximum Rectangular Hull method. Moreover, the amplitudes of such components correspond to the half sides of the rectangle and, consequently, are determined as follows:

$$C_{u,a}(\Theta)=\frac{1}{2}\left\{\max_{0\le t<T}\left[C_u(t,\Theta)\right]-\min_{0\le t<T}\left[C_u(t,\Theta)\right]\right\} \tag{3.15a}$$

$$C_{v,a}(\Theta)=\frac{1}{2}\left\{\max_{0\le t<T}\left[C_v(t,\Theta)\right]-\min_{0\le t<T}\left[C_v(t,\Theta)\right]\right\} \tag{3.15b}$$

Then, the amplitude C_a of the shear stress component is given by:

$$C_a=\max_{0^\circ\le\Theta<90^\circ}\sqrt{\left[C_{u,a}(\Theta)\right]^2+\left[C_{v,a}(\Theta)\right]^2} \tag{3.16}$$

The fatigue failure assessment is carried out referring to the critical plane, by comparing the following equivalent uniaxial stress amplitude, $\sigma_{eq,a}$, with the fatigue limit under fully reversed normal stress:

$$\sigma_{eq,a}=\sqrt{N_{eq,a}^2+\left(\frac{\tau_{af,-1}}{\sigma_{af,-1}}\right)^2 C_a^2}=\sigma_{af,-1} \tag{3.17}$$

being

$$N_{eq,a}=N_a+\sigma_{af,-1}\left(\frac{N_m}{\sigma_u}\right) \tag{3.18}$$

where σ_u is the material ultimate tensile strength. Note that, in the case the value of σ_u is not available, the yield stress might be used instead of the ultimate tensile strength, especially in the case of mild metals.

Equation (3.18) considers the linear relationship between N_a and N_m proposed by Goodman (Goodman, 1899), which allows us to take into account the strength decrease due to the simultaneous presence of a tensile mean normal stress and an alternating normal stress. Therefore, N_m should be conservatively assumed to be equal to zero in the case of a compressive mean normal stress.

Nevertheless, according to Stephens et al. (Stephens, 2000) the Goodman expression can be extrapolated for negative mean stress, if the stress level is beneath the yielding stress value of the material. Therefore, in order to take into account the beneficial effect produced by the compressive residual stress field on fatigue life, N_m is considered in the computation of $N_{eq,a}$ even in the case of negative value of mean normal stress.

For the finite fatigue life evaluation, the finite life fatigue strengths, $\sigma'_{af,-1}$ and $\tau'_{af,-1}$, proposed by Basquin (Basquin, 1910) are employed, instead of the fatigue limits under fully reversed normal and shear loading, respectively:

$$\sigma'_{af,-1} = \sigma_{af,-1}\left(\frac{N_f}{N_0}\right)^m \qquad (3.19a)$$

$$\tau'_{af,-1} = \tau_{af,-1}\left(\frac{N_f}{N_0}\right)^{m^*} \qquad (3.19b)$$

where N_0 is the reference number of loading cycles (generally $N_0 = 2 \cdot 10^6$) for the material fatigue limits under fully reversed normal and shear loading, $\sigma_{af,-1}$ and $\tau_{af,-1}$, respectively, whereas m and m^* are the slopes of the S-N curve under fully reversed normal and shear loading, respectively.

Finally, fatigue life is evaluated by means of an iterative procedure. More precisely, the number of loading cycles to failure, $N_{f,cal}$, is computed by solving the following expression obtained by replacing *Equation (3.18)* and *Equations (3.19)* into *Equation (3.17)*:

$$\sqrt{\left[N_a+\sigma_{af,-1}\left(\frac{N_m}{\sigma_u}\right)\right]^2+\left(\frac{\sigma_{af,-1}}{\tau_{af,-1}}\right)^2\left(\frac{N_{f,cal}}{N_0}\right)^{2m}\left(\frac{N_0}{N_{f,cal}}\right)^{2m^*}C_a^2}=\sigma_{af,-1}\left(\frac{N_{f,cal}}{N_0}\right)^m \quad (3.20)$$

3.5 Advanced methodology: description

The present Section deals with the description of the methodology proposed in the present PhD Thesis for fretting fatigue assessment. Such a methodology allows us to determine both the crack initiation direction and the fatigue life of a metallic structural component subject to fretting fatigue.

The flowchart of such a methodology is shown in ***Figure 3.6***, whereas the main steps are hereafter summarised.

Let us consider the typical fretting fatigue configuration already shown in ***Figure 2.3*** (see Section 2.4 of the present PhD Thesis), where two fretting pads, which may be characterised by either spherical or cylindrical shape, are pushed against a dog-bone specimen in partial slip regime. A normal constant force, P, and a cyclic tangential force, $Q(t)$, are applied to the pads, whereas the specimen experiences a cyclic axial bulk stress, $\sigma_B(t)$, which is in-phase with $Q(t)$.

Three categories of input data need to be set in order to employ the methodology proposed in the present PhD Thesis. Such input data are related to geometrical sizes, material properties, and loading conditions.

Related to the first category, the sizes of both pads and specimen are needed: radius of the pads, R, and thickness and width of the specimen.

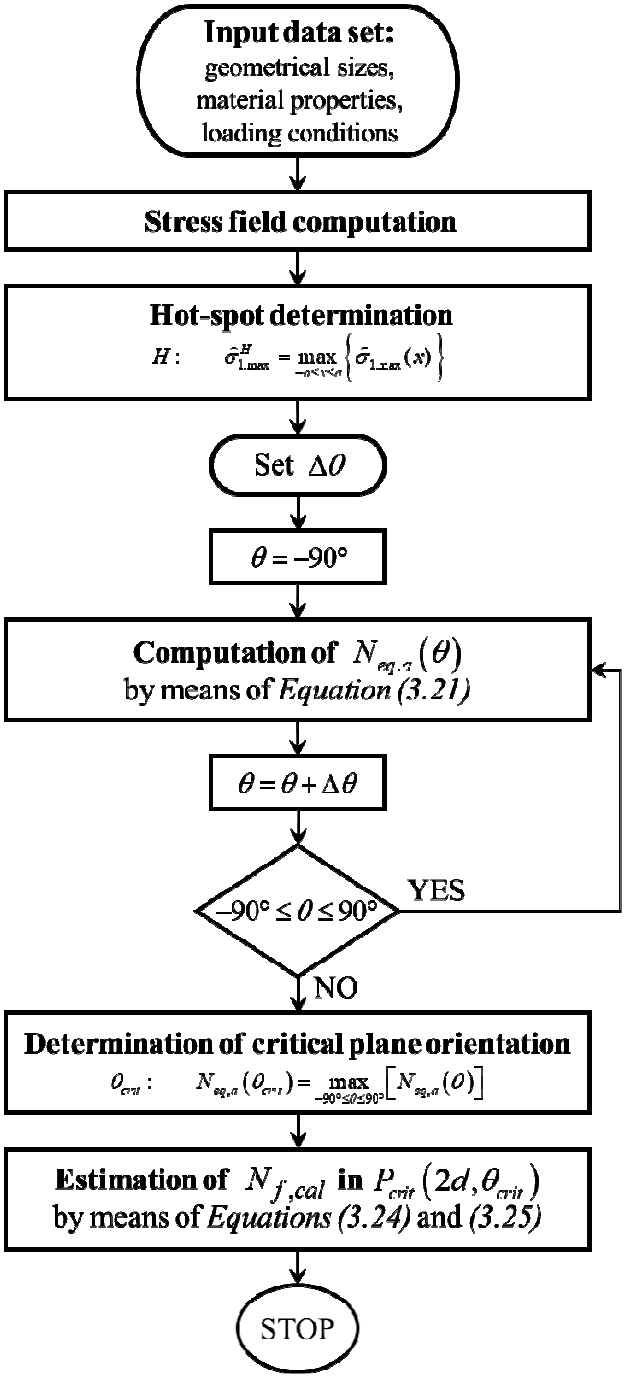

Figure 3.6 *Flowchart of the methodology proposed in the present PhD Thesis for the*

fretting fatigue assessment of metallic structural components.

The parameters belonging to the second category are the mechanical and fatigue properties and the average grain size of the material. In more detail, the elastic modulus E, the Poisson coefficient ν, the coefficient of friction μ, the ultimate tensile strength σ_u, the fatigue limits under fully reversed normal and shear stress, $\sigma_{af,-1}$ and $\tau_{af,-1}$, respectively, the slopes m and m^* of the S-N curves under fully reversed normal and shear stress, respectively, and the average grain size d.

Moreover, the loading conditions to be set are the normal constant load P, the amplitude Q_a of the cyclic tangential load, and both amplitude $\sigma_{B,a}$ and mean stress $\sigma_{B,m}$ of the cyclic bulk stress applied to the specimen.

Firstly, the stress field in the vicinity of the contact zone is computed as is described in Section 2.4, by means of the closed-form solutions proposed by Johnson (Johnson, 1985) and by Nowell and Hills (Nowell, 1987) for the case of fretting fatigue elastic partial slip loading condition. Note that such an analytical formulation has been implemented within the methodology proposed in the present PhD Thesis, since such a methodology has been verified by taking into account experimental fretting fatigue tests in partial slip conditions.

Once the stress field is evaluated, the hot-spot H is looked for on the contact surface, that is, $-a \le x \le a$, where a is the semi-width of the contact area (***Figure 3.7***). The hot-spot is assumed to be the point where the maximum value of the average maximum principal stress is attained. Note that H is generally found to be at the contact trailing edge, that is, $x = a$.

Subsequently, the critical plane orientation is computed by exploiting the Critical Direction Method proposed by Araújo et al. (Araújo, 2017) described in Section 3.2. According to the Critical Direction Method, material planes having length equal to twice the critical distance, that is, $2L$, starting from the hot-spot, H, and characterised by different orientations are examined. Subsequently, a suitable fatigue parameter is computed for each of the aforementioned material planes. According to the methodology proposed in the present PhD Thesis, the equivalent stress amplitude, $N_{eq,a}$, defined according to the Carpinteri et al. criterion (Carpinteri, 2001; Carpinteri, 2011), is taken as such a parameter.

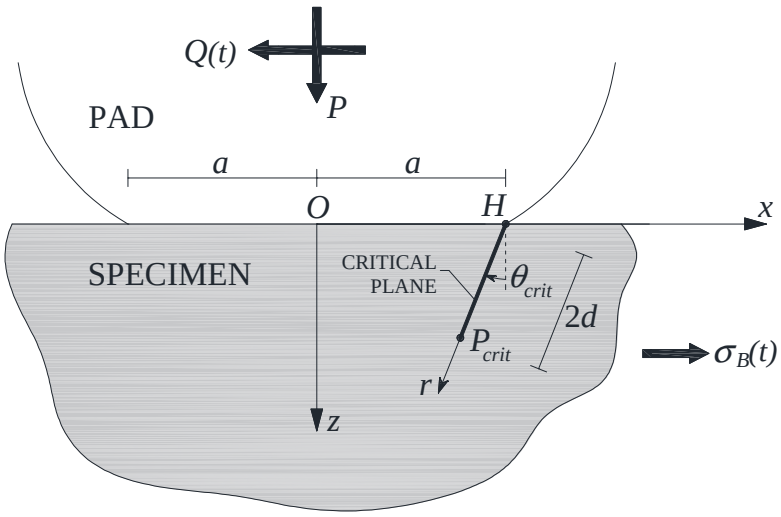

Figure 3.7 *Hot-spot, H, critical plane and verification point, P_{crit}, according to the methodology proposed in the present PhD Thesis for the fretting fatigue assessment of metallic structural components.*

The critical distance L is assumed to be equal to the average material grain size, d, in order to relate such a length to the material microstructure.

Moreover, the orientation of each material plane is identified by means of the angle θ ($-90° \le \theta \le 90°$), defined as a clock-wise angle starting from the line perpendicular to the contact surface (***Figure 3.7***). Therefore, as far as the hot-spot is located at the contact trailing edge, the angle θ assumes either positive or negative values for material planes inside or outside the contact zone, respectively.

A suitable value of the angular increment, $\Delta\theta$, needs to be set (for instance, $\Delta\theta = 1°$ may be assumed). The procedure starts by analysing the material plane corresponding to the initial value $\theta = -90°$. The equivalent stress amplitude, $N_{eq,a}(\theta)$, acting on the corresponding material plane and related to a segment with length equal to $2d$, is evaluated by means of the Carpinteri et al. criterion:

$$N_{eq,a}(\theta) = \bar{N}_a(\theta) + \sigma_{af,-1}\left(\frac{\bar{N}_m(\theta)}{\sigma_u}\right) \qquad (3.21)$$

where $\bar{N}_a(\theta)$ and $\bar{N}_m(\theta)$ are the amplitude and the mean value of the normal stress component perpendicular to the material plane, averaged along the above material plane up to a length equal to $2d$:

$$\bar{N}_a(\theta) = \frac{1}{2d}\int_0^{2d} N_a(r,\theta)\, dr \qquad (3.22a)$$

$$\bar{N}_m(\theta) = \frac{1}{2d}\int_0^{2d} N_m(r,\theta)\, dr \qquad (3.22b)$$

Note that the values of both $N_a(r,\theta)$ and $N_m(r,\theta)$ are computed by considering the critical plane orientation as fixed (equal to θ). This means that the procedure described in Section 3.4.1 for determining the critical plane orientation through the off-angle δ is not employed in the proposed methodology.

Then, a new material plane is taken into account by updating the value of the angle, $\theta = \theta + \Delta\theta$. Such a procedure is iterated for all the material planes belonging to the specimen half-space, that means until θ is equal to $90°$.

The material plane orientation, θ_{crit}, that produces the maximum value of the equivalent stress amplitude is referred to as the critical plane and, accordingly, as the crack initiation plane:

$$N_{eq,a}(\theta_{crit}) = \max_{-90°\le\theta\le 90°}\left[N_{eq,a}(\theta)\right] \qquad (3.23)$$

Then, in accordance to the philosophy of the Theory of the Critical Distance proposed by Taylor (Taylor, 1999; Taylor, 2007) in order to take into account the high stress gradient close to the contact surface, the fretting fatigue assessment is performed in a certain point away from the hot-spot. In more detail, the position of the critical point, P_{crit}, where to perform the fretting fatigue assessment is assumed

to be located at the end of the segment starting from H, with length equal to $2d$ and direction defined by the angle θ_{crit} (***Figure 3.7***).

Note that, according to the methodology proposed in the present PhD Thesis, the length of the above segment is related to the average material grain size, d. Such an assumption is supported by both the assumptions of the Theory of the Critical Distance by Taylor and experimental evidences, as has already been discussed in Section 3.3.

Finally, the fatigue life $N_{f,cal}$ is estimated through *Equation (3.20)*, by employing the values of the stress components acting on the critical plane at the critical point: $N_a\left(2d,\theta_{crit}\right)$, $N_m\left(2d,\theta_{crit}\right)$, and $C_a\left(2d,\theta_{crit}\right)$ (note that such values are computed by considering the critical plane orientation to be equal to θ_{crit}, that is, the procedure in Section 3.4.1 to determine the critical plane orientation through the off-angle δ is not applied):

$$\sqrt{\left[N_{eq,a}\left(2d,\theta_{crit}\right)\right]^2+\left(\frac{\sigma_{af,-1}}{\tau_{af,-1}}\right)^2\left(\frac{N_{f,cal}}{N_0}\right)^{2m}\left(\frac{N_0}{N_{f,cal}}\right)^{2m^*}\left[C_a\left(2d,\theta_{crit}\right)\right]^2}= \\ =\sigma_{af,-1}\left(\frac{N_{f,cal}}{N_0}\right)^m \qquad (3.24)$$

where

$$N_{eq,a}\left(2d,\theta_{crit}\right)=N_a\left(2d,\theta_{crit}\right)+\sigma_{af,-1}\left(\frac{N_m\left(2d,\theta_{crit}\right)}{\sigma_u}\right) \qquad (3.25)$$

Therefore, the methodology proposed in the present PhD Thesis for the fretting fatigue assessment of metallic structural components allows us:

i) to estimate the crack initiation direction (assumed coincident with the orientation of the critical plane) by means of *Equation (3.23)*;

ii) to estimate the number of loading cycles to failure by means of *Equation (3.24)*.

3.6 References

Amargier R., Fouvry S., Chambon L., Schwob C., Poupon C. Stress gradient effect on crack initiation in fretting using a multiaxial fatigue framework. *International Journal of Fatigue*, 2010; 32: 1904-1912.

Araújo J.A., Nowell D. The effect of rapidly varying contact stress fields on fretting fatigue. *International Journal of Fatigue*, 2002; 24: 763-775.

Araújo J.A., Susmel L., Taylor D., Ferro J.C.T., Mamiya E.M. On the use of the theory of critical distances and the modified wöhler curve method to estimate fretting fatigue strength of cylindrical contacts. *International Journal of Fatigue*, 2007; 29: 95-107.

Araújo J.A., Susmel L., Taylor D., Ferro J.C.T., Ferreira J.L.A. On the prediction of high-cycle fretting fatigue strength: theory of critical distances vs. hot-spot approach. *Engineering Fracture Mechanics*, 2008; 75: 1763–78.

Araújo J.A., Dantas A.P., Castro F.C., Mamiya E.N., Ferreira J.L.A. On the characterization of the critical plane with a simple and fast alternative measure of the shear stress amplitude in multiaxial fatigue. *International Journal of Fatigue*, 2011; 33: 1092-1100.

Araújo J.A., Almeida G.M.J., Ferreira J.L.A., da Silva C.R.M., Castro F.C. Early cracking orientation under high stress gradients: The fretting case. *International Journal of Fatigue*, 2017; 100: 611-618.

Basquin O.H. The exponential law of endurance tests. *Proceedings of the American Society for Testing and Materials*, 1910; 10: 625-630.

Carpinteri A., Macha E., Brighenti R., Spagnoli A. Expected principal stress directions under multiaxial random loading – Part I (Theoretical aspects of the weight function method) e Part II (Numerical simulation and experimental assessment through the weight function method). *International Journal of Fatigue*, 1999; 21: 83-96.

Carpinteri A., Brighenti R., Spagnoli A. A fracture plane approach in multiaxial high-cycle fatigue of metals. *Fatigue and Fracture of Engineering Materials and Structures*, 2000; 23: 355-364.

Carpinteri A., Spagnoli A. Multiaxial high-cycle fatigue criterion for hard metals. *International Journal of Fatigue*, 2001; 23: 135-145.

Carpinteri A., Karolczuk A., Macha E., Vantadori S. Expected position of the fatigue fracture plane by using the weighted mean principal Euler angles. *International Journal of Fracture*, 2002; 115: 87-99.

Carpinteri A., Spagnoli A., Vantadori S. Multiaxial fatigue assessment using a simplified critical plane-based criterion. *International Journal of Fatigue*, 2011; 33: 969-976.

Carpinteri A., Ronchei C., Spagnoli A., Vantadori S., Araújo J.A. MRH method and modified C-S (Carpinteri-Spagnoli) criterion. *In: Atti del XXI Congresso dell'Associazione Italiana di Meccanica Teorica e Applicata*, Torino; 2013.

Carpinteri A., Ronchei C., Spagnoli A., Vantadori S. On the use of the Prismatic Hull method in a critical plane-based multiaxial fatigue criterion. *International Journal of Fatigue*, 2014; 68: 159-167.

Carpinteri A., Ronchei C., Scorza D., Vantadori S. Critical plane orientation influence on multiaxial high-cycle fatigue assessment. *Physical Mesomechanics*, 2015; 18: 348-354.

Carpinteri A., Vantadori S., Zanichelli A. Lifetime estimation of mechanical assemblies under constant amplitude fretting fatigue loading. *Fatigue and Fracture of Engineering Materials and Structures*, 2019; 42: 1927-1936.

Castro F.C., Araújo J.A., Zouain N. On the application of multiaxial high-cycle fatiguecriteria using the theory of critical distances. *Engineering Fracture Mechanics*, 2009; 76: 512-524.

Cattaneo C. Sul contatto di due corpi elastici: distribuzione locale degli sforzi. *Rendiconti dell'Accademia Nazionale dei Lincei*, 1938; 27, 6: 342–8.

El-Haddad M.H., Dowling N.F., Topper T.H., Smith K.N. J Integral applications for short fatigue cracks at notches. *International Journal of Fracture*, 1980; 16: 15-24.

Fouvry S., Gallien H., Berthel B. From uni-to-multi-axial fretting-fatigue crack nucleation: development of a stress-gradient-dependent critical distance approach. *International Journal of Fatigue*, 2014; 62: 194-209.

Goodman J. *Mechanics Applied to Engineering*. Longmans Green, London; 1899.

Grubisic V., Simbürger A. Fatigue under combined out of phase multiaxial stresses. *In: Proceedings of International Conference on Fatigue Testing and Design*, Society of Environmental Engineers, London, 27.1-27.8; 1976.

Hertz H. *Miscellaneous Paper by Heinrich Hertz*. New York: Macmillan & Co; 1896.

Johnson K.L. *Contact Mechanics*. UK: Cambridge University Press; 1985.

Kouanga C.T., Jones J.D., Revill I., Wormald A., Nowell D., Dwyer-Joyce R.S., et al. On the estimation of finite lifetime under fretting fatigue loading. *International Journal of Fatigue*, 2018; 112: 138-152.

Lemaitre J., Chaboche J.L. *Mechanics of Solid Materials*. Cambridge University Press, Cambridge; 1990.

Mamiya E.N., Araújo J.A. Fatigue limit under multiaxial loadings: on the definition of the equivalent shear stress. *Mechanics Research Communications*, 2002; 29: 141-151.

Mamiya E.N., Araújo J.A., Castro F.C. Prismatic hull: a new measure of shear stress amplitude in multiaxial high cycle fatigue. *International Journal of Fatigue*, 2009; 31: 1144-1153.

Marquis G.B., Karjalainen-Roikonen P. Long-life multiaxial fatigue of a nodular graphite cast iron. *In: Biaxial/Multiaxial Fatigue and Fracture, a cura di A. Carpinteri, M. de Freitas e A. Spagnoli*. Amsterdam: Elsevier; 383-400; 2003.

McEwen E. Stress in elastic cylinders in contact along a generatrix. *Philosophical Magazine*, 1949; 40: 454.

Mindlin R.D. Compliance of elastic bodies in contact. *ASME Journal of Applied Mechanics*, 1949; 16: 259–68.

Nowell D., Hills D. Mechanics of fretting fatigue tests. *International Journal of Mechanical Sciences*, 1987; 29, 5: 355–65.

Nowell D. *An analysis of fretting fatigue*. Ph.D. thesis, Oxford University; 1988.

Papadopoulos I.V. Critical plane approaches in high-cycle fatigue: on the definition of the amplitude and mean value of the shear stress acting on the critical plane. *Fatigue and Fracture of Engineering Materials and Structures*, 1998; 21: 269-285.

Ronchei C., Carpinteri A., Fortese G., Scorza D., Vantadori S. Fretting high-cycle fatigue assessment through a multiaxial critical plane-based criterion in conjunction with the Taylor's point method. *Solid State Phenomena*, 2016; 258: 217-220.

Stephens R.I., Fatemi A., Stephens R.R., Fuchs H.O. *Metal Fatigue in Engineering*. Second edition, John Wiley & Sons; 2000.

Susmel L., Taylor D. A novel formulation of the theory of critical distances to estimate lifetime of notched components in the medium-cycle fatigue regime. *Fatigue and Fracture of Engineering Materials and Structures*, 2007; 30: 567-581.

Susmel L. *Multiaxial Notch Fatigue: from nominal to local stress-strain quantities*. Woodhead & CRC, Cambridge; 2009.

Taylor D. Geometrical effects in fatigue: a unifying theoretical model. *International Journal of Fatigue*, 1999; 21: 413-420.

Taylor D. *The Theory of Critical Distances: A New Perspective in Fracture Mechanics*. UK: Elsevier; 2007.

Vantadori S., Vázquez J., Zanichelli A. Fretting fatigue and shot peening: a multiaxial fatigue criterion including residual stress relaxation. *Tribology International*, 2020a; 151, 106537.

Vantadori S., Zanichelli A. Fretting-fatigue analysis of shot-peened aluminium and titanium test specimens. *Fatigue and Fracture of Engineering Materials and Structures*, 2020b; In press.

Vantadori S., Zanichelli A., Araújo J.A. Fretting fatigue of 7050-T7451 Al alloy: the influence of bulk mean stress. *International Journal of Fatigue*, 2020c; 140, 105816.

Wulpi Donald J. *Understanding how components fail*. 3rd ed. Ohio: Edited by Brett Miller. ASM International; 2013.

Zanichelli A., Vantadori S. Shot-peened fretting fatigue components: endurance strength and fatigue life assessment. *Material Design & Processing Communications*, 2020; doi: 10.1002/mdp2.196.

4

VALIDATION OF THE ADVANCED METHODOLOGY PROPOSED FOR FRETTING FATIGUE ASSESSMENT

4.1 Introduction

The present Chapter deals with the validation of the analytical methodology proposed in the present Ph.D. Thesis for fretting fatigue assessment of structural components. In particular, the multiaxial fatigue criterion proposed by Carpinteri et al. (Carpinteri, 2011) and the Critical Direction method proposed by Araújo et al. (Araújo, 2017) are implemented in such a methodology (that is described in Chapter 3), and the philosophy related to the theory of the Critical Distance by Taylor (Taylor, 2007) is also taken into account.

The fretting behaviour of metallic components under fretting fatigue elastic partial slip loading conditions is assessed.

Experimental campaigns available in the literature characterised by either cylindrical or spherical contact configurations are examined. In more detail, the fretting fatigue tests analysed involve the application of the fretting loads by means of two pads, characterised by either cylindrical or spherical profile, which are clamped to a flat specimen.

Experimental tests carried out under either fretting fatigue or fretting wear loading conditions are taken into account. More precisely, as far as fretting fatigue loading conditions are concerned, a constant normal load and a cyclic tangential load are applied to the pads. On the other hand, as far as fretting wear loading conditions are concerned, a constant normal load and a cyclic tangential displacement are applied to the pads.

The stress field within the specimens is determined by means of the closed-form solution by Johnson (Johnson, 1985), based on the formalisms by Hertz (Hertz, 1896), Cattaneo (Cattaneo, 1938) and Mindlin (Mindlin, 1949), and McEwen (McEwen, 1949), together with the closed-form solution by Nowell and Hills

(Nowell, 1987). Such an analytical formulation in the case of cylindrical contact is detailed in Section 2.4 of the present Ph.D. Thesis.

The accuracy of the proposed methodology is verified by taking into account eight different materials: four aluminium alloys, one titanium alloy, and three steels.

It can be highlighted that, in some cases, shot-peened specimens have been tested. In particular, such specimens have been treated before the fretting test, in order to investigate the influence of such a surface treatment on the fretting behaviour of the structural component.

Shot peening is a cold process consisting in hitting the surface to be treated with a jet of well-defined shots. The main beneficial effect of shots impact is represented by a compressive residual stress field, limited to a material surface layer of the order of 0.1÷0.5 mm (Vantadori, 2020). Nevertheless, it should be highlighted that the superficial compressive stress state is not stable, but it may evolve. Such a phenomenon, known as residual stress relaxation (Schulze, 2006; Wagner, 2003), is considered as one of the main drawbacks of shot peening.

Residual stresses may be experimentally measured by means of the X-Ray Diffraction method or the Blind Hole Drilling method, the latter being a destructive test. It can be remarked that shot peening produces residual stresses along both longitudinal and transversal specimen directions, and the values of such stresses are comparable to each other, whereas the values of all the other stress components are negligible (Araujo, 2009).

The stress state within a shot-peened specimen may be computed by taking into account both the relaxed residual stress field and the stress produced by fretting fatigue loading. Such two contributions may be independently evaluated and then combined according to the superposition principle, since residual stresses affect the stress field acting on the mean value of longitudinal and transversal components of the stress tensor.

In Sections from 4.2 to 4.9, the theoretical results obtained in terms of both crack path orientation and fatigue life are described and compared to the experimental ones available in the literature. Moreover, the accuracy of the criterion in terms of fatigue life estimations is quantified by means of the root mean square error method. Such an error, T_{RMS}, is computed as follows:

$$T_{RMS} = 10^{E_{RMS}} \tag{4.1}$$

being

$$E_{RMS} = \sqrt{\frac{\sum_{i=1}^{n} \log^2 \left(N_{exp} / N_{cal,R} \right)_i}{n_s}} \tag{4.2}$$

where n_s is the total number of specimens of the considered series. Note that $T_{RMS} = 1$ represents a perfect correlation between experimental and estimated values.

4.2 Al 2024-T351 aluminium alloy

The experimental campaign carried out by Szolwinski and Farris (Szolwinski, 1998) has been analysed through the proposed methodology. Such an experimental campaign is detailed in Section 4.2.1, whereas the results obtained by employing the proposed methodology are discussed in Section 4.2.2.

4.2.1 Experimental campaign

Thirty-seven flat dog-bone test specimens (named specimens from T1 to T37 in the following) made of Al 2024-T351 alloy were tested. The mechanical and fatigue properties are listed in ***Table 4.1*** (Szolwinski, 1998).

Table 4.1 Mechanical and fatigue properties of Al 2024-T351 alloy (Szolwinski, 1998).

MATERIAL	E [GPa]	ν	σ_u [MPa]	$\sigma_{af,-1}$ [MPa]	m	$\tau_{af,-1}$ [MPa]	m^*	N_0 [cycles]
Al 2024-T351	74	0.33	465	218	-0.08	126	-0.08	$2 \cdot 10^6$

The averaged grain size d is equal to $40\,\mu m$ (Li, 2019), whereas the coefficient of friction μ within the contact zone is equal to 0.65 (Szolwinski, 1998).

The experimental tests were carried out in partial slip regime by using two cylindrical pads (made of the same material of the specimens). Note that three different values of the pad radius were used, that is, R equal to 127 mm, 178 mm, and 229 mm, respetively. A constant normal load P and a cyclic tangential load $Q(t)$ (characterised by a loading ratio $R=-1$) were applied to the pads. Moreover, the specimen experienced a cyclic bulk stress $\sigma_B(t)$ (characterised by a loading ratio $R=-1$), which was in-phase with $Q(t)$.

The pad radius, the loading parameters (normal load P, amplitude Q_a of the cyclic tangential load, and amplitude $\sigma_{B,a}$ of the cyclic bulk stress) and the corresponding experimental fretting fatigue life, $N_{f,exp}$, are listed in ***Table 4.2*** for each specimen tested.

Table 4.2 Pad radius R, loading parameters (normal load P, amplitude Q_a of the cyclic tangential load, amplitude $\sigma_{B,a}$ of the cyclic bulk stress), estimated crack path orientation θ_{cal}, experimental and estimated fretting fatigue life ($N_{f,exp}$ and $N_{f,cal}$, respectively), for specimens No. T1-T36.

TEST No.	R [mm]	P [N/mm]	Q_a [N/mm]	$\sigma_{B,a}$ [MPa]	θ_{cal} [°]	$N_{f,exp}$ [cycles]	$N_{f,cal}$ [cycles]	$\frac{N_{f,exp}}{N_{f,cal}}$
T1	121	384	134	101	4	241016	314611	0.77
T2	121	497	154	110	4	217061	236445	0.92
T3	127	385	108	85	5	422000	1316663	0.32
T4	127	410	213	116	4	465000	106999	4.35
T5	127	423	148	88	5	563946	553733	1.02
T6	127	427	132	110	4	241475	339815	0.71
T7	127	430	142	97	4	311516	450683	0.69
T8	127	489	171	109	4	302804	205269	1.48
T9	127	490	113	85	5	668277	1188410	0.56
T10	127	494	178	98	4	464166	260476	1.78

T11	127	557	150	109	4	253883	269926	0.94
T12	127	560	151	85	5	381535	590168	0.65
T13	127	569	176	102	5	545489	240020	2.27
T14	127	569	176	102	5	337934	240020	1.41
T15	127	595	131	110	5	314000	336676	0.93
T16	178	418	159	86	4	582922	745793	0.78
T17	178	419	151	97	4	459882	558239	0.82
T18	178	421	160	111	4	330695	326479	1.01
T19	178	486	131	85	4	621442	1140104	0.55
T20	178	493	133	100	4	433780	624223	0.69
T21	178	494	133	100	4	349520	623309	0.56
T22	178	509	173	106	4	225535	311753	0.72
T23	178	551	187	113	4	455759	216657	2.10
T24	178	558	117	85	4	665073	1360706	0.49
T25	178	558	117	85	4	749093	1360706	0.55
T26	178	571	177	99	4	552250	365069	1.51
T27	229	417	129	81	4	867330	1792186	0.48
T28	229	419	109	83	4	768364	2230689	0.34
T29	229	427	158	113	3	249574	397615	0.63
T30	229	429	185	112	3	238000	319864	0.74
T31	229	487	161	111	3	479540	399302	1.20
T32	229	490	157	97	4	739250	665561	1.11
T33	229	494	158	85	4	856524	1000289	0.86
T34	229	551	187	110	3	320864	313487	1.02
T35	229	557	134	82	4	747135	1536121	0.49
T36	229	557	139	82	4	729715	1425722	0.51
T37	229	563	135	98	4	463324	791507	0.59

4.2.2 Results

The experimental campaign described in Section 4.2.1 has been analysed by means of the analytical methodology proposed in the present Ph.D. Thesis for fretting fatigue assessment of structural components.

As far as the crack path orientation is concerned, the angles θ_{cal} estimated by means of the proposed methodology range from 3° to 5°, depending on the fretting loading conditions (***Table 4.2***). More precisely, the theoretical crack nucleates at

the contact trailing edge, and is characterized by a direction inward the contact region.

No data in terms of experimental crack path are available for the tests examined. However, an additional specimen subjected to fretting loading conditions equal to those used in test No. T22 was tested in order to experimentally analyse the crack initiation path. The experimental crack orientation of such an additional test is compared to the corresponding analytical one in ***Figure 4.1***. It can be observed that the experimental crack nucleated at the contact trailing edge and grew inward the contact region, in accordance with the theoretical estimations. However, further comparisons with the theoretical results are quite difficult since, in accordance to the proposed methodology, the critical plane orientation is estimated by taking into account a process zone characterised by a size equal to twice the averaged grain size.

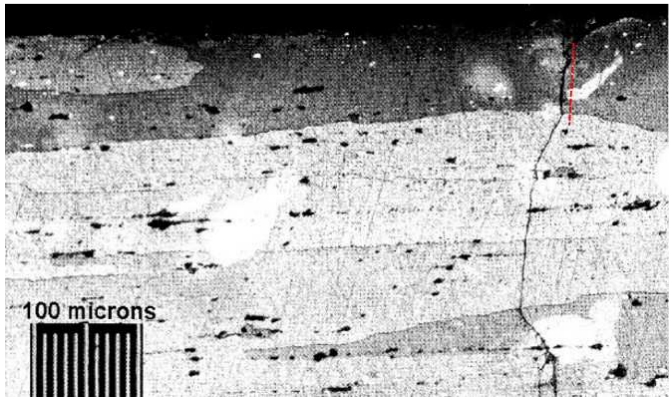

Figure 4.1 *Experimental crack path (Szolwinski, 1998) and theoretical crack orientation (dashed-red line) for fretting fatigue configuration of test No. T22.*

As far as fatigue life is concerned, the number $N_{f,cal}$ of loading cycles to failure estimated by means of the proposed methodology is listed in ***Table 4.2*** for each specimen, together with the ratio $N_{f,exp}/N_{f,cal}$. Moreover, a comparison between experimental and estimated fatigue life is shown in ***Figure 4.2*** for each test analysed. Note that the dashed lines correspond to $N_{f,exp}/N_{f,cal}$ equal to 0.5 and 2, thus defining the scatter band 2.

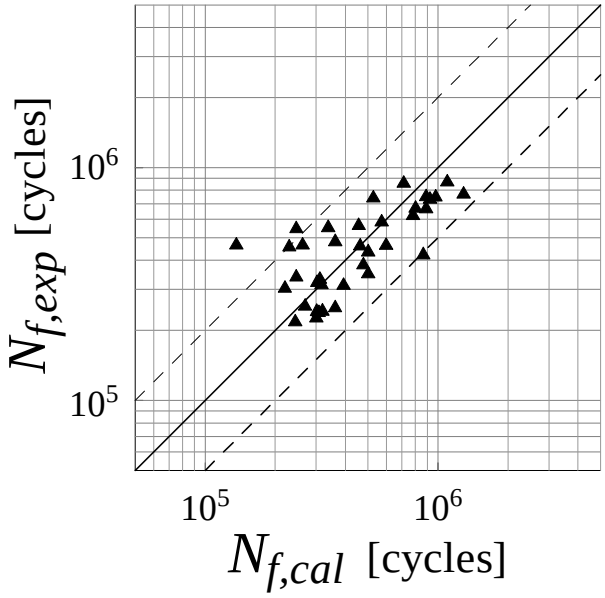

Figure 4.2 *Experimental fatigue life vs estimated fatigue life for each test analysed.*

It can be observed that 78% of the results fall within the scatter band 2, and 95% of the results fall within the scatter band 3. Therefore, the estimations seem to be quite satisfactory.

In more detail, the proposed methodology provides conservative estimations for one-third of the results (***Table 4.8***). Moreover, the accuracy of the criterion is verified by means of the root mean square error method: the value of T_{RMS} is equal to 1.75, which highlights a quite good accuracy of the criterion employed.

In conclusion, it can be stated that the estimated crack paths reproduce the experimental ones with good agreement for Al 2024-T351 alloy, and satisfactory predictions in terms of fretting fatigue life are provided by the methodology proposed in the present Ph.D. Thesis.

4.3 Al 7050-T7451 aluminium alloy

The experimental campaigns carried out by Rossino et al. (Rossino, 2009) and by Almeida et al. (Almeida, 2020) have been analysed by means of the proposed methodology. The experimental campaign carried out by Rossino et al.

(experimental campaign 1 in the following) is detailed in Section 4.3.1, whereas the results obtained by employing the proposed methodology are discussed in Section 4.3.2. The experimental campaign carried out by Almeida et al. (experimental campaign 2 in the following) is detailed in Section 4.3.3, whereas the results obtained by employing the proposed methodology are discussed in Section 4.3.4.

4.3.1 Experimental campaign 1

Ten flat dog-bone test specimens (named specimens from T1 to T10 in the following) made of Al 7050-T7451 alloy were tested. The mechanical and fatigue properties are listed in ***Table 4.3*** (Chen, 2012; Rossino, 2009).

Table 4.3 Mechanical and fatigue properties of Al 7050-T7451 alloy (Chen, 2012; Rossino, 2009), tested by Rossino et al. (Rossino, 2009).

MATERIAL	E [GPa]	ν	σ_u [MPa]	$\sigma_{af,-1}$ [MPa]	m	$\tau_{af,-1}$ [MPa]	m^*	N_0 [cycles]
Al 7050-T7451	73.4	0.33	513	301	-0.05	127	-0.08	$2\cdot 10^6$

The averaged grain size d is equal to $5\,\mu m$ (Rossino, 2009), whereas the coefficient of friction μ within the contact zone is equal to 0.54 (Rossino, 2009).

The experimental tests were carried out in partial slip regime by using two cylindrical pads (made of the same material of the specimens), characterised by a radius R equal to 70 mm. A constant normal load P and a cyclic tangential load $Q(t)$ (characterised by a loading ratio $R=-1$) were applied to the pads. Moreover, the specimen experienced a cyclic bulk stress $\sigma_B(t)$, which was characterised by a pulsation equal to that of $Q(t)$ and a phase shift of 180° with respect to $Q(t)$. Different mean values $\sigma_{B,m}$ of bulk stress were considered in the tests. Note that the mean bulk stress was applied to the specimen before clamping the pads, in order to avoid the influence of such a mean stress on the contact solution.

The loading parameters (normal load P, amplitude Q_a of the cyclic tangential load, and amplitude $\sigma_{B,a}$ and mean value $\sigma_{B,m}$ of the cyclic bulk stress) and the corresponding experimental fretting fatigue life $N_{f,exp}$ are listed in ***Table 4.4*** for each tested specimen. Note that run-out was reached for tests No. T9 and No. T10.

Table 4.4 Loading parameters (normal load P, amplitude Q_a of the cyclic tangential load, amplitude $\sigma_{B,a}$ and mean value $\sigma_{B,m}$ of the cyclic bulk stress), estimated crack path orientation θ_{cal}, experimental and estimated fretting fatigue life, $N_{f,exp}$ and $N_{f,cal}$, respectively, for each specimen tested by Rossino et al. (Rossino, 2009).

TEST No.	P [N/mm]	Q_a [N/mm]	$\sigma_{B,a}$ [MPa]	$\sigma_{B,m}$ [MPa]	θ_{cal} [°]	$N_{f,exp}$ [cycles]	$N_{f,cal}$ [cycles]	$\frac{N_{f,exp}}{N_{f,cal}}$
T1	654	163	92.7	15	2	164662	116521	1.41
T2	654	163	92.7	15	2	202609	116521	1.74
T3	654	163	92.7	0	2	198686	204687	0.97
T4	654	163	92.7	0	2	274248	204687	1.34
T5	654	163	92.7	-15	2	268230	364813	0.74
T6	654	163	92.7	-15	2	299568	364813	0.82
T7	654	163	92.7	-60	2	1304620	2269755	0.57
T8	654	163	92.7	-60	2	1552276	2269755	0.68
T9	654	163	92.7	-92.7	2	10000000*	9453212	-
T10	654	163	92.7	-145	2	10000000*	113098560	-

4.3.2 Results

The experimental campaign described in Section 4.3.1 has been analysed by means of the analytical methodology proposed in the present Ph.D. Thesis for fretting fatigue assessment of structural components.

As far as the crack path orientation is concerned, the angle θ_{cal} estimated by means of the proposed methodology was equal to 2° for each fretting loading condition (***Table 4.4***). More precisely, the theoretical crack nucleates at the contact trailing edge, and is characterized by a direction inward the contact region.

The experimental crack orientation of test No. T9 is compared to the corresponding analytical one in ***Figure 4.3***. Multiple experimental cracks were found at the contact trailing edge. The direction of such cracks was inward the contact region, in accordance with the theoretical estimations. However, the comparison between experimental and theoretical results is quite difficult, because the analytical ones can be estimated only related to a length of twice the averaged grain size of the material (corresponding to the length of the critical plane, $2d = 10\ \mu m$).

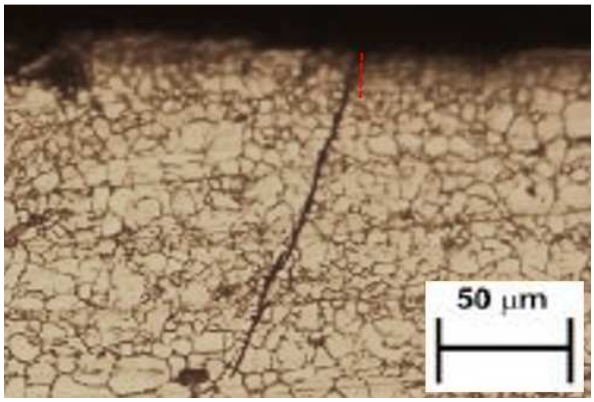

Figure 4.3 *Experimental crack path (Rossino, 2009) and theoretical crack orientation (dashed-red line) for test No. T9.*

As far as fatigue life is concerned, the number $N_{f,cal}$ of loading cycles to failure estimated by means of the proposed methodology is listed in ***Table 4.4*** for each specimen. The ratio $N_{f,exp}/N_{f,cal}$ is also listed in ***Table 4.4*** for tests No. from T1 to T8, by excluding the run-outs due to the fact that, in such cases, the experimental number of loading cycles to failure is unknown. Moreover, a comparison between experimental and estimated fatigue life is shown in ***Figure 4.4*** for tests No. from T1 to T8. Note that the dashed lines correspond to $N_{f,exp}/N_{f,cal}$ equal to 0.5 and 2, thus defining the scatter band 2.

It can be observed that all the results fall within the scatter band 2 and, therefore, the estimations seem to be quite satisfactory.

In more detail, the proposed methodology provides conservative estimations for tests No. from T1, T2 and T4, whereas results for the other tests are characterised by $N_{f,cal} > N_{f,exp}$ (***Table 4.4***). Moreover, the accuracy of the criterion is verified by means of the root mean square error method: for as-received specimens, the value of T_{RMS} is equal to 1.45, which highlights a quite good accuracy of the criterion employed.

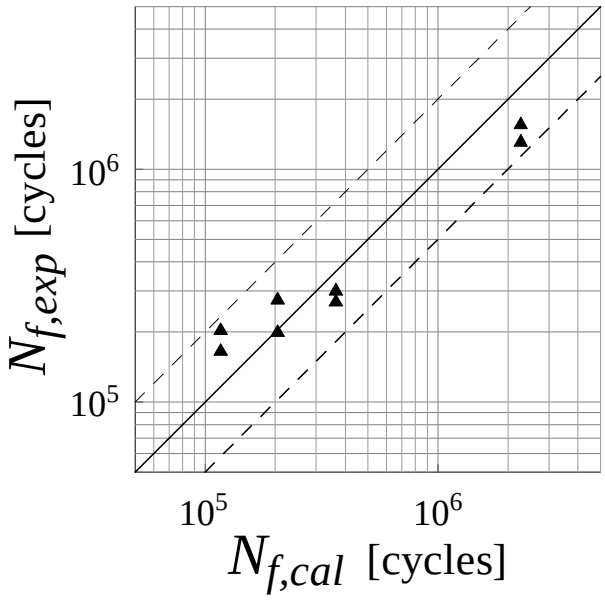

Figure 4.4 *Experimental fatigue life vs. estimated fatigue life for tests No. from T1 to T8.*

Moreover, as far as the run-outs (i.e., tests No. T9 and T10) are concerned, the proposed methodology estimates a number of loading cycles to failure slightly lower than the value of run-out for test No. T9 and higher than the value of run-out for test No. T10.

Therefore, it can be stated that the methodology proposed in the present Ph.D. Thesis provides fretting fatigue life estimations characterised by a quite satisfactory accuracy in case of either tensile or compressive mean bulk stress applied to the specimen.

4.3.3 Experimental campaign 2

Nineteen flat dog-bone test specimens (named specimens from T1 to T19 in the following) made of Al 7050-T7451 alloy were tested. The mechanical and fatigue properties are listed in ***Table 4.5*** (Almeida, 2020; Chen, 2012).

Table 4.5 Mechanical and fatigue properties of Al 7050-T7451 alloy (Almeida, 2020; Chen, 2012), tested by Almeida et al. (Almeida, 2020).

MATERIAL	E [GPa]	ν	σ_u [MPa]	$\sigma_{af,-1}$ [MPa]	m	$\tau_{af,-1}$ [MPa]	m^*	N_0 [cycles]
Al 7050-T7451	71.7	0.33	524	301	-0.05	127	-0.08	$2\cdot 10^6$

The averaged grain size d is equal to $8\,\mu m$ (Almeida, 2020), whereas the coefficient of friction μ within the contact zone is equal to 0.54 (Rossino, 2009).

The experimental tests were carried out in partial slip regime by using two cylindrical pads (made of the same material of the specimens). Note that two different values of the pad radius were used, that is, R equal to 30 mm and 70 mm. A constant normal load P and a cyclic tangential load $Q(t)$ (characterised by a loading ratio $R=-1$) were applied to the pads. Moreover, a constant bulk stress σ_B was applied to the specimen before clamping the pads, in order to avoid the influence of such a mean stress on the contact solution.

All the tests were interrupted at 10^6 loading cycles and, subsequently, crack direction was measured on the longitudinal middle-cross section by means of a confocal laser microscope. The experimental crack path orientation θ_{exp} is defined as the angle between the crack direction and a line perpendicular to the surface. Such an angle is measured for a specific distance from the surface, and it is defined positive if the crack path is inside the contact zone. Note that, when multiple cracks were observed, only the longest one was considered.

The pad radius R, the loading parameters (normal load P, amplitude Q_a of the cyclic tangential load, and bulk stress σ_B) and the corresponding experimental crack path orientation θ_{exp} (measured at a distance equal to $56.5\,\mu m$ from the surface) are listed in ***Table 4.6*** for each tested specimen.

Table 4.6 Pad radius R, loading parameters (normal load P, amplitude Q_a of the cyclic tangential load, and bulk stress σ_B), experimental and estimated crack path orientation, θ_{exp} and θ_{cal}, respectively, and estimated fretting fatigue life $N_{f,cal}$, for each specimen tested by Almeida et al. (Almeida, 2020).

TEST No.	R [mm]	P [N/mm]	Q_a [N/mm]	σ_B [MPa]	θ_{exp} [°]	θ_{cal} [°]	$N_{f,cal}$ [cycles]
T1	70	800	240	0	7.3	3	115930572
T2	70	800	240	0	41.5	3	115930572
T3	70	800	320	0	24.8	3	4457854
T4	70	800	320	0	36.6	3	4457854
T5	70	800	320	0	37.5	3	4457854
T6	70	800	400	0	32.5	3	352292
T7	70	800	400	0	37.0	3	352292
T8	70	800	320	25	54.4	3	1942145
T9	70	800	320	25	17.3	3	1942145
T10	70	800	320	25	42.5	3	1942145
T11	70	800	320	50	55.6	3	813926
T12	70	800	320	50	32.8	3	813926
T13	70	800	320	50	42.6	3	813926
T14	30	341	136	0	39.9	5	73786216
T15	30	341	136	0	24.2	5	73786216
T16	30	341	136	25	31.3	5	34655327
T17	30	341	136	25	31.7	5	34655327
T18	30	341	136	50	36.3	4	12939376
T19	30	341	136	50	33.7	4	12939376

4.3.4 Results

The experimental campaign described in Section 4.3.3 has been analysed by means of the analytical methodology proposed in the present Ph.D. Thesis for fretting fatigue assessment of structural components.

As far as the crack path orientation is concerned, the angle θ_{cal} estimated by means of the proposed methodology was equal to 3° for tests No. from T1 to T13, 5° for tests No. from T14 to T17, and 4° for tests No. T18 and T19 (***Table 4.6***).

More precisely, the theoretical crack nucleates at the contact trailing edge, and is characterized by a direction inward the contact region for each test.

The direction of experimental cracks was found to be inward the contact region for all the tests, in accordance with the theoretical estimations. The experimental crack orientations are compared to the corresponding analytical ones in ***Figure 4.5***, for each test configuration. Note that the experimental crack orientations were measured at a distance equal to $56.5\,\mu m$ from the surface, whereas the theoretical crack orientations are related to a length equal to twice the averaged grain size of the material that is, $2d = 16\,\mu m$.

An analytical simulation of the above experimental tests was also provided by Almeida et al. (Almeida, 2020). Three different multiaxial fatigue parameters were employed, that is, the SWT parameter proposed by Smith, Watson and Topper (Smith, 1970), the FS parameter proposed by Fatemi and Socie (Fatemi, 1988), and the Modified Wohler Curve Method (MWCM) parameter (Susmel, 2002). Moreover, three different critical plane averaging methods were applied using the above parameters, in order to estimate the initial crack direction. Note that the estimated crack orientations are related to a length ranging from about $100\,\mu m$ to $200\,\mu m$, depending on the employed method.

Almeida et al. observed that the results determined by employing the SWT parameter estimated the experimental crack paths better than those determined by using the shear-based parameters (i.e., the FS and MWCM parameters). In particular, the crack direction was generally predicted inward the contact region by employing the SWT parameter, with estimated angles ranging from -4° to 7°, while estimated crack direction was generally outward the contact region by employing the shear-based parameters (when associated with the Critical Direction Method, the MWCM predicted crack directions inward the contact region, with estimated angles ranging from 61° to 75°).

Therefore, it can be stated that the methodology proposed in the present Ph.D. Thesis provides more appropriate results in terms of crack path orientation with respect to other shear-based criteria available in the literature. More precisely, such a methodology correctly predicts crack directions inward the contact region, with crack angles comparable to those estimated by means of a SWT parameter-based approach available in the literature.

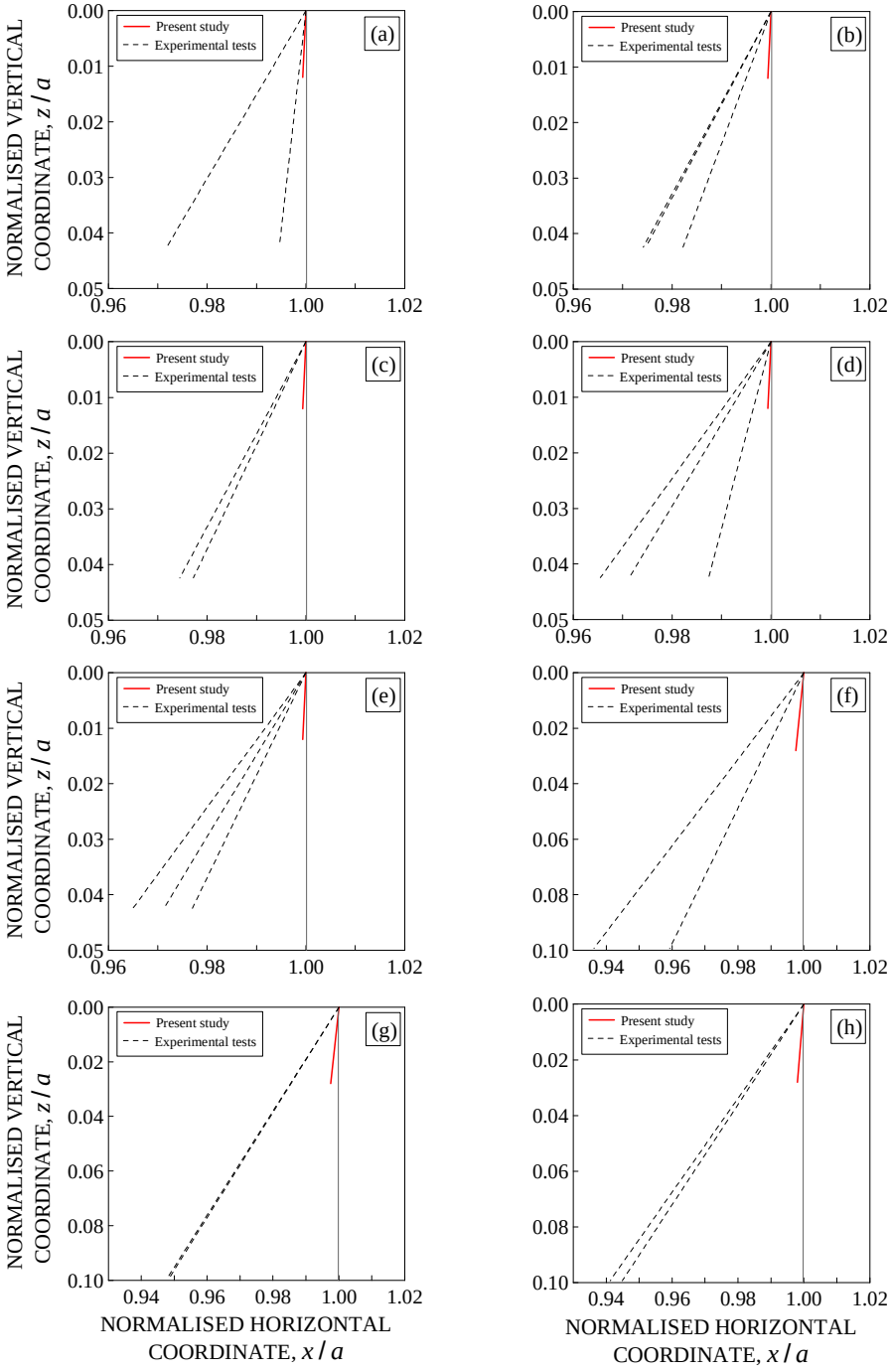

Figure 4.5 *Experimental and theoretical crack orientation for tests No. (a) T1-T2, (b)T3-T4-T5, (c) T6-T7, (d) T8-T9-T10, (e) T11-T12-T13, (f) T14-T15, (g) T16-T17, and (h) T18-T19.*

As far as fatigue life is concerned, the number $N_{f,cal}$ of loading cycles to failure estimated by means of the proposed methodology is listed in ***Table 4.4*** for each specimen. Note that a comparison between experimental and estimated fatigue life is not possible, since the experimental number of loading cycles to failure is unknown for all the tests. Nevertheless, it can be observed that, for 74% of the tests analysed, the loading cycle number estimated by means of the proposed methodology is higher than the value of run-out.

4.4 Al 7075-T651 aluminium alloy

The experimental campaigns carried out by Vázquez et al. (Vázquez, 2012) and by Vázquez et al. (Vázquez, 2017) have been analysed through the proposed methodology. The experimental campaign carried out by Vázquez et al. in 2012 (experimental campaign 1 in the following) is detailed in Section 4.4.1, whereas the results determined by employing the proposed methodology are discussed in Section 4.4.2. The experimental campaign carried out by Vázquez et al. in 2017 (experimental campaign 2 in the following) is detailed in Section 4.4.3, whereas the results determined by employing the proposed methodology are discussed in Section 4.4.4.

4.4.1 Experimental campaign 1

Thirteen flat dog-bone test specimens made of Al 7075-T651 alloy were tested. The mechanical and fatigue properties are listed in ***Table 4.7*** (Vázquez, 2012). The averaged grain size d is equal to $50\ \mu m$ (Abrahams, 2019).

Table 4.7 Mechanical and fatigue properties of Al 7075-T651 alloy (Vázquez, 2012), tested by Vázquez et al. (Vázquez, 2012).

MATERIAL	E [GPa]	ν	σ_u [MPa]	$\sigma_{af,-1}$ [MPa]	m	$\tau_{af,-1}$ [MPa]	m^*	N_0 [cycles]
Al 7075-T651	71	0.33	572	193	-0.12	111	-0.12	$2\cdot10^6$

Before testing, seven specimens (from No. T1 to T7) were subjected to a shot peening treatment, whereas six specimens (from No. R1 to R6) were not treated and tested as reference.

The superficial treatment was characterised by an Almen intensity equal to 20-24A and a complete coverage condition. After shot peening, the specimens were polished in order to restore the un-treated superficial roughness. The coefficient of friction μ after the polish treatment was equal to 1.18, similar to that of the as-received specimens which was equal to 1.20 (Vázquez, 2012).

The residual stress field up to a depth of $1\,mm$ was measured by means of the Blind-Hole method. The residual stress distribution, measured both immediately after the superficial treatment (that is, before fretting fatigue tests) and after 10^4 fretting fatigue loading cycles, is shown in ***Figure 4.6***, where each band represents different values of the measurements performed (Vázquez, 2012). It can be considered that the phenomenon of relaxation is included in the residual stress distribution measured after 10^4 fretting fatigue loading cycles, since relaxation is mainly produced during the first fretting fatigue loading cycles.

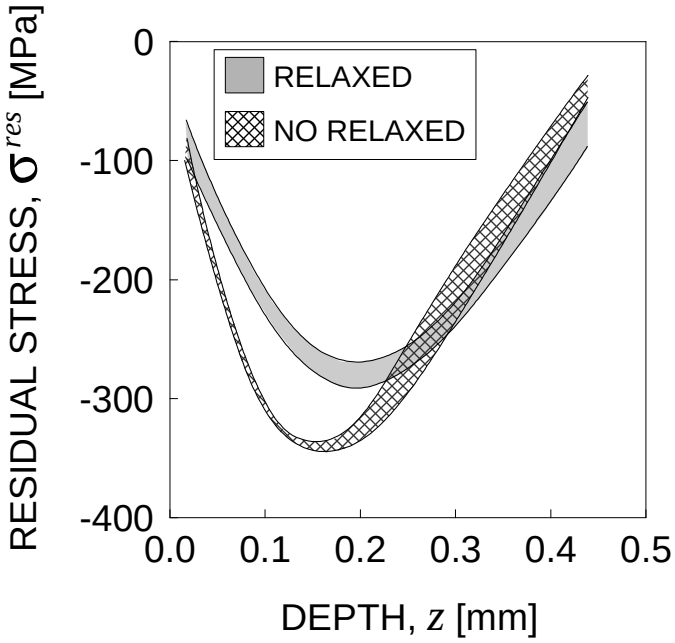

Figure 4.6 *Measured residual stress profiles due to shot peening treatment performed on specimens No. T1-T7.*

The experimental tests were carried out in partial slip regime by using two spherical pads (made of the same material of the specimens), characterised by a radius R equal to 100 mm. A constant normal load P and a cyclic tangential load $Q(t)$ (characterised by a loading ratio $R=-1$) were applied to the pads. Moreover, the specimen experienced a cyclic bulk stress $\sigma_B(t)$ (characterised by a loading ratio $R=-1$), which was in-phase with $Q(t)$.

The loading parameters (normal load P, amplitude Q_a of the cyclic tangential load, and amplitude $\sigma_{B,a}$ of the cyclic bulk stress) and the corresponding experimental fretting fatigue life $N_{f,exp}$ are listed in ***Table 4.8*** for each tested specimen.

Table 4.8 Loading parameters (normal load P, amplitude Q_a of the cyclic tangential load, amplitude $\sigma_{B,a}$ of the cyclic bulk stress), estimated crack path orientation θ_{cal}, experimental and estimated fretting fatigue life, $N_{f,exp}$ and $N_{f,cal}$, respectively, for each specimen tested by Vázquez et al. (Vázquez, 2012).

TEST No.	P [N]	Q_a [N]	$\sigma_{B,a}$ [MPa]	θ_{cal} [°]	$N_{f,exp}$ [cycles]	$N_{f,cal}$ [cycles]	$\frac{N_{f,exp}}{N_{f,cal}}$
R1	1200	1100	90	8	55759	42852	1.30
R2	1200	1100	100	8	51787	34198	1.51
R3	1000	900	110	8	59793	51475	1.16
R4	1000	900	125	7	65614	36043	1.82
R5	650	600	125	8	52499	75805	0.69
R6	650	600	125	8	47379	75805	0.63
T1	1200	1100	90	10	283522	317811	0.89
T2	1200	1100	100	9	191755	238211	0.81
T3	1000	900	110	9	238394	404952	0.59
T4	1000	900	125	9	196035	259454	0.76
T5	1000	900	125	9	214425	259454	0.83
T6	650	600	125	9	588006	673885	0.87
T7	650	600	125	9	941615	673885	1.40

4.4.2 Results

The experimental campaign described in Section 4.4.1 has been analysed by means of the analytical methodology proposed in the present Ph.D. Thesis for fretting fatigue assessment of structural components.

It can be highlighted that, in case of shot-peened specimens (that is, T-series test specimens), the measured relaxed residual stress field shown in ***Figure 4.6*** is taken into account in the stress field evaluation.

As far as the crack path orientation is concerned, the angles θ_{cal} estimated by means of the proposed methodology range from 7-8°, for R-series test specimens, to 9-10°, for T-series test specimens (***Table 4.8***). More precisely, the theoretical crack nucleates at the contact trailing edge, and is characterized by a direction inward the contact region.

No data in terms of experimental crack path are available for the tests considered. However, additional specimens subjected to fretting loading conditions equal to those used in tests No. T4-T5 and T6-T7 were tested in order to experimentally analyse the crack initiation path. The experimental crack orientations of such additional tests are compared to the corresponding analytical ones in ***Figure 4.7***. It can be observed that the experimental cracks nucleated at the contact trailing edge and grew inward the contact region, in accordance with the theoretical estimations.

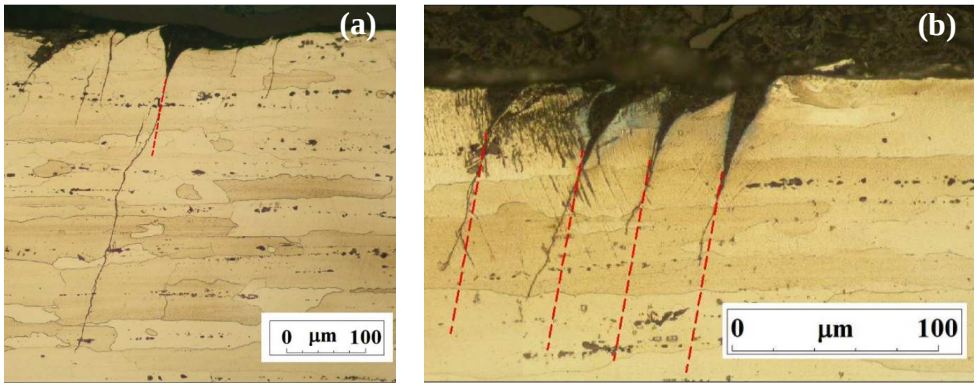

Figure 4.7 *Experimental crack path (Vázquez, 2012) and theoretical crack orientation (dashed-red lines) for fretting fatigue configurations of tests No. (a) T4-T5, and (b) T6-T7.*

However, further comparisons with the theoretical results are quite difficult. In particular, the experimental cracks showed some direction changes, whereas the proposed methodology contemplates a single critical plane orientation related to a process zone characterised by the size equal to twice the averaged grain size. Moreover, multiple cracks were found in the specimen characterised by the loading configuration of tests No. T6-T7, whereas a single crack starting from the hot-spot at the contact trailing edge is considered in the proposed methodology.

As far as fatigue life is concerned, the number $N_{f,cal}$ of loading cycles to failure computed by means of the proposed methodology is listed in ***Table 4.8*** for each specimen, together with the ratio $N_{f,exp}/N_{f,cal}$. Moreover, comparisons between experimental and estimated fatigue life are shown in ***Figure 4.8a*** and ***Figure 4.8b***, for each test of the R-series (i.e. as-received specimens) and the T-series (i.e. shot-peened specimens), respectively. Note that the dashed lines correspond to $N_{f,exp}/N_{f,cal}$ equal to 0.5 and 2, thus defining the scatter band 2.

It can be observed that all results fall within the scatter band 2, and therefore, the estimations seem to be quite satisfactory.

Related to the R-series, the proposed methodology provides conservative estimations for tests No. from R1 to R4, whereas results for the loading configuration of tests No. R5 and R6 are characterised by $N_{f,cal} > N_{f,exp}$ (***Table 4.8***). Moreover, the accuracy of the criterion is verified by means of the root mean square error method: the value of T_{RMS} for as-received specimens is equal to 1.50, which highlights a quite good accuracy of the criterion employed.

A numerical simulation of the above R-series experimental tests was also carried out by Vázquez et al. (Vázquez, 2014) employing a numerical methodology that combines crack initiation and propagation. The comparison between experimental and estimated fatigue life is shown in ***Figure 4.8a***. It can be noticed that almost all the results fall within the scatter band 2, and all the estimations are conservative. The computed value of T_{RMS} is equal to 1.59.

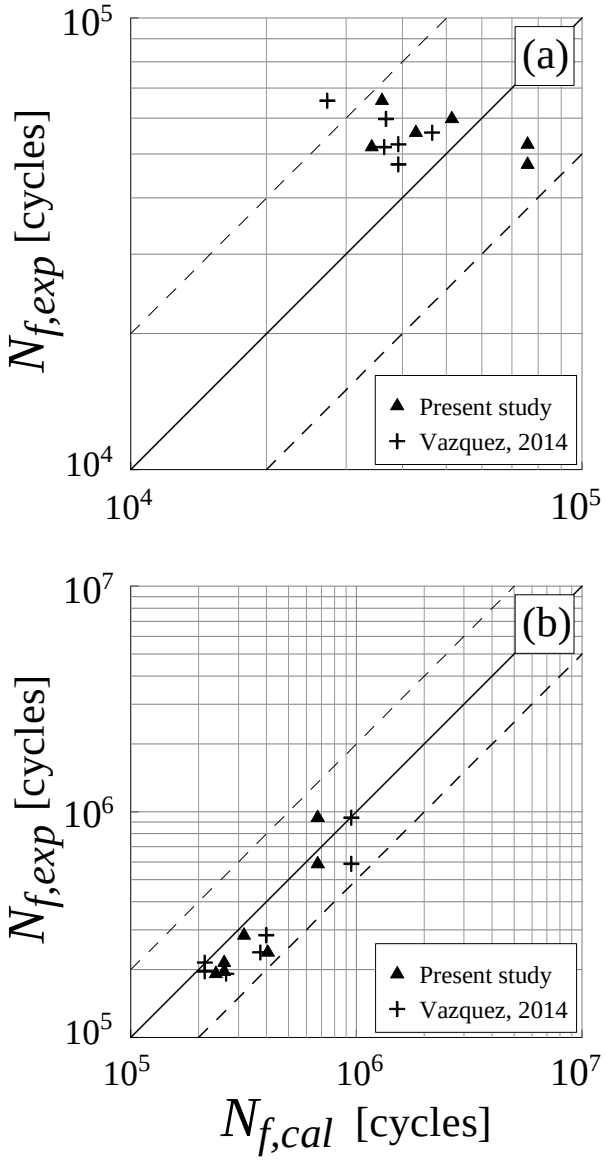

Figure 4.8 *Experimental fatigue life vs. estimated fatigue life for each test of (a) the R-series and (b) the T-series. The numerical results obtained by Vázquez et al. (Vázquez, 2014) are also reported.*

Related to the T-series, the proposed methodology provides conservative estimations for test No. T7, whereas results for the other tests are characterised by $N_{f,cal} > N_{f,exp}$ (***Table 4.8***). Moreover, the accuracy of the criterion is verified by

means of the root mean square error method: the value of T_{RMS} for as-received specimens is equal to 1.34, which highlights a quite good accuracy of the criterion employed.

A numerical simulation of the above T-series experimental tests was also provided by Vázquez et al. (Vázquez, 2014). The comparison between experimental and estimated fatigue life is shown in ***Figure 4.8b***. It can be remarked that all the results fall within the scatter band 2, and almost all the estimations are non-conservative. The computed value of T_{RMS} is equal to 1.36.

Therefore, it can be stated that the methodology proposed in the present Ph.D. Thesis provides results characterised by a satisfactory accuracy, comparable with that related to a more complex numerical approach, even in the case of shot-peened specimens. The estimations in terms of fatigue life seem to be less conservative for shot-peened specimens than those for untreated specimens.

4.4.3 Experimental campaign 2

Six flat dog-bone test specimens (named specimens from T1 to T6 in the following) made of Al 7075-T651 alloy were tested. The mechanical and fatigue properties are listed in ***Table 4.9*** (Vázquez, 2012).

Table 4.9 Mechanical and fatigue properties of Al 7075-T651 alloy (Vázquez, 2012), tested by Vázquez et al. (Vázquez, 2017).

MATERIAL	E [GPa]	ν	σ_u [MPa]	$\sigma_{af,-1}$ [MPa]	m	$\tau_{af,-1}$ [MPa]	m^*	N_0 [cycles]
Al 7075-T651	71	0.33	572	193	-0.12	111	-0.12	$2 \cdot 10^6$

The averaged grain size d is equal to $50\,\mu m$ (Abrahams, 2019), whereas the coefficient of friction μ within the contact zone is equal to 0.72 (Vázquez, 2017).

The experimental tests were carried out in partial slip regime by using two cylindrical pads (made of the same material of the specimens), characterised by a radiu R equal to 100 mm. A constant normal load P and a cyclic tangential load

$Q(t)$ (characterised by a loading ratio $R=-1$) were applied to the pads. Moreover, the specimen experienced a cyclic bulk stress $\sigma_B(t)$ (characterised by a loading ratio $R=-1$), which was in-phase with $Q(t)$.

The loading parameters (normal load P, amplitude Q_a of the cyclic tangential load, and amplitude $\sigma_{B,a}$ of the cyclic bulk stress) and the corresponding experimental fretting fatigue life $N_{f,exp}$ are listed in ***Table 4.10*** for each tested specimen.

Table 4.10 Loading parameters (normal load P, amplitude Q_a of the cyclic tangential load, amplitude $\sigma_{B,a}$ of the cyclic bulk stress), estimated crack path orientation θ_{cal}, experimental and estimated fretting fatigue life, $N_{f,exp}$ and $N_{f,cal}$, respectively, for each specimen tested by Vázquez et al. (Vázquez, 2017).

TEST No.	P [N/mm]	Q_a [N/mm]	$\sigma_{B,a}$ [MPa]	θ_{cal} [°]	$N_{f,exp}$ [cycles]	$N_{f,cal}$ [cycles]	$\frac{N_{f,exp}}{N_{f,cal}}$
T1	829	121	50	11	577540	927565	0.62
T2	829	121	50	11	676704	927565	0.73
T3	829	157	55	10	252878	398954	0.63
T4	829	157	55	10	283110	398954	0.71
T5	829	193	70	9	167324	149832	1.12
T6	829	193	70	9	162421	149832	1.08

4.4.4 Results

The experimental campaign described in Section 4.4.3 has been analysed by means of the analytical methodology proposed in the present Ph.D. Thesis for fretting fatigue assessment of structural components.

As far as the crack path orientation is concerned, the angle θ_{cal} estimated by means of the proposed methodology was equal to 11° for tests No. T1-T2, 10° for tests No. T3-T4, and 9° for tests No. T5-T6 (***Table 4.10***). More precisely, the theoretical crack nucleates at the contact trailing edge, and is characterized by a direction inward the contact region for each test.

The direction of experimental cracks was found to be inward the contact region for all the tests, in accordance with the theoretical estimations. The experimental crack paths are compared to the corresponding analytical ones in ***Figure 4.9***, for tests No. T1, T3 and T5. It can be noticed that the estimated crack paths agree quite well with those obtained from the experimental tests, with angular difference equal to about 9°, 6° and 3° for tests No. T1, T3 and T5, respectively.

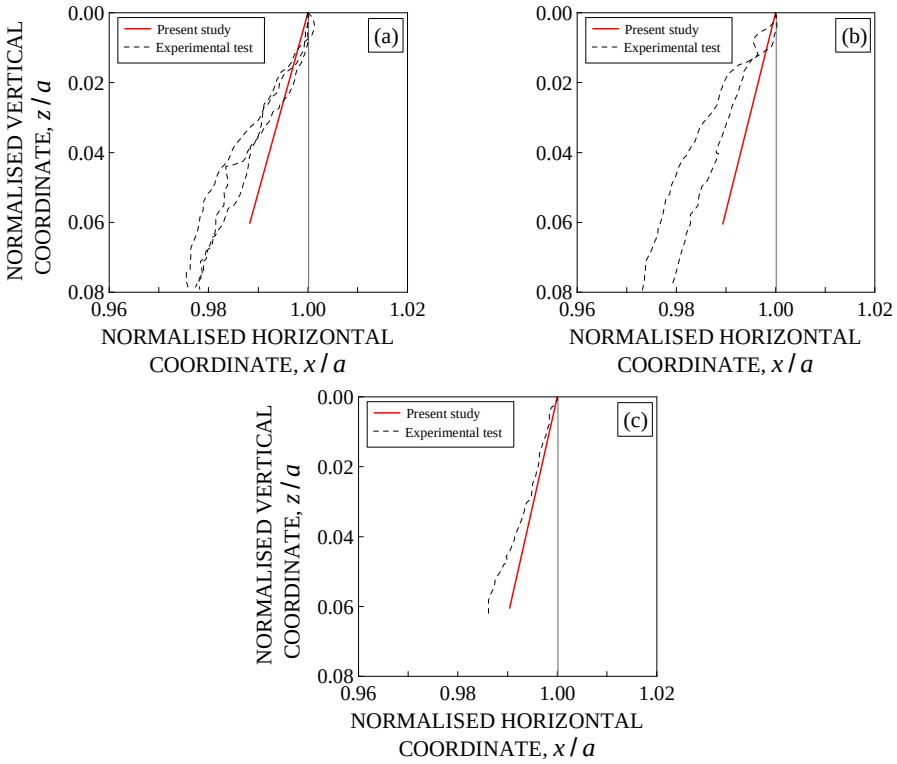

Figure 4.9 *Experimental and theoretical crack paths for tests No. (a) T1, (b)T3, and (c) T5.*

As far as fatigue life is concerned, the number $N_{f,cal}$ of loading cycles to failure estimated by means of the proposed methodology is listed in ***Table 4.10*** for each specimen, together with the ratio $N_{f,exp}/N_{f,cal}$. Moreover, a comparison between experimental and estimated fatigue life is shown in ***Figure 4.10*** for each test analysed. Note that the dashed lines correspond to $N_{f,exp}/N_{f,cal}$ equal to 0.5 and 2, thus defining the scatter band 2.

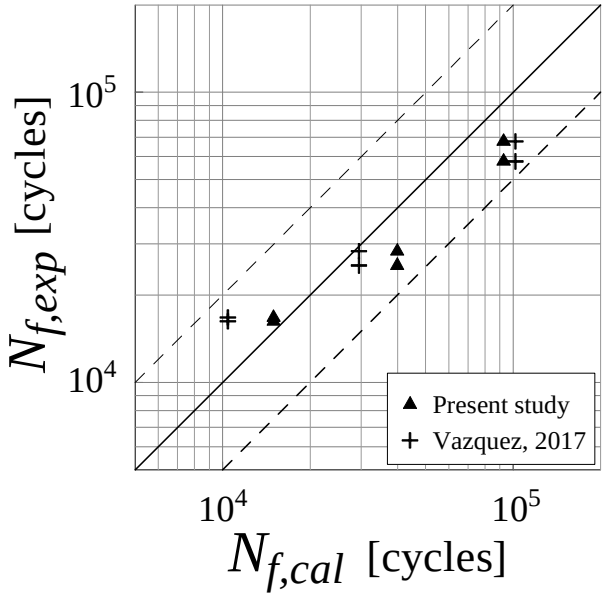

Figure 4.10 *Experimental fatigue life vs. estimated fatigue life for each test analysed. The numerical results obtained by Vázquez et al. (Vázquez, 2017) are also reported.*

It can be observed that all the results fall within the scatter band 2 and, therefore, the estimations are quite satisfactory. Moreover, the accuracy of the criterion is verified by means of the root mean square error method: the value of T_{RMS} is equal to 1.40.

Therefore, it can be stated that the estimated crack paths reproduce the experimental ones with good agreement for Al 7075-T651 alloy, and a satisfactory prediction in terms of fretting fatigue life is determined by employing the methodology proposed in the present Ph.D. Thesis.

4.5 Al-4Cu aluminium alloy

The experimental campaign carried out by Araújo et al. (Araújo, 2004) has been analysed by means of the proposed methodology. Such an experimental campaign is detailed in Section 4.5.1, whereas the results derived by employing the proposed methodology are discussed in Section 4.5.2.

4.2.1 Experimental campaign

Flat dog-bone specimens made of Al-4Cu alloy were tested. The mechanical and fatigue properties are listed in ***Table 4.11*** (Araújo, 2004).

Table 4.11 Mechanical and fatigue properties of Al 2024-T351 alloy (Araújo, 2004).

MATERIAL	E [GPa]	ν	σ_y [MPa]	$\sigma_{af,-1}$ [MPa]	m	$\tau_{af,-1}$ [MPa]	m^*	N_0 [cycles]
Al-4Cu	74	0.33	465	191	-0.11	110	-0.11	$2\cdot10^6$

The averaged grain size d is equal to $50\,\mu m$ (Araújo, 2004), whereas the coefficient of friction μ within the contact zone is equal to 0.75 (Araújo, 2004).

The experimental tests were carried out in partial slip regime by using two cylindrical pads (made of the same material of the specimens). Note that different values of the pad radius R were used. A constant normal load P and a cyclic tangential load $Q(t)$ (characterised by a loading ratio $R=-1$) were applied to the pads. Moreover, the specimen experienced a cyclic bulk stress $\sigma_B(t)$ (characterised by a loading ratio $R=-1$), which was in-phase with $Q(t)$. Twenty-nine different fretting fatigue configurations were examined, and some specimens were tested for each configuration.

The pad radius R, the loading parameters (normal load P, amplitude Q_a of the cyclic tangential load, and amplitude $\sigma_{B,a}$ of the cyclic bulk stress) and the corresponding experimental fretting fatigue life $N_{f,exp}$ are listed in ***Table 4.12*** for each fretting fatigue configuration. Note that in some cases, characterised by small contact area, failure was caused by anomalous cracks originated out of the contact zone in regions of poor surface finish. Therefore, in such cases characterised by a non-acceptable failure mode, the number of loading cycles to failure (marked with "*" in ***Table 4.12***) may be considered as a lower limit.

Table 4.12 Pad radius R, loading parameters (normal load P, amplitude Q_a of the cyclic tangential load, amplitude $\sigma_{B,a}$ of the cyclic bulk stress), estimated crack orientation θ_{cal}, experimental $N_{f,exp}$ and estimated $N_{f,cal}$ fretting fatigue life, for each configuration.

TEST No.	R [mm]	P [N/mm]	Q_a [N/mm]	$\sigma_{B,a}$ [MPa]	θ_{cal} [°]	$N_{f,exp}$ [cycles]	$N_{f,cal}$ [cycles]	$\frac{N_{f,exp}}{N_{f,cal}}$
T1	12.5	23	10	92.7	1	1000000*	19117479	-
T2	25	47	21	92.7	3	1000000*	7717940	-
T3	37.5	70	31	92.7	5	1000000*	3668776	-
T4	50	93	42	92.7	5	1290000	2043901	0.63
T5	75	140	63	92.7	6	670000	998311	0.67
T6	100	186	84	92.7	5	850000	628223	1.35
T7	125	233	105	92.7	5	730000	464568	1.57
T8	150	280	126	92.7	5	670000	372451	1.80
T9	12.5	19	9	92.7	0	1000000*	20524101	-
T10	25	39	17	92.7	3	1000000*	10103129	-
T11	37.5	58	26	92.7	4	4040000	4941405	0.82
T12	50	77	35	92.7	5	1500000	2913246	0.51
T13	75	116	52	92.7	5	800000	1411144	0.57
T14	100	155	70	92.7	5	610000	904978	0.67
T15	125	193	87	92.7	5	1240000	668421	1.86
T16	150	232	104	92.7	5	690000	534939	1.29
T17	12.5	19	9	77.2	1	1000000*	56423724	-
T18	25	39	17	77.2	3	1000000*	23500510	-
T19	50	77	35	77.2	5	1000000*	5848140	-
T20	75	116	52	77.2	6	1420000	2689769	0.53
T21	100	155	70	77.2	6	610000	1645611	0.37
T22	125	193	87	77.2	5	1240000	1163687	1.07
T23	25	27	12	61.8	2	1000000*	103940553	-
T24	37.5	41	18	61.8	4	1000000*	50712396	-
T25	50	54	25	61.8	5	1000000*	27728846	-
T26	75	82	37	61.8	6	1000000*	11943853	-
T27	100	109	49	61.8	6	1000000*	6918770	-
T28	125	136	61	61.8	6	1570000	4761295	0.33
T29	150	163	74	61.8	6	1230000	3621014	0.34

4.5.2 Results

The experimental campaign described in Section 4.5.1 has been analysed by means of the analytical methodology proposed in the present Ph.D. Thesis for fretting fatigue assessment of structural components.

As far as the crack path orientation is concerned, the angle θ_{cal} estimated by means of the proposed methodology ranges from 0° to 6°, depending on the fretting loading conditions (***Table 4.2***). More precisely, the theoretical crack nucleates at the contact trailing edge, and is characterized by a direction perpendicular to the contact surface (for test configuration No. T9) or inward the contact region.

The experimental cracks were generally found to nucleate at or close to the contact trailing edge, and to grow approximately perpendicular to the surface, in accordance with the theoretical estimations.

As far as fatigue life is concerned, the number $N_{f,cal}$ of loading cycles to failure estimated by means of the proposed methodology is listed in ***Table 4.12*** for each test configuration. The ratio $N_{f,exp}/N_{f,cal}$ is also listed in ***Table 4.12*** for test configurations characterized by an acceptable failure mode.

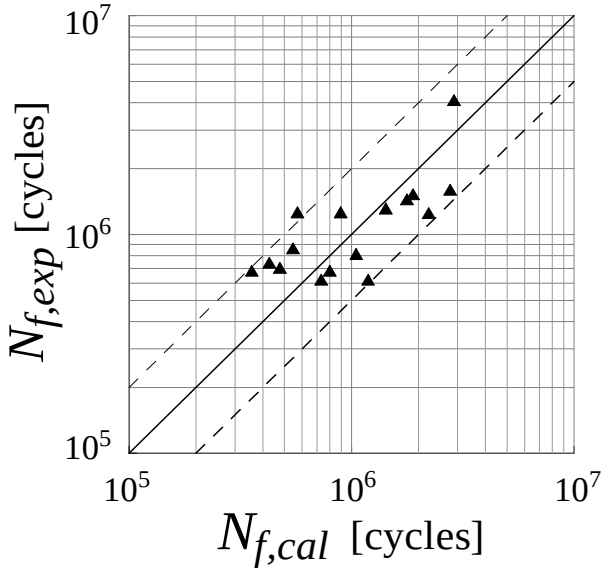

Figure 4.11 *Experimental fatigue life vs. estimated fatigue life for tests characterised by acceptable failure modes.*

Moreover, a comparison between experimental and estimated fatigue life is shown in ***Figure 4.11*** for such test configurations. Note that the dashed lines correspond to $N_{f,exp}/N_{f,cal}$ equal to 0.5 and 2, thus defining the scatter band 2.

It can be observed that 81% of the results fall within the scatter band 2, and 94% of the results fall within the scatter band 3. Therefore, the estimations seem to be quite satisfactory. In more detail, the proposed methodology provides conservative estimations for 38% of tests (***Table 4.12***). Moreover, the accuracy of the criterion is verified by means of the root mean square error method: the value of T_{RMS} is equal to 1.86, which highlights a quite good accuracy of the criterion employed.

As far as the specimens characterised by non-acceptable failure modes are concerned, for 69% of analysed test configurations the proposed methodology estimates a number of loading cycles to failure higher than the value considered as a lower limit listed in ***Table 4.12***.

Therefore, it can be stated that the methodology proposed in the present Ph.D. Thesis provides quite satisfactory results in terms of both crack path orientation and fretting fatigue life for Al-4Cu alloy.

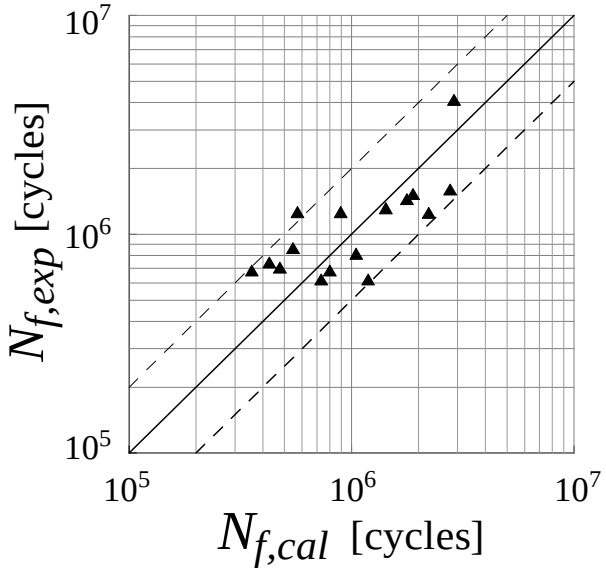

Figure 4.11 *Experimental fatigue life vs. estimated fatigue life for tests characterised by acceptable failure modes.*

4.6 Ti-6Al-4V titanium alloy

The experimental campaign carried out by Araújo et al. (Araújo, 2004) has been analysed by means of the proposed methodology. Such an experimental campaign is detailed in Section 4.6.1, whereas the results determined by employing the proposed methodology are discussed in Section 4.6.2.

4.6.1 Experimental campaign

Flat dog-bone test specimens made of Ti-6Al-4V alloy were tested. The mechanical and fatigue properties are listed in ***Table 4.13*** (Araújo, 2004).

The averaged grain size d is equal to $5\,\mu m$ (Araújo, 2004), whereas the coefficient of friction μ within the contact zone is equal to 0.55 (Araújo, 2004).

Table 4.13 Mechanical and fatigue properties of Al 2024-T351 alloy (Araújo, 2004).

MATERIAL	E [GPa]	ν	σ_y [MPa]	$\sigma_{af,-1}$ [MPa]	m	$\tau_{af,-1}$ [MPa]	m^*	N_0 [cycles]
Ti-6Al-4V	115	0.32	974	418	-0.10	241	-0.10	$2\cdot 10^6$

The experimental tests were carried out in partial slip regime by using two cylindrical pads (made of the same material of the specimens). Note that different values of the pad radius R were used. A constant normal load P and a cyclic tangential load $Q(t)$ (characterised by a loading ratio $R=-1$) were applied to the pads. Moreover, the specimen experienced a cyclic bulk stress $\sigma_B(t)$ (characterised by a loading ratio $R=-1$), which was in-phase with $Q(t)$. Five different fretting fatigue configurations were examined, and some specimens were tested for each configuration.

The pad radius R, the loading parameters (normal load P, amplitude Q_a of the cyclic tangential load, and amplitude $\sigma_{B,a}$ of the cyclic bulk stress) and the corresponding experimental fretting fatigue life $N_{f,exp}$ are listed in ***Table 4.14*** for each fretting fatigue configuration. Note that, in the tests of configuration No. T1 (that is, tests characterised by the smallest contact area), failure was caused by

anomalous cracks originated out of the contact zone in regions of poor surface finish. Therefore, in such cases characterised by a non-acceptable failure mode, the number of loading cycles to failure (marked with "*" in ***Table 4.12***) may be considered as a lower limit.

Table 4.14 Pad radius R, loading parameters (normal load P, amplitude Q_a of the cyclic tangential load, amplitude $\sigma_{B,a}$ of the cyclic bulk stress), estimated crack orientation θ_{cal}, experimental $N_{f,exp}$ and estimated $N_{f,cal}$ fretting fatigue life, for each configuration.

TEST No.	R [mm]	P [N/mm]	Q_a [N/mm]	$\sigma_{B,a}$ [MPa]	θ_{cal} [°]	$N_{f,exp}$ [cycles]	$N_{f,cal}$ [cycles]	$\frac{N_{f,exp}}{N_{f,cal}}$
T1	12.5	259	41	280	4	1400000*	1716677	-
T2	37.5	777	124	280	2	521000	310142	1.68
T3	50	1036	166	280	2	374000	231261	1.62
T4	60	1243	199	280	2	196000	196194	1.00
T5	70	1450	232	280	2	173000	172704	1.00

4.6.2 Results

The experimental campaign described in Section 4.6.1 has been analysed by means of the analytical methodology proposed in the present Ph.D. Thesis for fretting fatigue assessment of structural components.

As far as the crack path orientation is concerned, the angle θ_{cal} estimated by means of the proposed methodology was equal to 4° for test configuration No. T1, and 2° for other test configurations (***Table 4.14***). More precisely, the theoretical crack nucleates at the contact trailing edge, and is characterized by a direction inward the contact region.

The experimental cracks were generally found to nucleate within the slip region at or close to the contact trailing edge. More precisely, some cracks initiated within the fretted zone. However, the exact distance between such cracks and the contact trailing edge was difficult to be measured, since the experimental contact area was characterized by indefinite and irregular boundaries. Moreover, most of

the cracks grew approximately perpendicular to the surface, in quite good agreement with the theoretical estimations.

As far as fatigue life is concerned, the number $N_{f,cal}$ of loading cycles to failure estimated by means of the proposed methodology is listed in ***Table 4.14*** for each test configuration. The ratio $N_{f,exp}/N_{f,cal}$ is also listed in ***Table 4.14*** for test configurations characterized by an acceptable failure mode. Moreover, a comparison between experimental and estimated fatigue life is shown in ***Figure 4.12*** for such test configurations. Note that the dashed lines correspond to $N_{f,exp}/N_{f,cal}$ equal to 0.5 and 2, thus defining the scatter band 2.

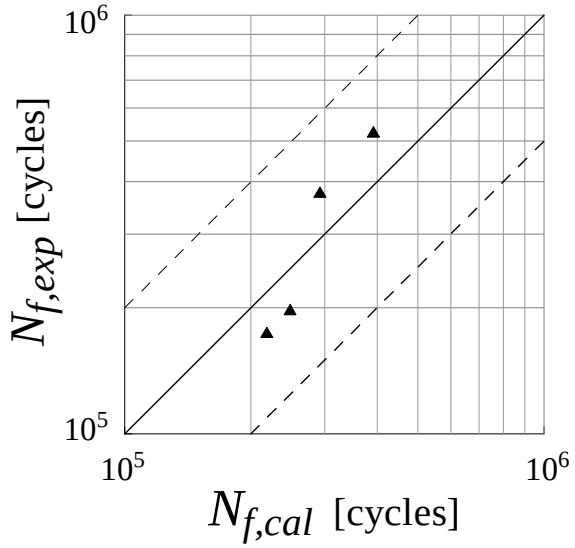

Figure 4.12 *Experimental fatigue life vs. estimated fatigue life for tests characterised by acceptable failure modes.*

It can be observed that all the results fall within the scatter band 2 and, therefore, the estimations are quite satisfactory. In more detail, the proposed methodology provides conservative estimations for two over four test configurations (***Table 4.14***). Moreover, the accuracy of the criterion is verified by means of the root mean square error method: the value of T_{RMS} is equal to 1.42, which highlights a quite good accuracy of the criterion employed.

As far as the specimens characterised by an anomalous failure mode are concerned, the proposed methodology estimates a number of loading cycles to failure higher than the value considered as a lower limit listed in ***Table 4.14*** for test configuration No. T1.

Therefore, it can be stated that the methodology proposed in the present Ph.D. Thesis provides quite satisfactory results in terms of both crack path orientation and fretting fatigue life.

4.7 EN8 steel

The experimental campaign carried out by O'Halloran et al. (O'Halloran, 2017) has been examined. Such an experimental campaign is detailed in Section 4.7.1, whereas the results determined by employing the proposed methodology are discussed in Section 4.7.2.

4.7.1 Experimental campaign

Flat dog-bone test specimens made of EN8 steel were tested. The mechanical and fatigue properties are listed in ***Table 4.15*** (O'Halloran, 2017).

Table 4.15 Mechanical and fatigue properties of EN8 steel (O'Halloran, 2017).

MATERIAL	E [GPa]	ν	σ_u [MPa]	$\sigma_{af,-1}$ [MPa]	m	$\tau_{af,-1}$ [MPa]	m^*	N_0 [cycles]
EN8	189	0.3	882	276	-0.12	159	-0.12	$2 \cdot 10^6$

The averaged grain size d is equal to $30\,\mu m$ (Vantadori, 2019), whereas the coefficient of friction μ within the contact zone is equal to 0.75 (O'Halloran, 2017).

The experimental tests were carried out in partial slip regime by using two cylindrical pads (made of the same material of the specimens). The pad radius R was equal to $6\,mm$. Such tests were characterised by fretting wear loading conditions. More precisely, a constant normal load P and a cyclic tangential

displacement $\Delta(t)$ (characterised by a loading ratio $R=-1$) were applied to the pads. All the tests were interrupted at 10^5 loading cycles.

The above experimental tests were carried out in order to both estimate the effective value of the coefficient of friction and compare the results with those determined by means of a numerical model developed by the same Authors (O'Halloran, 2017).

Once the numerical model was validated, different fretting fatigue configurations were numerically simulated by considering the same material such as that of the experimental tests. Such configurations were characterised by cylindrical pads, with pad radius R equal to $3\,mm$. A constant normal load P and a cyclic tangential displacement $\Delta(t)$ (characterised by a loading ratio $R=-1$) were applied to the pads: the value of the normal load was equal to $227\,N/mm$, whereas different values of the amplitude Δ_a of the tangential displacement were considered.

Such numerical investigations were characterised by either partial slip or gross slip regime, depending on the value of the applied amplitude of the tangential displacement. In more detail, the transition from partial slip to gross slip regime was found to be in correspondence of a transition value $\Delta_{a,t}$ of the tangential displacement amplitude equal to about $3.8\,\mu m$ (O'Halloran, 2017). Note that simulations characterised by $\Delta_a < \Delta_{a,t}$ are taken into account here, since the methodology proposed in the present Ph.D. Thesis may be applied to fretting fatigue problems in partial slip regime. A value of Δ_a equal to $1\,\mu m$, $2\,\mu m$, $3\,\mu m$ and $3.8\,\mu m$ was applied in numerical simulations No. 1, 2, 3 and 4, respectively.

4.7.2 Results

The numerical simulations described in Section 4.7.1 have been analysed by means of the analytical methodology proposed in the present Ph.D. Thesis for fretting fatigue assessment of structural components.

In order to determine the stress field within the specimen by employing the analytical formulation detailed in Section 2.4 of the present Ph.D. Thesis, the

amplitude Q_a of the tangential load needs to be defined for each numerical simulation. In more detail, such a loading parameter is computed as a function of the amplitude Δ_a of the tangential displacement, by means of the following equation:

$$Q_a = \frac{\mu P}{\Delta_{a,t}} \Delta_a \qquad (4.3)$$

Therefore, the tangential load amplitude Q_a equal to $9.9\ N/mm$, $19.7\ N/mm$, $29.6\ N/mm$, and $37.5\ N/mm$ is considered for numerical simulations No. 1, 2, 3 and 4, respectively.

Note that *Equation (4.3)* has been deduced by considering that, in partial slip regime, the value of the ratio Q_a/P linearly increases as the amplitude of the tangential displacement increases (Jin, 2004). Such a ratio reaches its maximum value (equal to the coefficient of friction μ) in correspondence to the transition between partial slip and gross slip regimes, that is, for $\Delta_a = \Delta_{a,t}$. Note that such a relation is not valid for gross slip regime.

As far as the crack path orientation is concerned, the angle θ_{cal} estimated by means of the proposed methodology was equal to 7°, 11°, 15° and 10°, for numerical simulations No. 1, 2, 3 and 4, respectively. More precisely, the theoretical crack nucleates at the contact trailing edge, and is characterized by a direction inward the contact region. However, no data in terms of numerical crack path are available in the literature for the tests considered.

As far as fatigue life is concerned, the number $N_{f,cal}$ of loading cycles to failure estimated by means of the proposed methodology is equal to 648679, 52699, 28257 and 10352, for numerical simulations No. 1, 2, 3 and 4, respectively.

Moreover, the fretting map (in terms of number of loading cycle to failure against displacement amplitude) built by taking into account the analytical results related to the above fretting wear tests under partial slip regime is shown in ***Figure 4.13***. The comparison between the number of loading cycles to failure numerically

estimated by O'Halloran et al. (O'Halloran, 2017) and that analytically estimated in the present Ph.D. Thesis is also reported in ***Figure 4.13***. Note that such a comparison seems to highlight a quite good accuracy of the proposed analytical methodology for EN8 steel, but further comparisons with experimental test results are needed.

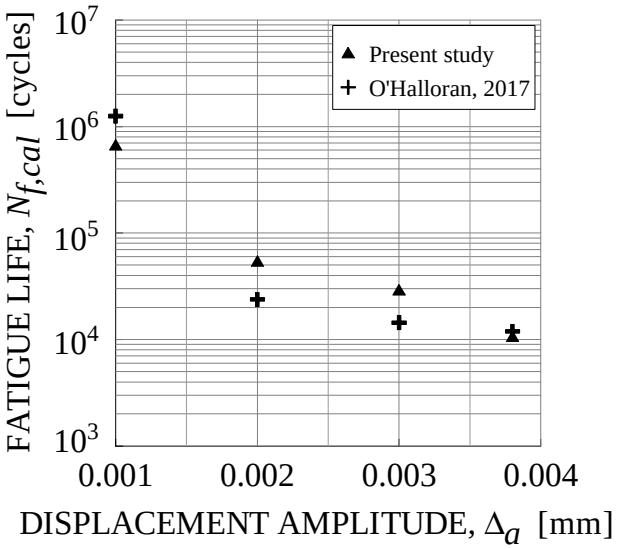

Figure 4.13 *Fretting map in terms of fatigue life vs. displacement amplitude: results estimated in the present Ph.D. Thesis and numerical results by O'Halloran et al. (O'Halloran, 2017).*

4.8 AISI 1034 steel

The experimental campaign carried out by Araújo et al. (Araújo, 2017) has been analysed by means of the proposed methodology. Such an experimental campaign is detailed in Section 4.8.1, whereas the results determined by employing the proposed methodology are discussed in Section 4.8.2.

4.8.1 Experimental campaign

Flat dog-bone test specimens made of AISI 1034 steel were tested. The mechanical and fatigue properties are listed in ***Table 4.16*** (Araújo, 2017; Li, 2017).

Table 4.16 Mechanical and fatigue properties of AISI 1034 steel (Araújo, 2017; Li, 2017).

MATERIAL	E [GPa]	ν	σ_u [MPa]	$\sigma_{af,-1}$ [MPa]	m	$\tau_{af,-1}$ [MPa]	m^*	N_0 [cycles]
AISI 1034	200	0.3	600	299	-0.10	173	-0.10	$2 \cdot 10^6$

The averaged grain size d is equal to $30\,\mu m$ (Fouvry, 2008), whereas the coefficient of friction μ within the contact zone is equal to 0.9 (Araújo, 2017).

The experimental tests were carried out in partial slip regime by using two cylindrical pads made of chromium 52,100 steel ($E = 210\,GPa$, $\upsilon = 0.3$, $\sigma_y = 1700\,MPa$). The pad radius R was equal to $40\,mm$.

A constant normal load P and a cyclic tangential load $Q(t)$ (characterised by a loading ratio $R = -1$) were applied to the pads. In particular, the values of the normal load P and the amplitude Q_a of the tangential load were equal to $227\,N/mm$ and $169\,N/mm$, respectively.

The tests were interrupted at 10^6 loading cycles and, subsequently, crack direction was measured on the longitudinal middle-cross section by means of a confocal laser microscope. The experimental crack path orientation θ_{exp} is defined as the angle between the crack direction and a line perpendicular to the surface. The average value of such an angle was found to be equal to 30°, with the crack path inside the contact zone.

4.8.2 Results

The experimental campaign described in Section 4.8.1 has been analysed by means of the analytical methodology proposed in the present Ph.D. Thesis for fretting fatigue assessment of structural components.

As far as the crack path orientation is concerned, the angle θ_{cal} estimated by means of the proposed methodology was equal to 12°. More precisely, the theoretical crack nucleates at the contact trailing edge, and is characterized by a direction inward the contact region.

The direction of experimental cracks was found to be inward the contact region for all the tests, in accordance with the theoretical estimations. The average experimental crack orientation was found to be equal to 30°. The comparison between experimental and analytical crack orientations is shown in ***Figure 4.14***. It should be highlighted that the experimental crack orientation is related to a crack length equal to $68\,\mu m$, whereas the theoretical crack orientations are related to a length equal to twice the averaged grain size of the material, that is, $2d = 60\,\mu m$.

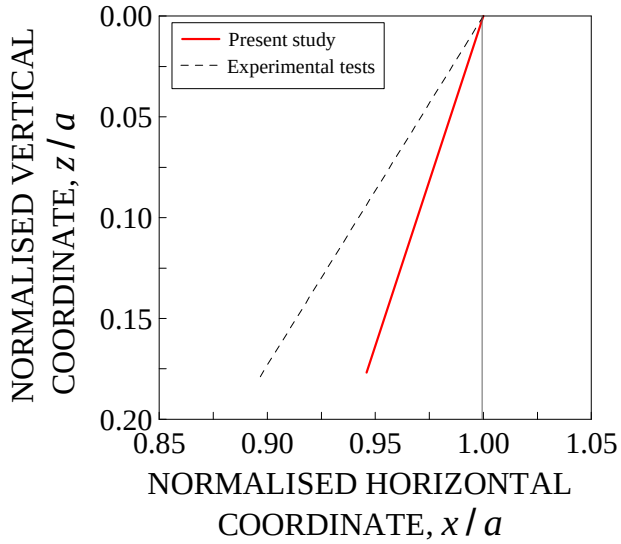

Figure 4.14 *Comparison between experimental and theoretical crack orientation.*

An analytical simulation of the above experimental tests was also provided by Araújo et al. (Araújo, 2017). In more detail, three different multiaxial fatigue parameters were employed, that is, the SWT parameter proposed by Smith, Watson and Topper (Smith, 1970), the FS parameter proposed by Fatemi and Socie (Fatemi, 1988), and the Modified Wohler Curve Method (MWCM) parameter (Susmel, 2002). Moreover, three different critical plane averaging methods were applied using the above parameters, in order to estimate the initial crack direction. Note that the estimated crack orientations are related to a length ranging from about $214\,\mu m$ to $428\,\mu m$, depending on the employed method.

Araújo et al. remarked that the experimental crack paths could be estimated by employing the SWT parameter better than by using the shear-based parameters (i.e., FS and MWCM parameters). In particular, the crack direction was predicted inward the contact region by employing the SWT parameter, with estimated angle equal to 11°. On the other hand, the estimated crack direction was generally outward the contact region by employing the shear-based parameters (when associated with the Critical Direction Method, the MWCM predicted crack directions inward the contact region, with estimated angle equal to 70°).

Therefore, it can be stated that the estimated crack path reproduces the experimental one with good agreement for AISI 1034 steel. In particular, the methodology proposed in the present Ph.D. Thesis provides more appropriate results in terms of crack path orientation with respect to other shear-based criteria available in the literature. More precisely, such a methodology correctly predicts crack direction inward the contact region, with crack angle comparable to that estimated by means of a SWT parameter-based approach available in the literature.

As far as fatigue life is concerned, the number $N_{f,cal}$ of loading cycles to failure estimated by means of the proposed methodology is equal to 2119173. Note that a comparison between experimental and estimated fatigue life is not possible, since the experimental number of loading cycles to failure is unknown for all the tests. Nevertheless, it can be observed that the value of loading cycle number estimated by means of the proposed methodology is higher than the value of run-out.

4.9 35NCD16 steel

The experimental campaign carried out by Araújo et al. (Araújo, 2017) has been analysed by means of the proposed methodology. Such an experimental campaign is detailed in Section 4.9.1, whereas the results obtained by employing the proposed methodology are discussed in Section 4.9.2.

4.9.1 Experimental campaign

Flat dog-bone test specimens made of 35NCD16 steel were tested. The mechanical and fatigue properties are listed in ***Table 4.17*** (Araújo, 2017; Kurek, 2017).

Table 4.17 Mechanical and fatigue properties of 35NCD16 steel (Araújo, 2017; Kurek, 2017).

MATERIAL	E [GPa]	ν	σ_u [MPa]	$\sigma_{af,-1}$ [MPa]	m	$\tau_{af,-1}$ [MPa]	m^*	N_0 [cycles]
35NCD16	200	0.3	1270	361	-0.10	342	-0.07	$2 \cdot 10^6$

The experimental tests were carried out in partial slip regime by using two cylindrical pads made of 100C6 steel ($E = 195\,GPa$, $\upsilon = 0.3$, $\sigma_y = 1500\,MPa$). The pad radius R was equal to $80\,mm$.

A constant normal load P and a cyclic tangential load $Q(t)$ (characterised by a loading ratio $R = -1$) were applied to the pads. In particular, the values of the normal load and the amplitude Q_a of the tangential load were equal to $1000\,N/mm$ and $500\,N/mm$, respectively.

The tests were interrupted at $5 \cdot 10^5$ loading cycles and, subsequently, crack direction was measured on the longitudinal middle-cross section by means of a confocal laser microscope. The experimental crack path orientation θ_{exp} is defined as the angle between the crack direction and a line perpendicular to the surface. The average value of such an angle was found to be equal to 11°, with the crack path inside the contact zone.

4.9.2 Results

The experimental campaign described in Section 4.9.1 has been analysed by means of the analytical methodology proposed in the present Ph.D. Thesis for fretting fatigue assessment of structural components.

As far as the crack path orientation is concerned, the angle θ_{cal} estimated by means of the proposed methodology was equal to 7°. More precisely, the theoretical crack nucleates at the contact trailing edge, and is characterized by a direction inward the contact region.

The direction of experimental cracks was found to be inward the contact region for all the tests, in accordance with the theoretical estimations. The average experimental crack orientation was found to be equal to 17°. The comparison between experimental and analytical crack orientations is shown in ***Figure 4.15***. It

should be highlighted that the experimental crack orientation is related to a crack length equal to $105\,\mu m$, whereas the theoretical crack orientations are related to a length equal to twice the averaged grain size of the material, that is, $2d = 30\,\mu m$.

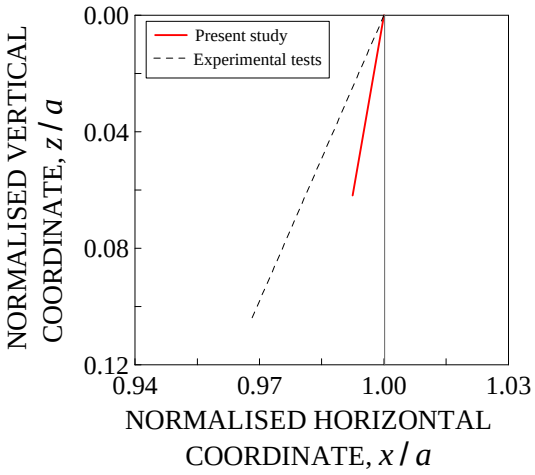

Figure 4.15 *Comparison between experimental and theoretical crack orientation.*

An analytical simulation of the above experimental tests was also provided by Araújo et al. (Araújo, 2017). In more detail, three different multiaxial fatigue parameters were employed, that is, the SWT parameter proposed by Smith, Watson and Topper (Smith, 1970), the FS parameter proposed by Fatemi and Socie (Fatemi, 1988), and the Modified Wohler Curve Method (MWCM) parameter (Susmel, 2002). Moreover, three different critical plane averaging methods were applied using the above parameters, in order to estimate the initial crack direction. Note that the estimated crack orientations are related to a length ranging from about $39\,\mu m$ to $78\,\mu m$, depending on the employed method.

Araújo et al. remarked that the experimental crack paths could be estimated by employing the SWT parameter better than by using the shear-based parameters (i.e., FS and MWCM parameters). In particular, the crack direction was predicted inward the contact region by employing the SWT parameter, with estimated angle ranging from 4° to 6°. On the other hand, estimated crack direction was generally outward the contact region by employing the shear-based parameters (when associated with the Critical Direction Method, both FS and MWCM predicted

crack direction inward the contact region, with estimated angle equal to 46° and 53°, respectively).

Therefore, it can be stated that the estimated crack path reproduces the experimental one with good agreement for 35NCD16 steel. In particular, the methodology proposed in the present Ph.D. Thesis provides more appropriate results in terms of crack path orientation than other shear-based criteria available in the literature. More precisely, such a methodology correctly predicts crack direction inward the contact region, with crack angle comparable to that estimated by means of a SWT parameter-based approach available in the literature.

As far as fatigue life is concerned, the number $N_{f,cal}$ of loading cycles to failure estimated by means of the proposed methodology is equal to 133762. Note that a comparison between experimental and estimated fatigue life is not possible, since the experimental number of loading cycles to failure is unknown for all the tests. Nevertheless, it can be observed that the value of number of loading cycles estimated by means of the proposed methodology is slightly lower than the value of run-out.

4.10 References

Abrahams R., Mikhail J., Fasihi P. Effect of friction stir process parameters on the mechanical properties of 5005-H34 and 7075-T651 aluminium alloys. *Materials Science and Engineering*, 2019; 751: 363–73.

Almeida G.M.J., Pessoa G.C.V., Cardoso R.A., Castro F.C., Araújo J.A. Investigation of crack initiation path in AA7050-T7451 under fretting conditions. *Tribology International*, 2020; 144: 106103.

Araújo J.A., Nowell D., Vivacqua R.C. The use of multiaxial fatigue models to predict fretting fatigue life of components subjected to different contact stress fields. *Fatigue and Fracture of Engineering Materials and Structures*, 2004; 27: 967-978.

Araújo J.A., Nowell D. Mixed high low fretting fatigue of Ti6Al4V: Tests and modelling. *Tribology International*, 2009; 42: 1276-1285.

Araújo J.A., Almeida G.M.J., Ferreira J.L.A., da Silva C.R.M., Castro F.C. Early cracking orientation under high stress gradients: The fretting case. *International Journal of Fatigue*, 2017; 100: 611-618.

Carpinteri A., Spagnoli A., Vantadori S. Multiaxial fatigue assessment using a simplified critical plane-based criterion. *International Journal of Fatigue*, 2011; 33: 969-976.

Cattaneo C. Sul contatto di due corpi elastici: distribuzione locale degli sforzi. *Rendiconti dell'Accademia Nazionale dei Lincei*, 1938; 27, 6: 342–8.

Chen H., Shang D.G., Tian Y.J., Liu J.Z. Comparison of multiaxial fatigue damage models under variable amplitude loading. *Journal of Mechanical Science and Technology*, 2012; 26: 3439–46.

Fatemi A., Socie D.F. A critical plane approach to multiaxial fatigue damage including out-of-phase loading. *Fatigue and Fracture of Engineering Materials and Structures*, 1988; 11, 3: 149-65.

Fouvry S., Nowell D., Kubiak K., Hills D.A. Prediction of fretting crack propagation based on a short crack methodology. *Engineering Fracture Mechanics*, 2008; 75: 1605–1622.

Hertz H. *Miscellaneous Paper by Heinrich Hertz*. New York: Macmillan & Co; 1896.

Jin O., Mall S. Effects of slip on fretting behaviour: experiments and analyses. *Wear*, 2004; 256: 671-684.

Johnson K.L. *Contact Mechanics*. UK: Cambridge University Press; 1985.

Kurek M., Łagoda T., Morel F. Estimation of the fatigue life of 35ncd16 alloy steel under random loading. *Materials Science*, 2017; 52, 4: 492-499.

Li C., Dai W., Duan F., Zhang Y., He D. Fatigue Life Estimation of Medium-Carbon Steel with Different Surface Roughness. *Applied Science*, 2017; 7, 338.

Li J., Zhou J., Sun Y., Feng A., Meng X., Huang S., Sun Y. Study on mechanical properties and microstructure of 2024-T351 aluminum alloy treated by cryogenic laser peening. *Optics and laser Technology*, 2019; 120: 105670.

McEwen E. Stress in elastic cylinders in contact along a generatrix. *Philosophical Magazine*, 1949; 40: 454.

Mindlin R.D. Compliance of elastic bodies in contact. *ASME Journal of Applied Mechanics*, 1949; 16: 259–68.

Nowell D., Hills D. Mechanics of fretting fatigue tests. *International Journal of Mechanical Sciences*, 1987; 29, 5: 355–65.

O'Halloran S.M., Shipway P.H., Connaire A.D., Leena S.B., Harte A.M. A combined wear-fatigue design methodology for fretting in the pressure armour layer of flexible marine risers. *Tribology International*, 2017; 108: 7–15.

Rossino L.S., Castro F.C., Bose Filho W.W., Araújo J.A. Issues on the mean stress effect in fretting fatigue of a 7050–T7451 Al alloy posed by new experimental data. *International Journal of Fatigue*, 2009; 31: 2041–8.

Sabelkin V., Martinez S. A., Mall S., Sathish S., Blodgett M.P. Effects of shot-peening intensity on fretting fatigue crack-initiation behaviour of Ti–6Al–4V. *Fatigue and Fracture of Engineering Materials and Structures*, 2005; 28: 321-332.

Smith K.N., Watson P., Topper T.H. A stress-strain function for the fatigue of metals. Journal of Materials, 1970; 5, 4: 767-78.

Susmel L., Lazzarin P. A bi-parametric W€ohler curve for high cycle multiaxial fatigue assessment. *Fatigue and Fracture of Engineering Materials and Structures*, 2002; 25, 1: 63-78.

Schulze V. *Modern Mechanical Surface Treatment*. Wiley-VCH, 2006.

Szolwinski M.P., Farris T.N. Observation, analysis and prediction of fretting fatigue in 2024-T351 aluminum alloy. *Wear*, 1998; 221: 24-36.

Taylor D. *The Theory of Critical Distances: A New Perspective in Fracture Mechanics*. UK: Elsevier; 2007.

Vantadori S., Carpinteri A., Iturrioz I. Fretting failure of a pressure armour in an unbonded flexible riser. *International Journal of Fatigue*, 2019; 128: 105203.

Vantadori S., Zanichelli A. Fretting-fatigue analysis of shot-peened aluminium and titanium test specimens. *Fatigue and Fracture of Engineering Materials and Structures*, 2020; In press.

Vázquez J., Navarro C., Domínguez J. Experimental results in fretting fatigue with shot and laser peened Al 7075-T651 specimens. *International Journal of Fatigue*, 2012; 40: 143–53.

Vázquez J., Navarro C., Domínguez J. A model to predict fretting fatigue life including residual stresses. *Theoretical and Applied Fracture Mechanics*, 2014; 73: 144-151.

Vázquez J., Navarro C., Domínguez J. Analysis of fretting fatigue initial crack path in Al7075-T651 using cylindrical contact. *Tribology International*, 2017; 108: 87-94.

Wagner L. (Ed.). *Shot Peening*. Proceedings of the 8th International Conference on Shot Peening, Wiley–VCH, Weinheim, 2003.

5
CONCLUSIONS

An analytical methodology for fretting fatigue assessment of structural components has been proposed in the present Ph.D. Thesis. In more detail, such a methodology may be employed in order to evaluate both the initial crack path and the lifetime of metallic structures under fretting fatigue elastic partial slip loading conditions. Consequently, being based on linear-elastic formulations, it could be easily applied to practical situations in the industrial field.

The proposed methodology falls in the category of stress-based critical-plane approach. In particular, the multiaxial fatigue criterion originally proposed by Carpinteri et al. for metallic structures under multiaxial constant amplitude fatigue loading in high-cycle fatigue regime is here extended to the case of fretting fatigue.

The Carpinteri et al. criterion is implemented in conjunction with the Critical Direction Method proposed by Araújo et al. Such a non-local approach is employed in order to determine the orientation of the critical plane, thus avoiding two drawbacks typical of the stress-based critical-plane approach: (a) the need to evaluate the critical plane orientation in many points of the specimen, and (b) anomalous situations (that arise in problems characterised by high stress gradients) occurring when the critical plane orientations determined in adjacent points may be completely different from each other.

Moreover, the philosophy related to the theory of the Critical Distance by Taylor is taken into account in the procedure for the definition of the verification point where to perform the fretting fatigue assessment of the structural component. The fatigue life in such a point is evaluated in accordance to the Carpinteri et al. criterion by means of an equivalent stress amplitude, after the reduction of the multiaxial stress state to an equivalent uniaxial one.

Furthermore, the linear relationship between the amplitude and the mean value of the stress component perpendicular to the critical plane proposed by Goodman is employed in order to take into account the simultaneous presence of both a tensile or compressive mean normal stress and an alternating normal stress. In particular, such a relationship allows to take into account the beneficial effect on fatigue life due to the presence of a compressive mean normal stress. Such a situation is typical of fretting fatigue problems in which either a compressive mean axial stress is applied to the component or a compressive residual stress field is induced by shot peening.

The stress field used as input for the Carpinteri et al. criterion is analytically evaluated by using the closed-form solution by Johnson, based on the formalisms by Hertz, Cattaneo and Mindlin, and McEwen, together with the closed-form solution by Nowell and Hills.

The behaviour of metallic components under fretting fatigue elastic partial slip loading conditions has been assessed in order to validate the proposed methodology. In more detail, ten different experimental campaigns available in the literature characterised by either cylindrical or spherical contact configurations, carried out under either fretting fatigue or fretting wear loading conditions have been examined.

As far as the crack path orientation is concerned, the experimental cracks were found to nucleate at or close to the contact trailing edge, and to grow inward the contact region or perpendicular to the contact surface. The theoretical cracks nucleate at the contact trailing edge, and are characterized by a direction inward the contact region or perpendicular to the contact surface, in accordance to the experimental results. Nevertheless, further comparisons with theoretical results are quite difficult. In particular, the experimental cracks show some direction changes, whereas the proposed methodology contemplates a single critical plane orientation, estimated by taking into account a process zone characterised by a fixed size equal to twice the averaged grain size of the material. Moreover, multiple cracks nucleating within the slip region close to the contact trailing edge have been observed in some cases, whereas a single crack starting from the hot-spot at the contact trailing edge is considered in the proposed methodology.

Therefore, it can be stated that the crack direction estimated by means of the proposed methodology is in a quite good agreement with the experimental evidences. Moreover, such results are more appropriate than those determined by means of other shear-based criteria available in the literature, and the values of crack angle computed in the present Ph.D. Thesis are comparable to those estimated by means of a SWT parameter-based approach available in the literature. However, further developments are still needed to improve the accuracy between estimated and observed crack angles.

As far as fatigue life is concerned, the estimated values of loading cycle number to failure are in good agreement with the experimental ones. Moreover, the accuracy of the methodology in terms of fatigue life evaluation is verified by means of the root mean square error method: the value of T_{RMS} ranges from 1.34 to 1.86 for the analysed cases, thus highlighting a good correlation.

Therefore, the methodology proposed in the present Ph.D. Thesis seems to provide results in terms of number of loading cycles to failure characterised by a satisfactory accuracy. More precisely, such results are comparable with those related to more complex numerical approaches in the literature. Although by analysing the results obtained in the present Ph.D. Thesis the proposed methodology seems to be characterised by a promising accuracy, further investigations on different materials and contact configurations are needed.

It is worth noting that the proposed analytical methodology has the advantage to be able to estimate both crack path and fatigue life, without physically taking into account the crack in the model, and thus it is computationally efficient. However, it has the drawback that both the fretting fatigue life and crack path estimations are referred to a verification point located at a fixed distance from the hot-spot.

A strong point of the proposed methodology consists in taking into account the material average grain size. In fact, it has been observed that an accurate fretting fatigue assessment needs to include features of the material microstructure. In particular, both the critical plane orientation and the verification point position are related to such a size.

Moreover, it should be highlighted that a possible influence of the slip amplitude on the fretting fatigue behaviour of the component analysed is discarded, since a stress-based approach is implemented in the proposed methodology.

However, since the superficial damage produced at the contact surface within the partial slip regime is not high, such a hypothesis seems to be acceptable.

On the other hand, the influence of the high stress gradient is clearly captured using the Critical Direction Method by Araújo et al. Therefore, the proposed analytical methodology seems to be promising not only for fretting fatigue, but also for other fatigue problems involving high stress gradients, in the case of both proportional and non-proportional stress histories.

NOMENCLATURE

FS	Fatemi and Socie fatigue parameter
MWCM	Modified Wohler Curve Method fatigue parameter
SWT	Smith, Watson and Topper fatigue parameter

δ	angle between the normal to the critical plane and the averaged direction of the maximum principal stress
δ_1, δ_2	displacements of points T_1, T_2
$\Delta(t)$	cyclic tangential displacement applied to the pads
$\Delta\sigma_{af,-1}$	fatigue limit range for fully reversed normal loading
$\Delta K_{I,th}$	threshold stress intensity factor range for long cracks
ε_y	deformation in correspondence of material yielding
μ	coefficient of friction
ν	Poisson coefficient
θ	orientation of a critical plane candidate
θ_{cal}	crack path orientation estimated in the present Ph.D. Thesis
θ_{crit}	critical plane orientation
θ_{exp}	experimental crack path orientation from the literature
Θ	orientation of a generic rectangle bordering the Σ path
$\boldsymbol{\sigma}$	stress tensor

$\sigma_{eq,a}$	equivalent uniaxial stress amplitude related to the critical plane
$\sigma_{af,-1}$	fatigue limit under fully reversed normal stress
$\sigma'_{af,-1}$	finite life fatigue strength under fully reversed normal stress
$\sigma_B(t)$	cyclic axial stress (bulk stress) applied to the specimen
σ_{eff}	effective linear elastic stress quantity
σ_n , $n=1,2,3$	principal stresses, where $\sigma_1(t) \geq \sigma_2(t) \geq \sigma_3(t)$
$\hat{\sigma}_n$, $n=1, 2, 3$	averaged principal stresses within a loading cycle, where $\sigma_1(t) \geq \sigma_2(t) \geq \sigma_3(t)$
σ_u	material ultimate tensile strength
σ_y	stress in correspondence of material yielding
Σ	closed path of the shear stress component on the critical plane
Σ'	polygonal approximation of Σ path
$\tau_{af,-1}$	fatigue limit under fully reversed shear stress
$\tau'_{af,-1}$	finite life fatigue strength under fully reversed shear stress
$\phi(t), \theta(t), \psi(t)$	principal Euler angles
$\hat{\phi}, \hat{\theta}, \hat{\psi}$	averaged principal Euler angles

a	half-width of contact zone
c	half-width of stick zone
$c'(t)$	instantaneous half-width of stick zone
$\boldsymbol{C}$	shear stress component lying on the critical plane
C_a	amplitude of the shear stress component lying on the critical plane

C_m	mean value of the shear stress component lying on the critical plane
d	average material grain size
e	eccentricity of stick zone
$e'(t)$	instantaneous eccentricity of stick zone
E	elastic modulus
E^*	elastic modulus for plane strain condition
G	tangential elastic modulus
h	distance between the contact body surfaces (Chapter 2)
$h[x]$	Heaviside step function (Chapter 3)
H	hot-spot
l	depth of contact bodies
L	critical distance
m	slope of the S-N curve under fully reversed normal loading
m^*	slope of the S-N curve under fully reversed shear loading
N	normal stress component perpendicular to the critical plane
N_0	reference number of loading cycles
N_a	amplitude of the normal stress component perpendicular to the critical plane
$N_{eq,a}$	amplitude of the equivalent normal stress component perpendicular to the critical plane
N_f	number of cycles to failure
N_m	mean value of the normal stress component perpendicular to the critical plane
$Oxyz$	reference frame for the contact problem (Chapter 2)
$p(x)$	normal pressure distribution between contact bodies

p_0	maximum value of normal pressure distribution
P	normal constant force applied to the pads
P_{crit}	critical point where to perform the fretting fatigue assessment
$PXYZ$	fixed reference system (Chapter 3)
$Puvw$	local reference system related to the critical plane
$P123$	principal reference system
$q(x)$	contact shear distribution between contact bodies
q_0	maximum value of contact shear distribution
Q	static tangential force applied to the pads
$Q(t)$	cyclic tangential force applied to the pads
R	relative radius of curvature of contact bodies (Chapter 2)
R	radius of the pads (Chapter 3 and Chapter 4)
R', R''	main relative radii of curvature of contact bodies
s_x	slip between contact surfaces
$\boldsymbol{S}_w$	stress vector referred to the critical plane
S_1, S_2	points on the contact surface (Chapter 2)
t	time
T	period of the loading cycle
T_1, T_2	points reasonably distant from the contact surface (Chapter 2)
T_{RMS}	root mean square error
$\bar{u}_{z1}, \bar{u}_{z2}$	displacements of points S_1, S_2
$\mathbf{w}$	normal to the critical plane
$W(t)$	weight function
z_1, z_2	surface profiles of contact bodies

Subscripts

a	amplitude
cal	analytical value calculated in the present Ph.D. Thesis
exp	experimental value from literature
m	mean value
max	maximum value
min	minimum value

LIST OF PUBLICATIONS

Papers in International Journals

Vantadori S., Carpinteri A., Di Cocco V., Fortese G., Iacoviello F., Natali S., Ronchei C., Scorza D., Zanichelli A. Novel zinc-based alloys used to improve the corrosion protection of metallic substrates. *Engineering Failure Analysis*, 2017; 82: 327-339. DOI:10.1016/j.engfailanal.2017.05.043

Vantadori S., Boaretto J., Fortese G., Giordani F., Rodrigues R.I., Iturrioz I., Ronchei C., Scorza D., Zanichelli A. Fatigue strength of welded joints under multiaxial non-proportional loading. *Procedia Structural Integrity*, 2017; 5: 761-768, Open Access. DOI:10.1016/j.prostr.2017.07.167

Bernardi P., Michelini E., Sirico A., Vantadori S., Zanichelli A. Fracture toughness of fibre-reinforced concrete determined by means of numerical analysis. *Procedia Structural Integrity*, 2017; 5: 848-855, Open Access. DOI:10.1016/j.prostr.2017.07.090

Vantadori S., Haynes R., Fortese G., Habtour E., Ronchei C., Scorza D., Zanichelli A. Methodology for assessing embryonic cracks development in structures under high-cycle multiaxial random vibrations. *Fatigue and Fracture of Engineering Materials and Structures*, 2018; 41: 20-28. DOI:10.1111/ffe.12634

Carpinteri A., Boaretto J., Fortese G., Giordani F., Rodrigues R.I., Iturrioz I., Ronchei C., Scorza D., Vantadori S., Zanichelli A. Welded joints under multiaxial non-proportional loading. *Theoretical and Applied Fracture Mechanics*, 2018; 93: 202-210. DOI:10.1016/j.tafmec.2017.08.004

Carpinteri A., Di Cocco V., Fortese G., Iacoviello F., Natali S., Ronchei C., Scorza D., Vantadori S., Zanichelli A. Mechanical behaviour and phase transition mechanisms of a shape memory alloy by means of a novel analytical model. *Acta Mechanica et Automatica*, 2018; 12: 105-108. DOI:10.2478/ama-2018-0017

Vantadori S., Carpinteri A., Guo L.P., Ronchei C., Zanichelli A. Synergy assessment of hybrid reinforcements in concrete. *Composites Part B*, 2018; 147: 197-206. DOI:10.1016/j.compositesb.2018.04.020

Vantadori S., Carpinteri A., Fortese G., Ronchei C., Scorza D., Zanichelli A. Fatigue lifetime evaluation of notched components: Implementation of the control volume concept in a strain-based LCF criterion. *Theoretical and Applied Fracture Mechanics*, 2018; 97: 400-408. DOI:10.1016/j.tafmec.2017.07.001

Zanichelli A., Carpinteri A., Fortese G., Ronchei C., Scorza D., Vantadori S. Contribution of date-palm fibres reinforcement to mortar fracture toughness. *Procedia Structural Integrity*, 2018; 13: 542-547. DOI:10.1016/j.prostr.2018.12.089

Scorza D., Carpinteri A., Fortese G., Ronchei C., Vantadori S., Zanichelli A. Multiaxial fatigue life estimation in low-cycle fatigue regime including the mean stress effect. *MATEC Web of Conferences*, 2018; 165: 16002, Open access. DOI:10.1051/matecconf/201816516002

Vantadori S., Carpinteri A., Zanichelli A. Lightweight construction materials: Mortar reinforced with date-palm mesh fibres. *Theoretical and Applied Fracture Mechanics*, 2019; 100: 39-45. DOI:10.1016/j.tafmec.2018.12.011

Carpinteri A., Vantadori S., Zanichelli A. Lifetime estimation of mechanical assemblies under constant amplitude fretting fatigue loading. *Fatigue and Fracture of Engineering Materials and Structures*, 2019; 42, 9: 1927-1936. DOI:10.1111/ffe.13043

Vantadori S., Carpinteri A., Luciano R., Ronchei C., Scorza D., Zanichelli A. Mean stress effect on fatigue life estimation for Inconel 718 alloy. *International Journal of Fatigue*, 2020; 133: 105391. DOI:10.1016/j.ijfatigue.2019.105391

Vantadori S., Carpinteri A., Luciano R., Ronchei C., Scorza D., Zanichelli A., Okamoto Y., Saito S., Itoh T. Crack initiation and life estimation for 316 and 430 stainless steel specimens by means of a critical plane approach. *International Journal of Fatigue*, 2020; 138: 105677. DOI:10.1016/j.ijfatigue.2020.105677

Vantadori S., Carpinteri A., Głowacka K., Greco F., Osiecki T., Ronchei C., Zanichelli A. Fracture toughness characterisation of a glass fibre-reinforced plastic composite. *Fatigue and Fracture of Engineering Materials and Structures*, 2020; In press. DOI: 10.1111/ffe.13309

Vantadori S., Vázquez J., Zanichelli A. Fretting fatigue and shot peening: a multiaxial fatigue criterion including residual stress relaxation. *Tribology International*, 2020; 151: 106537. DOI:10.1016/j.triboint.2020.106537

Vantadori S., Zanichelli A., Araújo J.A. Fretting fatigue of 7050-t7451 al alloy: the influence of bulk mean stress. *International Journal of Fatigue*, 2020; 140: 105816. DOI:10.1016/j.ijfatigue.2020.105816

Zanichelli A., Vantadori S. Shot-peened fretting fatigue components: endurance strength and fatigue life assessment. *Material Design and Processing Communications*, 2020; 196: 1-5. DOI:10.1002/mdp2.196

Vantadori S., Ronchei C., Zanichelli A. Fatigue life assessment of DCI smooth specimens. *Material Design and Processing Communications*, 2020. DOI:10.1002/mdp2.210

Vantadori S., Zanichelli A. Fretting-fatigue analysis of shot-peened aluminium and titanium test specimens. *Fatigue and Fracture of Engineering Materials and Structures*, 2020; In press. DOI:10.1111/ffe.13367

Conference papers

Zanichelli A., Rooholamini H., Hassani A., Vantadori S., Scorza D., Ronchei C., Fortese G. *Fracture toughness of hybrid fibre reinforced concrete.* Proceedings of **The 25th Annual International Conference on Composites/Nano Engineering (ICCE-25)**, Rome, Italy, 2017.

Fortese G., Carpinteri A., Vantadori S., Zanichelli A., *Stress gradient effect in estimating fretting fatigue life.* Proceedings of **The Contact Mechanics International Symposium (CMIS 2018),** Biella, Italy, 2018.

Zanichelli A., Carpinteri A., Fortese G., Ronchei C., Scorza D., Vantadori S. *Fracture behaviour of hybrid roller-compacted concrete.* Proceedings of **The 26th Annual International Conference on Composites/Nano Engineering (ICCE-26)**, Paris, France, 2018.

Fortese G., Carpinteri A., Iturrioz I., Ronchei C., Scorza D., Vantadori S., Zanichelli A. *A novel hot-spot stress calculation for tubular welding joints used in agricultural sprayers.* Proceedings of **The XIX International Colloquium on Mechanical Fatigue of Metals (ICMFM XIX),** Porto, Portugal, 2018.

Zanichelli A., Carpinteri A., Fortese G., Ronchei C., Scorza D., Vantadori S. *Numerical modeling of hybrid roller-compacted concrete under monotonic loading.* Proceedings of **The 21st International Conference on Composite Structures (ICCS21)**, Bologna, Italy, 2018.

Zanichelli A., Carpinteri A., Vantadori S. *Fracture toughness of date-palm fibre-reinforced mortar*. Proceedings of **The 6th International Conference on Crack Paths (CP 2018)**, Verona, Italy, 2018.

Zanichelli A., Carpinteri A., Vantadori S. *Fretting fatigue crack path and lifetime estimation in Al 7075 aluminium alloy.* Proceedings of **The 9th International Symposium on Fretting Fatigue (ISFF9)**, Seville, Spain, 2019.

Vantadori S., Carpinteri A., Ronchei C., Scorza D., Zanichelli A. *Mean stress effects on Low-Cycle Fatigue behaviour of Inconel 718 alloy*. Proceedings of

the 12th International Conference on Multiaxial Fatigue and Fracture (ICMFF12), Bordeaux, France, 2019.

Vantadori S., Carpinteri A., Marsavina L., Ronchei C., Scorza D., Zanichelli A. *Size-independent performance of a novel model to compute Mode I fracture toughness in composites*. Proceedings of **The 25th International Conference Fracture and Structural Integrity (IGF 25)**, Catania, Italy, 2019.

Scorza D., Carpinteri A., Marsavina L., Ronchei C., Vantadori S., Zanichelli A. *Fracture toughness of particleboard by means of the modified two-parameter model*. Proceedings of **The 5th International Conference on Mechanics of Composites (MECHCOMP2019)**, Lisbon, Portugal, 2019.

Vantadori S., Carpinteri A., Ronchei C., Scorza D., Zanichelli A. *Influence of hot-spot location on fretting fatigue crack path and lifetime estimation.* **XXV Congresso dell'Associazione Italiana di Meccanica Teorica e Applicata (AIMETA 2019)**, Rome, Italy, 2019.

Il mio primo ringraziamento è rivolto alla Professoressa Sabrina Vantadori, la cui guida ha reso possibile il mio percorso di Dottorato. Grazie anche per tutto il tempo che mi ha dedicato, per tutti i quesiti che mi ha risolto, per la fiducia che mi ha dimostrato e per la grande passione che mi ha trasmesso.

Un sentito ringraziamento anche al Professore Andrea Carpinteri, per i Suoi preziosi insegnamenti, la Sua estrema disponibilità e il Suo sostegno.

Inoltre, vorrei ringraziare le mie colleghe Camilla e Daniela per l'immancabile supporto, i numerosi consigli e la serenità del tempo trascorso insieme in ufficio.